MICROWAVE SIGNAL PROCESSING

WITH

PHOTOREFRACTIVE DYNAMIC HOLOGRAPHY

By

Edeline Fotheringham

B.A., Diplôme d'Ingénieur,

Ecole Nationale Supérieure de Physiques de Strasbourg, 1998

M.S., Diplôme d'Etudes Approfondies,

Université Louis Pasteur de Strasbourg, 1998

A thesis submitted to the

Faculty of the Graduate School of the

University of Colorado in partial fulfillment

of the requirements for the degree of

Doctor of Philosophy

Department of Electrical & Computer Engineering

2003

This thesis entitled:

"Microwave signal processing with photorefractive dynamic holography"

written by Edeline Fotheringham

has been approved for the

Department of Electrical & Computer Engineering

_____

Dr. Dana Z. Anderson

_____

Dr. Leo Hollberg

Date_____

The final copy of this thesis has been examined by the signatories, and

we find that both the content and the form meet acceptable presentation

standards for scholarly work in the above mentioned discipline.

Fotheringham, Edeline (Ph.D. Electrical Engineering)

Microwave signal processing with dynamic holography

Thesis directed by Prof. Dr. Dana Z. Anderson

Abstract

Have you ever found yourself listening to the music playing from the closest stereo rather than to the bromidic (uninspiring) person speaking to you? Your ears receive information from two sources but your brain listens to only one. What if your cell phone could distinguish among signals sharing the same bandwidth too? There would be no "full" channels to stop you from placing or receiving a call.

This thesis presents a nonlinear optical circuit capable of distinguishing uncorrelated signals that have overlapping temporal bandwidths. This so called autotuning filter is the size of a U.S. quarter dollar and requires less than 3 mW of optical power to operate. It is basically an oscillator in which the losses are compensated with dynamic holographic gain. The combination of two photorefractive crystals in the resonator governs the filter's winner-take-all dynamics through signal-competition for gain. This physical circuit extracts what is mathematically referred to as the largest principal component of its spatio-temporal input space.

The circuit's practicality is demonstrated by its incorporation in an RF-photonic system. An unknown mixture of unknown microwave signals, received by an antenna array, constitutes the input to the system. The output electronically returns one of the original microwave signals. The front-end of the system down converts the 10 GHz microwave signals and amplifies them before the signals phase modulate optical beams. The optical carrier is suppressed from these beams so that it may not be considered as a signal itself to the autotuning filter. The suppression is achieved with two-beam coupling in a single

photorefractive crystal. The filter extracts the more intense of the signals present on the carrier-suppressed input beams. The detection of the extracted signal restores the microwave signal to an electronic form. The system, without the receiving antenna array, is packaged in a 13x18x6" briefcase. Its power consumption equals that of a regular 50 W household light bulb. The system was shipped to different parts of the country for real-time demonstrations of signal separation thus also validating its claim to robustness.

DEDICATION

To my mother,

who lovingly offered me the keys to a blossoming life.

To my friends Gaelle and Christophe,

who opened my eyes to the world and to myself.

ACKNOWLEDGEMENTS

TABLE OF CONTENTS

LIST OF FIGURES

CHAPTER 1

INTRODUCTION

1. 1   Overview

This thesis aims to demonstrate the potential usefulness of photorefractive circuits in microwave signal processing. Photorefractive crystals are nonlinear holographic materials with a short-time memory and the ability to couple coherent optical beams at low intensities. We take advantage, as most modern optics based communications, of the fact that a narrow band device at optical frequencies translates into a broadband device at microwave frequencies [1]. The photorefractive volume gratings, with which we deal in this thesis, typically have lengths on the order of half a centimeter. This gives them a Bragg matched bandwidth of hundreds of gigahertz, amply sufficient to cover microwave frequencies.

Prof. D.Z. Anderson's group has a long history of information processing with photorefractive circuits. Our group has specialized in manipulating signals with novelty filter two-beam coupling configurations [2-5] and self-organized photorefractive resonators [6-9]. Circuits were built that performed processing tasks such as demultiplexing signals carried by different frequencies [10], or present on the input at different times [11], as well as controlling the relative intensities of signals [12]. The photorefractive community commonly employs resonators to design information processing circuits [13-22], and less often, novelty filters [23]. This thesis concentrates on possible uses of an oscillator-based photorefractive

circuit for microwave signal processing. The circuit extracts the largest principal component [24] of its input signal space. We mainly refer to it as the "autotuning filter" for reasons that will be explained later. The filter's design is a variation on the feature extractor's design previously reported on by Mark Saffman [25]. This thesis also shows the application of the novelty filter configuration to the suppression of the optical carrier of phase-modulated beams at microwave frequencies. The work on carrier suppression was pioneered by Valeria Damiao [26] and so this report presents only the basic principles that are necessary for contextualizing our use of it.

1. 1. 1   The photorefractive effect

Depending on the photorefractive material, two-wave mixing may transfer phase information between coherent beams or energy or a combination of both. The coupling constant Γ characterizes the exchange. Γ is purely imaginary for materials in which drift dominates the movement of free carriers generated by photoexcitation. Such materials record holograms that couple only the phase information of coherent beams. Γ is purely real for diffusion dominated materials that couple only the energy of interfering beams [27]. Energy transfer results from a $\pi/2$-phase shift between the light interference pattern and the index modulation it generates. A more in depth explanation of the phenomenon may be found in textbooks such as [28, 29].

The optical circuits presented in this thesis use barium titanate ($BaTiO_3$) crystals as photorefractive media, which is a diffusion-dominated material [30]. The coupling constants of these crystals commonly reach 20 cm^{-1}. The value of Γ indicates the potential depth of the index modulation and thus represents the potential diffraction efficiency of the photorefractive grating. The effective Γ in experiments, depends on the geometry of the beams and the orientation of these beams relative to the c-axis (or optical axis) of the birefringent crystal.

Two-beam coupling in barium titanate is analogous to an electronic transistor. A transistor has two inputs and one output. The output current is an amplified copy of one of the currents coming in. The extra current is provided by the non-amplified input. Two-beam coupling requires coherent input beams. In the crystal, one beam undergoes amplification, keeping all its spatio-temporal characteristics, at the expense of the other input beam's energy. The latter beam is often referred to as the "pump" beam. This optical transistor outputs both the amplified and the de-amplified beams. Its small signal gain is given by

Exp[ΓL] where L is the length of the grating in the material. For a typical 5 mm grating and a pump-to-small-signal ratio of 10^5, gains reach 20 000 or 40 dB.

Of particular interest in this work, is two-beam coupling with temporally modulated beams. The coupling beams may be modulated with more than one signal. If the various signals are temporally uncorrelated, they photorefractively couple as if they were the only signal present but with a modified coupling constant. Each signal experiences a coupling constant diminished by the ratio of their own intensity to the total intensity in the crystal. For example, the small signal gain for each temporal component is *Exp*[$I_{signal}/I_{total} \cdot \Gamma$L]. The fact that the available gain is finite means that when more signals are present the less each signal gets amplified. This phenomenon is one of the basic building blocks for the designs of our competition-for-gain driven photorefractive circuits.

The photorefractive material's memory provides another building block for the design of our circuits. The time constant of barium titanate is on the order of milliseconds to seconds depending on the total intensity of the light. A photorefractive index modulation therefore, mimics the light patterns the material is submitted to, but integrated over time. In other words, these holograms do not record the simple multiplication of the electrical fields generating the interference patterns, but rather the correlation of those fields over a few seconds. This correlation function is essential for the autotuning filter's ability to distinguish signals among a collection of uncorrelated signals. Milliseconds are an unnecessarily long time to integrate radio frequency signals for correlation. The slow time constant of barium titanate limits the adaptation speed of the autotuning filter to abruptly changing input signals. It also limits the lowest frequency of the signals it can process to a few kilohertz. The time constant does not, however, affect the processing of higher frequency signals.

1. 1. 2   The autotuning filter

The autotuning filter is designed to separate out the strongest uncorrelated signal from its spatio-temporal input space. This space refers to multiple coherent optical beams carrying amplitude and/or phase information. The strongest uncorrelated signal is closely related to the largest principal component of the input space. This relationship is clarified in the theoretical section 2. 4. 2. 1. Throughout this thesis, however, the terms "stronger signal" and "largest principal component" are used interchangeably.

The autotuning filter is fundamentally an optical ring oscillator in which gain is supplied by photorefractive two-beam coupling [31-39]. The input beams "pump" the gain medium. The cavity modes of the oscillator intersect these pump beams inside the photorefractive crystal aligned to transfer the most energy to the oscillating beam. The oscillation starts with scattered light from the pump beam that is naturally emitted in the direction of greatest gain. This fanning phenomenon [40] is a result of local photorefractive two-beam coupling between the scattered light and the propagating beam.

Figure 1.1 illustrates the design of the autotuning filter. The crystal on the left-hand side of the ring is the gain medium mentioned above that couples the input beams to the oscillating beam in the ring. The additional photorefractive crystal on the right-hand side of the ring, acts as a selective loss element. It "absorbs" a signal inversely proportionally to its power. Since the gain medium amplifies proportionally to a signal's relative strength, the two photorefractive interactions combine to facilitate the oscillation of only the largest principal component in the ring. In steady state, the other principal components remain on the pump beams at the output of the gain crystal. The filter effectively extracts the strongest signal from its input. That signal may be retrieved by sampling the oscillating beam of the

resonator. Thus the filter potentially has two outputs: one output to provide the strongest signal and the other output to provide all the other signals.
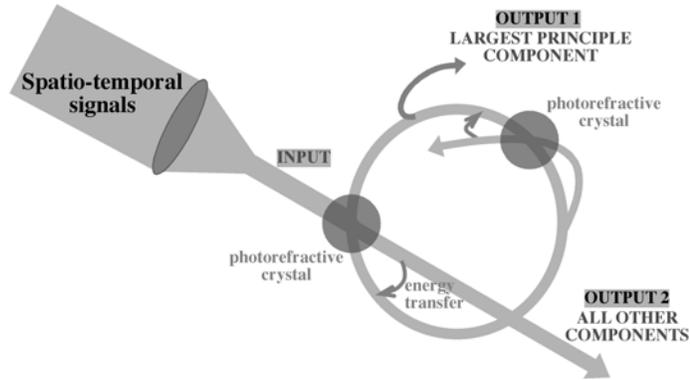
Figure 1.1. Schematic diagram of the autotuning filter.

Which (if not both) output is of interest depends on the application. For example, if the input beams are carrying a mixture of a weak signal and a strong jammer, output #2 (refering to Figure 1.1) delivers the desired signal while the ring extracts the unwanted jammer. If the input mixture contains a signal with much additive noise, then output #1 provides a noise-reduced signal. If all the principal components of a collection of information carrying beams need to be extracted then "daisy-chaining" autotuning filters at the #2 outputs yields the extracted components at the #1 outputs.

Many more applications can be found in the vast field of principal component analysis (PCA) [24]. PCA is a fundamental tool in the analysis of statistical data. It is generally a computer intensive method relegated to the post-recording processing of data. Real-time, adaptive principal component extraction is in its infancy. As digital signal processing techniques improve [41, 42] and the complexity of neural networks increases [43, 44], PCA finds applications in low frequency wireless communications. Neural network architectures have added adaptive capabilities to principal component extractor circuits [45, 46]. Those

implementations are computer based however and are therefore also signal bandwidth limited.

The optical filter discussed in this thesis is 5 cm^2 in size and extracts the principal components of up to 3-GHz bandwidth signals in seconds. Although the filter is based on an optical resonator, the photorefractive dynamics give the device adapting capabilities. For example, the circuit keeps track of slow drifts of the optical and the signal carrier frequencies. We believe that the literature presents no other optical adaptive extractor of spatio-temporal principal components. Most optical systems involving PCA realize pre-determined pattern recognition [47-50], or analyze and classify optical spectra [51-54].

1. 1. 3   An optically smart antenna array

We chose to demonstrate the potential merit of the autotuning filter in a communications scenario. More specifically, the filter was incorporated in the adaptive optical processor of signals received by a microwave antenna array. Adaptive processing in smart antenna systems [55, 56] can either be done at the analog front-end at the carrier frequency or after down conversion and analog-to-digital conversion at base-band using digital signal processing (DSP) techniques [57]. Front-end processing is fast, but expensive and complex as the adaptation circuitry requires microwave variable phase-shifters and variable gain-control elements. The more common DSP approach reduces system complexity, is more economical, and more flexible; however, it is typically power inefficient and has modest bandwidth. Part of this thesis's goal is to show that the use of photorefractive circuitry can simplify adaptive antenna systems and relieve the computational burden placed on the digital signal processing done after down conversion.

Principal component extraction on antenna array signals subscribes to the broad field of blind source separation (BSS) [58, 59]. This field seeks to separate unknown mixtures of unknown signals that possibly have overlapping bandwidths. The less assumptions a blind separation method makes about the unknown signals, the more powerful it is. For principal component separation to function as a BSS method [59], the unknown signals have to be received in temporally and spatially orthogonal mixtures. The temporal orthogonality or non-correlation is guaranteed in most communications scenarios by the fact that the signals are emitted from independent sources. The spatial orthogonality is a more restrictive condition. However, as will be shown in Chapter 3, principal component separation as a BSS method works only as well as the signals are spatially uncorrelated. The signals are 100% spatially

correlated only when they are emitted from the same spatial location (within the receiving antenna's angular resolution.)

The architecture of the processing system discussed in this report is intended to be used in applications with a large number of antenna elements. The experimental demonstration uses only two microwave receivers and two test sources; however, the optical processor does not substantially change as the number of array elements increases. The prototype system is illustrated in Figure 1.2.
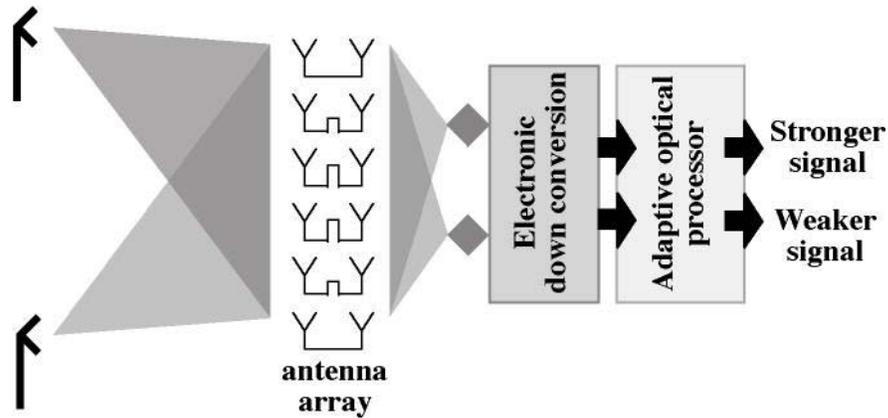
Figure 1.2. Block diagram of the prototype optically smart antenna array.

The first stage of our prototype system receives two 10 GHz signals from two distinct sources placed in the far field of the array. Audio signals amplitude-modulate the microwaves. The receiving front end consists of a 30-element antenna array that acts as a quasi-optical discrete lens [60] with detecting antennas placed on its focal arc. The two electrical signals from the detectors are then down converted to 150 MHz and amplified before being fed to the second stage of the system. The IF signals are applied to a one crystal, two-channel resonant electro-optic phase modulator. An optical line beam traverses the electro-optic modulator with its top half modulated with one of the IF signals and the bottom half modulated with the other. Since this is phase modulation with low modulation

indices, the original optical frequency is still present in the beam, necessitating a carrier suppression element in order for the autotuning filter to work properly. If the carrier is not suppressed it introduces artificial correlation between the signals that impairs the proper functioning of the filter. The suppression of the carrier is achieved by two-beam coupling the signal-bearing beam with a non signal-bearing beam. The photorefractive crystal is oriented such that the beam carrying information transfers energy to the non-modulated beam. Although the signals suffer a 3dB loss in the process, the carrier frequency is suppressed by over 50 dB. The final processing stage consists of the autotuning filter. It extracts the principal component of its two-dimensional input signal space. The oscillating beam of the filter is sampled and photodetected. Detection without homodyning is possible because the absence of the optical carrier turns the phase modulation into an amplitude modulation at twice the frequency. Demodulating electronics retrieve the audio signal from the AC port of the photodetector and send it to a speaker.

The whole system from the down conversion stage to the electronic output is packaged in a 13x18x6 inch briefcase. It plugs into a wall outlet consuming power equivalent to a common household light bulb. The briefcase system has proven its robustness and portability by demonstrating real-time principal component extraction around the country. The miniaturization and packaging of optics including interferometric setups in a briefcase is a significant accomplishment in and of itself. It shows that optical table-size systems (4x6 feet) may be considerably shrunk in size and made to work without the cumbersome vibration isolation offered by air-cushioned tables.

1. 1. 4   A photorefractive regenerative amplifier

Multiple stage electronic circuits require amplifier modules within or in between stages. The art and science of making amplifiers is a sophisticated branch of electronics. Sub-branches include high power amplifiers and low noise figure amplifiers, the design skills of which vary immensely depending on the operational frequency range. As our photorefractive systems grow in size and complexity, laser power becomes an issue. Barium titanate crystals generally have a high absorption constant— a typical α is between 1 and 2 cm^{-1} (for green wavelengths.) Taking the autotuning filter as a familiar example, this means that the through beam carrying all but the largest principal signal looses about half its energy passing through the "gain medium" of the ring (our crystals are typically around 5 mm in length.) Without an amplifier, the initial power of the beam determines how much more processing can be applied to it.

Optical regenerative amplification is a young field compared to its electronic counterpart [61]. The field blossomed in the early 1990's when optics were massively introduced in telecommunication systems. Optical amplifiers are, still today, developed mainly for the purposes of the communications industry. The operating wavelengths of the vast majority of these devices are therefore closely matched to the 1.3 and 1.5 μm communication wavelengths. Industrial research also focuses on single spatial mode amplifiers; again, because optical communication systems employ single mode fibers to propagate their beams. Unfortunately there are no efficient photorefractive materials at communication wavelengths. Barium titanate works best with blue and green wavelengths and rhodium doping extends its operating range to the visible red. Other photorefractive materials function for wavelengths up to 1.06 μm although their coupling constants Γ are not as high. In addition, the dynamics

of our photorefractive circuits require the spatial diversity of multi-mode beams. These facts prompted us to develop our own amplifiers.

The basic concept of a regenerative optical amplifier is relatively simple. Stimulated emission amplifies an optical information-carrying beam propagating through a population-inverted medium. The latter may be the same gain medium as the one used in the laser that originally generated the beam: the gain bandwidths of these materials generally cover thousands of gigahertz. A high noise figure constitutes the main drawback of non-parametric, i.e. simple, traveling wave amplifiers. The theoretical minimum decrease of the signal to noise ratio is 3 dB. A high number compared to low noise electronic amplifiers that limits the number of times a signal may be amplified before it drowns in noise.

The amplifier design presented in this thesis takes a multi-mode beam in and outputs an amplified single mode beam without any loss of temporal information. Like the autotuning filter it is essentially a photorefractive oscillator. A photorefractive element also couples the input to the oscillating beam. Unlike the autotuning filter, a semi-conductor laser diode amplifier provides gain to the loop and washes out the competition for photorefractive gain. The resonator is constrained to be single mode, which allows the use of a single mode semi-conductor amplifier in the ring. The oscillating beam picks up all the temporal information of the multi-mode input beam, since there is no competition for gain. The photorefractive gratings have no reason to organize themselves so as to select one part of the information over another. This oscillator thus transforms a multi-mode beam into a single mode with more energy.

This thesis reports the first steps toward making the amplifier. The semiconductor laser diode amplifier for red wavelengths was assembled in the laboratory, starting with uncoated chips. Another necessary experiment for demonstrating the feasibility of our photorefractive amplifier involved showing that a multi-mode beam could pump a resonant cavity that was forced to be single mode. This amplifier will hopefully be the first of a series. Our toolbox

of photorefractive circuits would be greatly enriched by the development of high performance semi-conductor amplifiers at red wavelengths. The privilege of that work though, is left for other graduate students. ☺

1. 2　　Thesis outline

This thesis reports work on three separate projects. Chapter 2 presents the experimental and theoretical progress in relation to the autotuning filter. Chapter 3 describes the making of an opto-electronic microwave processor and evaluates its performance. Chapter 4 reports on preliminary research for a photorefractive regenerative amplifier. The fifth and last chapter (the appendix) regroups supplementary technical information relative to various sections from the previous chapters.

Chapter 2 is divided into three sections. The first section aims to present the reader with an intuitive understanding of the autotuning filter's functioning. This short section offers enough information to make sense of the experimental section and provides a background for the discussions in the theoretical section. The second, experimental section describes the different implementation trials of the autotuning filter and discusses their performances. The third, theoretical section is divided into three parts. The first part studies the influence of the filter's parameters on its signal separation performance. The second part compares the experimental filter's data with a mathematically pure principal component extractor. The third part demonstrates the principal component extraction ability of the filter starting with the photorefractive differential equations embodying its design.

Chapter 3 describes in details the design, operation and measured performance of the adaptive microwave receiver. It consists of three major components: the microwave front end, the electro-optic modulation and carrier suppression stage, and the optical processing (auto-tuning filter) stage. A separate section explains each stage and reveals the packaging efforts that enabled to fit the system in a 13x18x6 inch briefcase. The result section reports the signal separation performance of the suitcase from a system's point of view. The last section of the chapter discusses the implementation of an extension of the 2-receiver system

to an N-receiver adaptive array, and the implications of using an optically smart quasi-optical antenna array in radar and communications.

Chapter 4 discusses the design of a photorefractive regenerative amplifier. It also reports on the experimental procedure to build a semiconductor laser diode amplifier necessary for the implementation of the photorefractive amplifier. The procedure described starts out with an uncoated and unmounted InGaAlP chip. The appendices present the detailed designs of some mechanical systems that we found particularly useful in the realization of the work presented in Chapters 2 and 3. They include practical information relating to the manufacturing of $BaTiO_3$ spheres and an operating manual for the suitcase system. The appendix also provides the Mathematica codes for the numerical simulation and study of the autotuning filter.

1. 3   Contributors to this thesis

The design of the autotuning filter was first presented in 1991 as a frequency demultiplexer [10]. This thesis introduces the building and testing of experimental versions of the filter as a principal component extractor. The influences of the filter's parameters on the device's signal separation performance were studied with a Mathematica program (presented in the appendices) that was greatly enhanced through discussions with Dr. A. Zozulya. His work on the stability analysis of a photorefractive feature extractor [62] allowed the demonstration of the autotuning filter's principal component extraction abilities in Chapter 2.

The realization of the suitcase project (Chapter 3) was the product of teamwork among Dr. S. Romisch and graduate student P. Smith, advised by Professor Z. Popovic, and myself. Dr. S. Romisch and P. Smith designed and built the front-end's electronics. I designed, machined and packaged the optical stage of the system. Dr. S. Romisch designed and built the demodulation electronics after the optical stage. Later, J.H. Loui helped me improve their performance. Dr. S. Romisch, P. Smith and I tested the different parts of the suitcase project and took the characterizing end-to-end measurements of the system. Professor D.Z. Anderson and Professor Z. Popovic contributed heavily to the discussion of the system from a communications perspective. The 4-channel implementation of Professor D.Z. Anderson's multiple-channel EOM idea, was designed, built and tested by graduate student H. Matern, advised by Professor Z. Popovic and experimentally assisted by myself.

My experimental work on assembling a semiconductor amplifier in Chapter 4, was guided by Dr. L. Hollberg. N. Mackie, a member of Dr. L. Hollberg's group, supervised and assisted my anti-reflection coating trials. Graduate student S. Hugh built the single mode cavity pumped by a multi-mode beam via a photorefractive crystal.

CHAPTER 2

THE AUTOTUNING FILTER

2. 1   Introduction

This chapter describes a photorefractive optical circuit that performs principal component extraction on an ensemble of spatially and temporally modulated signals. The circuit presented here is designed to process signals received by a microwave antenna array (see next chapter). In particular, it is designed to handle relatively large signal bandwidths as might be present in a communications receiver. The function of principal component extraction is a fundamental signal and data processing task employed in a much broader domain than simply communications [24]. It is the second order solution to the well-known problem of blind source separation [63]. A primary aim of this work is to demonstrate that a moderately sophisticated spatio-temporal signal-processing task can be implemented to good advantage with photorefractive nonlinear optics. Indeed, our miniaturized optical circuit is about the size of a U.S. quarter dollar, is capable of handling signal bandwidths in excess of one gigahertz, and can operate with an optical input power of less than 5 mW (and no other power source is needed to run the processor).

In the following sections, we fully characterize the circuit's handling of two spatially and temporally modulated signals. The processor is scalable to larger signal spaces without dramatic changes to its size or design. In these characteristics—high signal bandwidth, small

17

size, low power consumption, and scalability—the photorefractive signal processor compares favorably with a digital signal processor approach to the same function. Does the optical system remain in a favorable light when one contemplates an entire system from raw signal input to processed signal output? We believe the answer is yes. We have assembled a complete opto-electronic system around the processor presented here: from free-space microwave input, to the RF front-end, to the optical processor, and to the electrical output, the entire system is packaged in a standard-sized briefcase and consumes 50 W of power from the wall plug. This complete receiver system is described in Chapter 3. Here we focus on the design and characteristics of the photorefractive optical processor itself.

The photorefractive optical circuit presented in this thesis acts as a filter on the principal components of the input signal space. The largest principal component exits one output port while the remainder of the spatial-temporal signal space passes through the filter, as is schematically illustrated in Figure 2.1. We refer to this optical processor as an *autotuning filter*, for the circuit automatically tracks and extracts the principal components without having any *a priori* knowledge about the signal space.
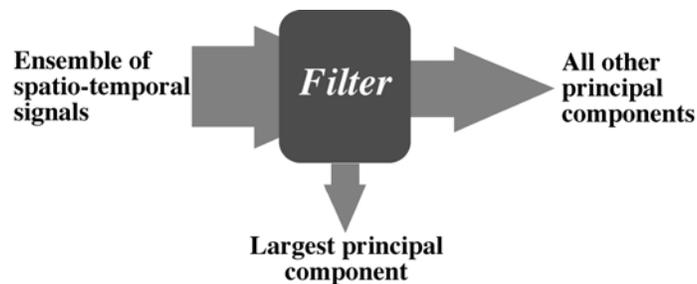
Figure 2.1. The filter extracts the largest principal component of its input signal space while passing on all the other components.

The first section of this chapter heuristically explains how the filter functions by using intuitive arguments of gain competition. The second section reports on the different

experimental implementations of autotuning filters. The performances of these filters at separating out two signals are regrouped at the end of this experimental section. The third and final section of this chapter is comprised of three parts. The first part qualitatively explores the optimization of the filter's design parameters. The second part compares the experimental results with those obtained with a pure principal component extractor. The third part of this theoretical section argues that the autotuning filter does physically implement the algebraic function of principal component extraction.

2. 2   A heuristic explanation of the filter's dynamics

The autotuning filter consists of a photorefractive ring oscillator [64], schematically depicted in Figure 2.2.   The photorefractive crystal on the left-hand side of the figure provides optical gain and the other one provides an active loss mechanism.
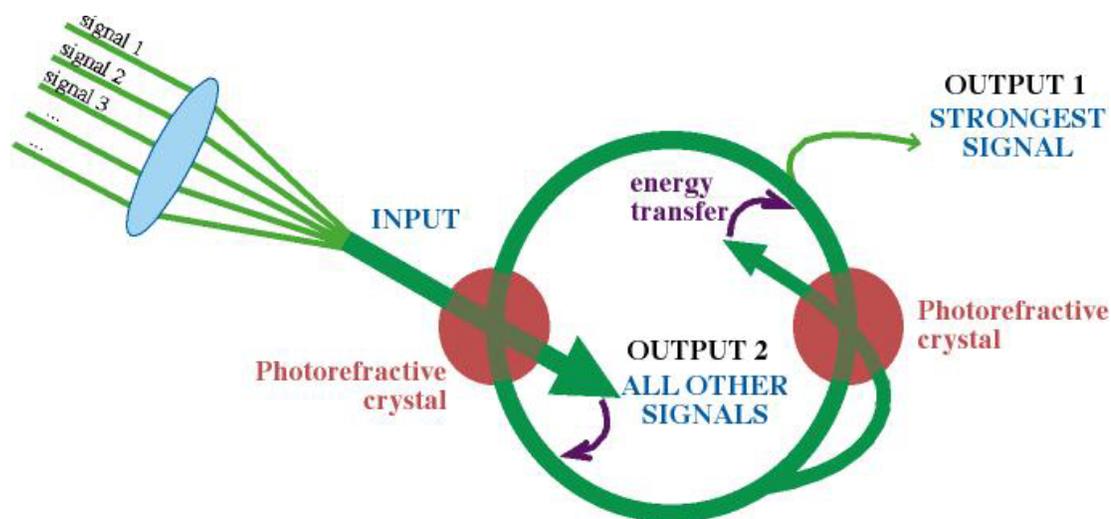
Figure 2.2. Schematic of the autotuning filter's design. The two-beam coupling occuring in the crystal on the left
of the figure provides gain to the ring. The two-beam coupling taking place in the crystal on the right
imposes loss on the ring signals inversely proportionally to their relative intensities.

Consider first a simple ring comprised of the gain medium alone. Also suppose that the input "pump beam" consists of a single spatial mode beam. The optical feedback loop is designed such that the gain is sufficient to cause oscillation in the ring. If the input beam is temporally modulated, then the oscillation beam will also be temporally modulated with essentially the same temporal structure. Suppose now that there are two beams having different, in particular uncorrelated, temporal structures. Again, the gain is chosen sufficiently large to overcome the round-trip losses so oscillation can once again take place.

What will be the temporal structure of the oscillating light? Will it carry the structure of one or both input beams?

The answer is "it depends." Ideally, the oscillating beam would have the temporal structure of solely the stronger input beam and none of the weaker. The second photorefractive crystal (on the right-hand side of Figure 2.2) is designed to enhance the circuit's ability to approach this ideal. The interaction that takes place in this medium is a special case of two-beam coupling referred to as reflexive coupling [12]. Figure 2.3 illustrates the effect reflexive coupling has on a multi-mode beam carrying two temporal signals. The initial beam is split in two unequal parts. They are then coupled to each other in a photorefractive crystal that is oriented to transfer energy from the brighter beam to the darker one. The signals in the latter get amplified proportionally to their relative intensities. This means that the stronger signal undergoes more amplification than the weaker one. At the output of the gain port, the intensity difference between the signals is larger than at the input. Overall, the weaker signals suffer more loss than the strongest one.
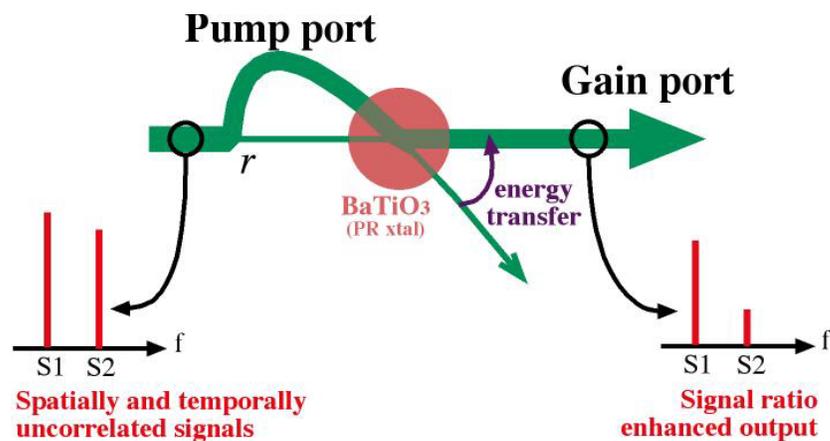
Figure 2.3. Reflexive coupling is a photorefractive selective loss element. It induces loss inversely proportionally to the strengths of signals.

Placed within the feedback loop of the gain medium, the reflexive-coupling element in the multi-mode ring oscillator effectively enhances the intensity differences among the signals until (ideally) only the initially strongest signal oscillates. At the same time, this strongest signal is largely removed from the input beam while all the other signals are passed on through the gain medium.

The oscillation in the autotuning filter starts with noise—photorefractive beam fanning in our case. The energy of the input beams alone powers the filter. If the carrier of those input beams (optical or RF) drifts with time, the circuit's dynamics automatically adjust to the change.

2. 3　Experimental versions of the filter

The first implementations of photorefractive feature extractors occupied about half the surface of an optical table (~2 m^2). The experimental efforts in building the filters presented in this thesis concentrated on miniaturization.   There are two main reasons for doing so. First, the cavity length of the ring oscillator determines the process bandwidth of the filter, as it is inversely proportional to the round trip time of the light.   Second, it makes the device more robust to environmental perturbations such as air currents and vibrations.

2. 3. 1　Fiber optic implementations of the filter

Fibers were our choice candidate to help us reduce the size of our filter device. Fibers dispense of using cumbersome adjustable mirror mounts for guiding the light. A fiberized device also appeared as more practical for future integration in optical systems.

For the photorefractive effect to govern the dynamics of the filter, the resonant cavity of the oscillator may be designed to be dispersionless or highly multi-mode. Either of these conditions ensure that the round trip phase requirement for oscillation plays no role in determining which signal wins the competition in the ring.

2. 3. 1. 1　Standard fiber technology

Photorefractive crystals are not presently integrated in fibers, so we opted to couple our optical beams in and out of fibers using gradient-index (GRIN) lens technology. Physically, the GRIN lenses look like small glass rods of 1.8 mm in diameter. They combine refraction at the plane end surfaces with continuous refraction (radial gradient-index material) within the rod [ref]. When cut to a specific length (pitch=0.23) they turn into a collimating lens with

zero back focal length. Their plane end can be put into contact with the plane end of a ferrule that holds a fiber. This theoretically leaves only two translation degrees of freedom with which to center the GRIN lens on the fiber tip located at the ferrule's end. This alignment may be adjusted using two pre-aligned v-grooves machined at the appropriate heights. Figure 2.4 shows coupling from fiber to fiber through a PR crystal using the GRIN lens and ferrule technology.
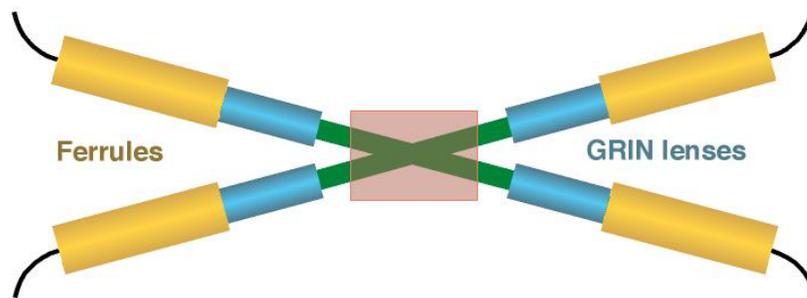
Figure 2.4. GRIN lenses collimate (and refocus) the light coming out of (or into) a fiber held by a ferrule.

Our fiber-to-fiber coupling efficiency reached a maximum of 50% only with complex, time-consuming alignment procedures (not counting the crystal's absorption). Part of the problem in our experiments was that the output beams from the GRIN lenses were never well collimated so that a portion of the light was emitted outside the receiving GRIN lens's numerical aperture.

2. 3. 1. 2   Spherical crystal technology

We greatly simplified our fiber-to-fiber coupling set up when we made spherical photorefractive crystals that doubled as lenses. We can couple light directly from bare fiber tip to bare fiber tip as shown in the diagram and photograph of Figure 2.5. The fibers' positions are constrained in v-grooves so that only one translation may be adjusted. The

position of the crystal sets all the remaining degrees of freedom necessary to optimize the fiber to fiber and the photorefractive coupling: x, y, z translations plus rotation of the c-axis in the xy plane. We achieve 75% coupling efficiency from one fiber to another. The multi-mode fibers we used had a core size of 64.5 μm and a numerical aperture of 0.268. Due to the birefringence of $BaTiO_3$ deviating the beams, however, the efficiency drops to about 50% when trying to couple 2 fibers to 2 other fibers. We still gain in ease of alignment and size of the filter over the previous version.
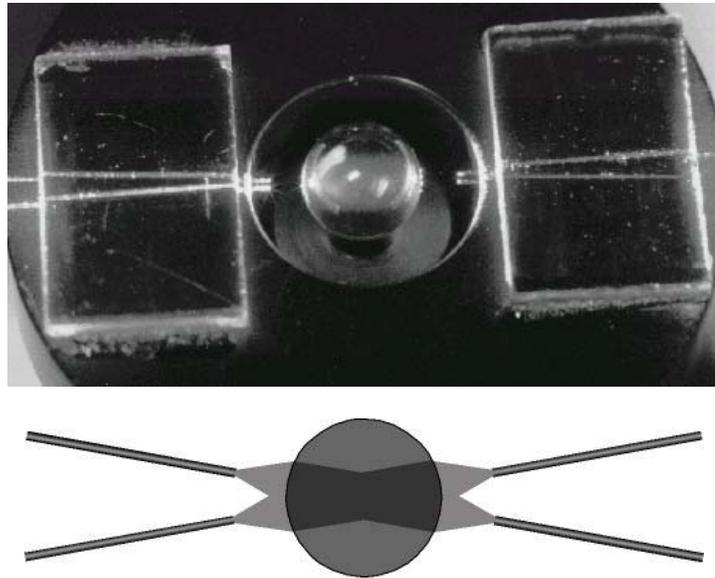
Figure 2.5. $BaTiO_3$ spherical crystals double as lenses to couple light from two fibers into two other fibers.

Our mechanical mounts for aligning the different elements evolved over time and the two main systems are described in Appendix 7. 2. The first version relies on glue to hold mechanical parts together making it difficult to disassemble for future reuse of the crystals. The second version is purely mechanically aligned and held in place. Figure 2.6.a shows photographs of filter implementations built with each aligning system. Another crucial mechanical aspect that enabled the realization of these devices is the manufacturing of the

spherical crystals themselves. Photorefractive spherical crystals are not commercially available. Appendix 7. 1 explains the process we have devised for making BaTiO3 spheres and slabs of spheres while wasting the least material.
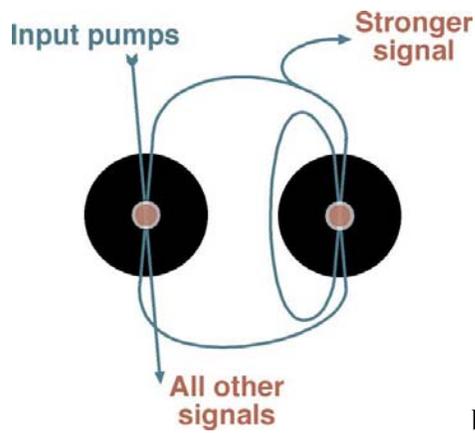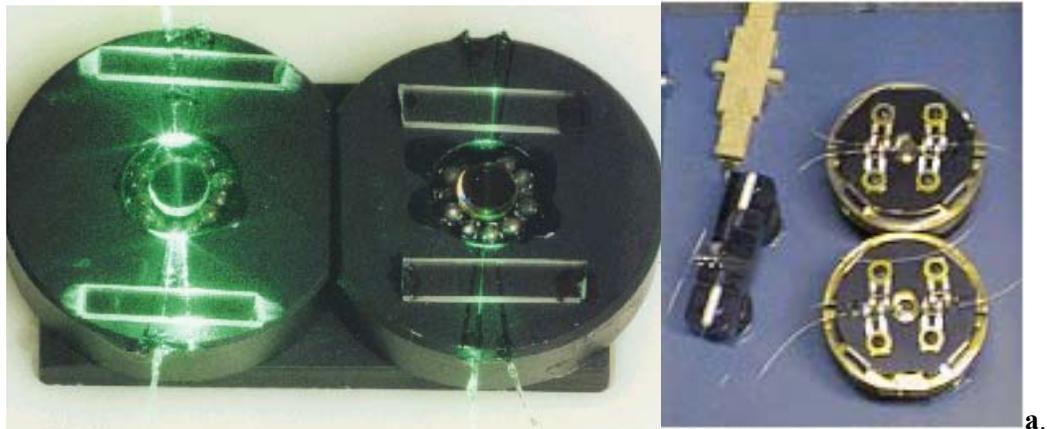
Figure 2.6. a) Photographs of the two fiberized autotuning filter versions. The crystals are slabs of spheres as it wastes less material than whole spheres. b) Design of the autotuning filter using fibers and spherical crystals.

Figure 2.6.b shows the layout of the fibers in these versions of the filter. We changed the reflexive coupling design of Figure 2.3. Instead of splitting the beam before the crystal with a fiber directional coupler, the whole beam goes through the crystal once and is guided back around to couple to itself. Two reasons prompted us to implement this change. One, it

simplifies the experimental setup while not fundamentally changing the dynamics of the reflexive coupling. Two, a multimode fiber directional coupler separates spatial modes rather than splitting off a portion of each. This induces slightly different dynamics for different loop paths thus breaking the degeneracy of the modes we initially designed for.

2. 3. 1. 3   Problems of multimode fibers

A problem common to all fiberized versions of the filter is the polarization scrambling property of multimode fiber. The photorefractive effect occurs only for polarizations that lie in the plane of the c-axis and the direction of propagation of the beams. With every roundtrip roughly half the light converts to the wrong polarization adding a 3dB loss factor to the loop. In addition, the intrinsic gain in the crystal goes as $\Gamma \dfrac{I_{signal}}{I_{total}}$ so that the wrong polarized light decreases the available gain by half.

High roundtrip losses were the main obstacle to obtaining a device with expected signal separation performance (see theoretical section below). Replacing multimode fibers with single mode fibers would require making the resonator's cavity dispersionless. We decided that an easier path involved abandoning fibers altogether and working on miniaturizing free space optics.

2. 3. 2   Free space optics implementation of the filter

2. 3. 2. 1   Miniature optics

The components of the filter are two BaTiO3 crystals for the reflexive and gain units, two planar mirrors and one spherical mirror for the ring cavity, and a beam splitter to split the beam for the reflexive coupling. Except for the crystals, we cut out miniature versions of

these elements from their normal size (1 inch optics) counterparts. We reduced alignment degrees of freedom by precisely cutting their bottom surface at "exactly" 90 degrees to the reflecting surfaces. These 90 degrees were measured by comparison to a commercial 90 degree prism. This cut eliminates the need for vertical tilt adjustments on the elements. Horizontal tilt and translation are adjusted externally before the components are glued in place (Norland UV glue #63). The crystals are mounted so that their center height roughly corresponds to the spherical mirror's center height. Figure 2.7 shows the filter compared to a U.S. quarter dollar. The two central elements are the gold bar shaped photorefractive $BaTiO_3$ crystals. The four outer elements include the two plane mirrors, the spherical mirror (radius of curvature: 5 cm) and the beam splitter (about 5% reflection on one side and anti-reflection coated on the other). The substrate is a quartz disc of 25 mm diameter.
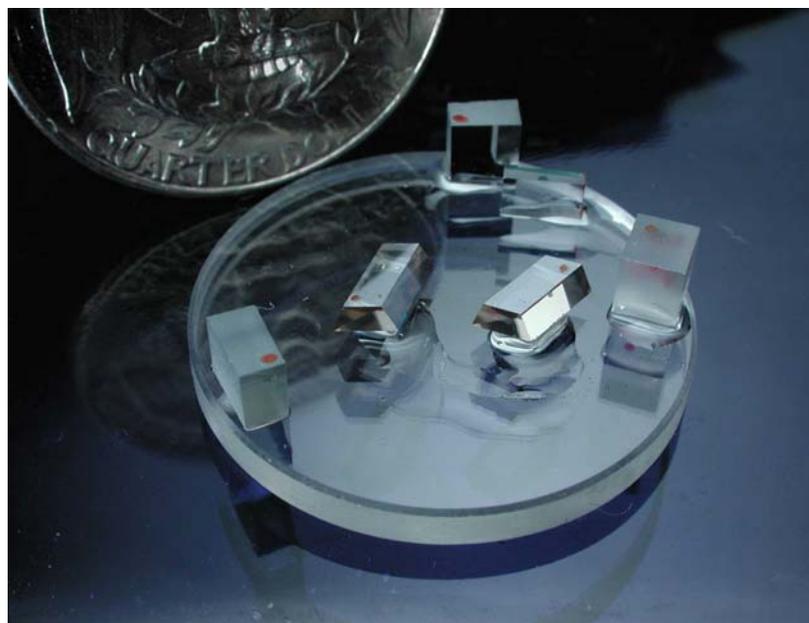
Figure 2.7. Photograph of the autotuning filter using free space miniature optics.

2. 3. 2. 2   Novel crystal cut

The original crystal cut we designed allows taking full advantage of the photorefractive crystal's available gain. In a conventional straight parallelogram cut, unwanted oscillations started by scattered light often arise between two parallel faces of the crystal. For one, the typical small signal gain of barium titanate is high (Γ=20/cm) and two, the index of refraction (n=2.4) induces 17% normal reflection at the crystal/air interfaces. These oscillations are in direct competition for gain with the desired two-beam coupling interactions and so decrease the effective available gain. Making the two opposite faces in question (the ones roughly parallel to the propagating beam) non-parallel prevents secondary oscillations. The crystals' geometry is shown in Figure 2.8. The crystals proved to have excellent saturation characteristics: a pump-beam to weak-beam ratio of one results in a gain of exactly two. Also, to reduce the reflection losses of the signal beam, the entrance and exit faces of the crystal are cut so that the angle of incidence is Brewster's angle.
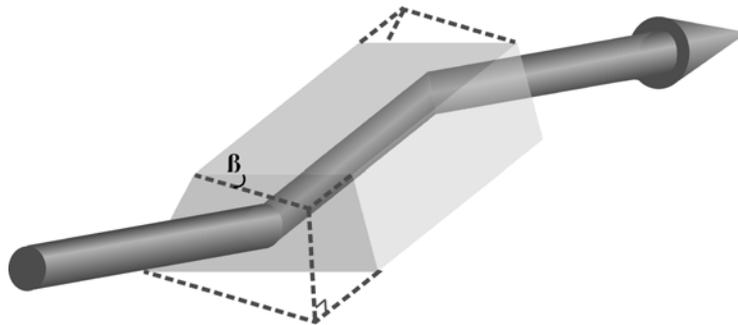
Figure 2.8. The "gold bar" shaped cut of photorefractive crystals suppresses unwanted oscillations arising between
        otherwize parallel faces.

2. 3. 2. 3   Alignment

Computer generated templates placed under the transparent substrate serve as alignment guides to position the filter's components. In order to draw the template, the elements' shapes are carefully measured and then faithfully reproduced as computer objects. Ray tracing on the computer then dictates the position and horizontal tilts of the elements to ensure that there is a closed path. Once the elements are aligned to the template as best as possible, just a little tweaking of the tilts of the mirrors enables the oscillation to start. Figure 2.9 is an enlarged picture of the template used to align the autotuning filter.
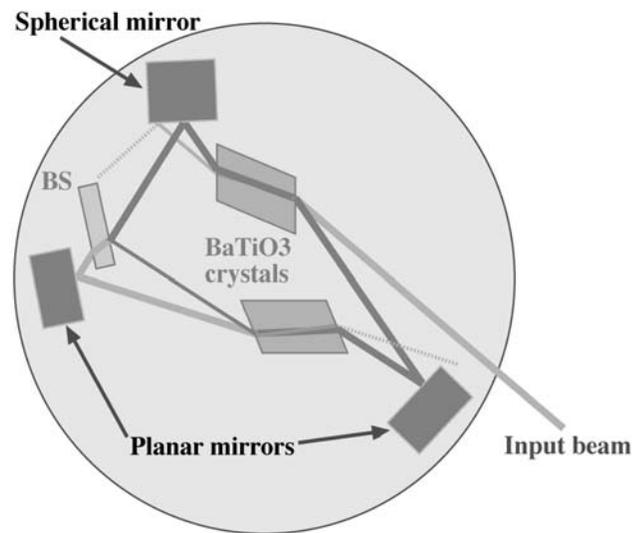
Figure 2.9. Computer generated template placed under the transparent substrate that the filter of Figure 2.7 is built on. The miniature elements of the filter are aligned to it externally before they are glued in place.

2. 3. 3   Results

As mentioned before, our ideal filter lets only the stronger signal oscillate in the ring while completely suppressing the weaker one. Not surprisingly, in practice this is not the case. For example, the spatially finite grating written between one pump beam and the oscillating light in the ring induces the diffraction of a small portion of the other pump beam even if it is not exactly Bragg matched. Experimentally we measure about –30 dB (0.1%) of the input beams diffracting off of each other's gratings.

We evaluate how well the filter separates signals by plotting the intensity ratio of the temporal signals inside the ring versus the input signal ratio carried by the pump beams. The interesting region of this plot occurs for input ratios close to one (0 dB). At exactly 0 dB the filter cannot distinguish between the two signals since the competition for gain is completely unbiased and therefore it also returns an output ratio of 0 dB. However, for ratios near 0 dB the competition for gain plays a strong role. The better the filter, the greater the signal ratio enhancement is around input ratios of 0 dB. In plots of the ring signal ratio in dB versus the input signal ratio in dB, this translates into a higher slope at the origin.

2. 3. 3. 1   Test bed setup

We generated our pump beams by driving two acousto-optic modulators with signal frequency f1 and f2 near 80 MHz. The exact frequencies were 79.99960 MHz and 80.00056 MHz (measured using an HP 8568B spectrum analyzer) resulting in a in frequency difference of less than one KHz. We used 514.5nm (argon laser) and 532 nm (Verdi laser) lasers as our light sources. The first order diffracted beams from the AOMs served as the input signals to our filter devices. Figure 2.10 schematically illustrates the experimental setup.
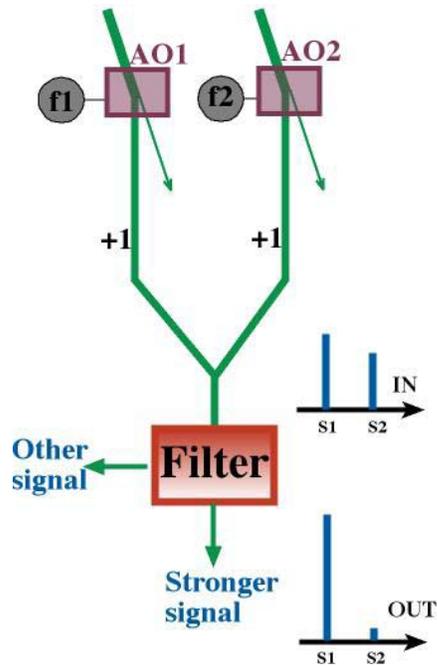
Figure 2.10. Schematic of the AO test bed used to evaluate the separation performance of the autotuning filters.

For the fiberized devices the pump beams were coupled to a multimode fiber with different angles thus ensuring that each beam occupied orthogonal spatial modes inside the fiber. The output of the latter was focused to pump the gain crystal of the photorefractive oscillator. For the free space optics devices, the two pump beams (~ 5 mm cross section diameter) were focused with 15 cm focal length lenses and crossed inside the gain crystal with a three to five degree angle between them.

We chose to monitor the filter's "stronger signal" output. This corresponds to sampling the beam inside the ring. For the fiberized filters using GRIN lenses and the free space optics filters, the sampling beam was the reflection of the oscillating beam off the front face of the gain crystal. For the filters using spherical crystals, the main loop of the oscillator was opened just before the gain crystal and a microslide inserted to deflect some of the ring's oscillating beam. The light was directly detected with a photodetector since AOMs generate amplitude modulated beams. In order to use practical low frequency detectors (ease of

alignment) and spectrum analyzer (ease of access) we lightly modulated the AOMs' driver signals with 15 and 17 kHz sinusoids. We checked that this extra modulation had no effect on the filter's choice of signal.

2. 3. 3. 2   Experiments with the fiberized filters

Figure 2.11 shows a separation curve taken with the filter on the top left-hand side of Figure 2.6. The slope at the origin is 8 dB/dB, thus an initial signal ratio close to unity ($P_1/P_2=1$) gets amplified 6 times. For input ratios greater than 20 dB, the slope tends towards unity (not shown on the graph); the filter does not enhance the signal contrast when their powers are very different to begin with.
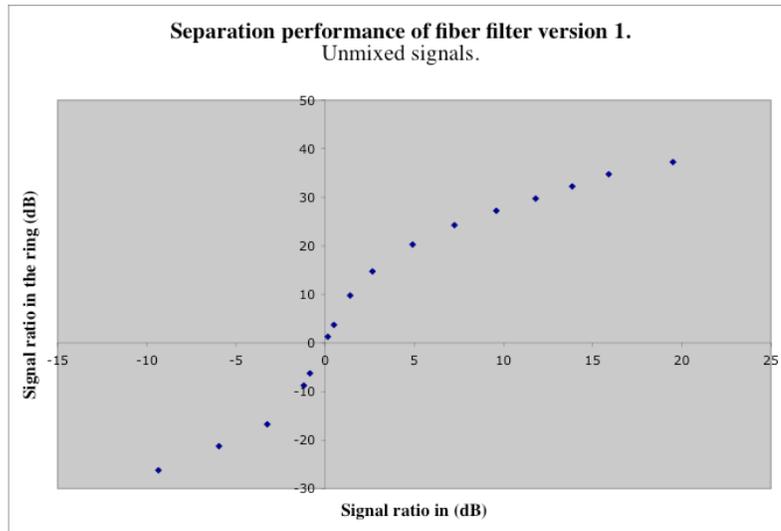
Figure 2.11. Separation curve taken with the filter on the top left-hand side of Figure 2.6

In principle the different input signals to the filter do not need to be separately carried by different spatial modes. The filter's response should be the same when the signals are orthogonally mixed up on the spatial modes. This is further explained in the theoretical section 2. 4. 3. This claim was verified with the setup depicted in Figure 2.12. The AOMs'

driver signals are each split in two equal parts and recombined so that each AOM is driven with some of both signals. To keep the mixing orthogonal, one of the arms has to be delayed by 180 degrees. The mixing matrix then performs a simple 45-degree rotation of the signals in the input space.

The separation results are plotted in Figure 2.13. The data was taken with the second version of the spherical crystal filter shown on the top right-hand side of Figure 2.6. When tested with unmixed signals, the filter yielded the same curve as in Figure 2.11 with an 8 dB/dB slope. The slope at the origin with the mixed signals is slightly less at 6.6 dB/dB. This decrease in performance may be explained by the fact that the weaker signal diffracts more off of the stronger signal's gratings. It is slightly closer to being Bragg matched to them since they are carried by the same spatial modes. This slightly hinders the competition for gain and decreases the slope at the origin in our plots.
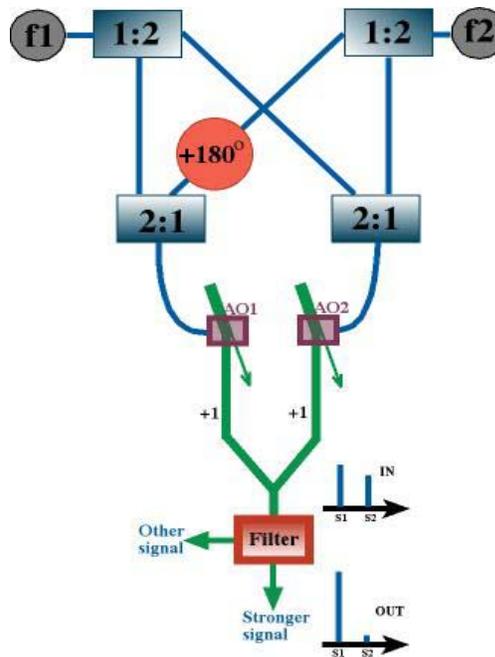
Figure 2.12: AO test bed with mixtures of two signals driving each AO. Each signal is split in two and recombined with half of the other signal. A 180-degree phase shift is added to one half of S2 before it is recombined.
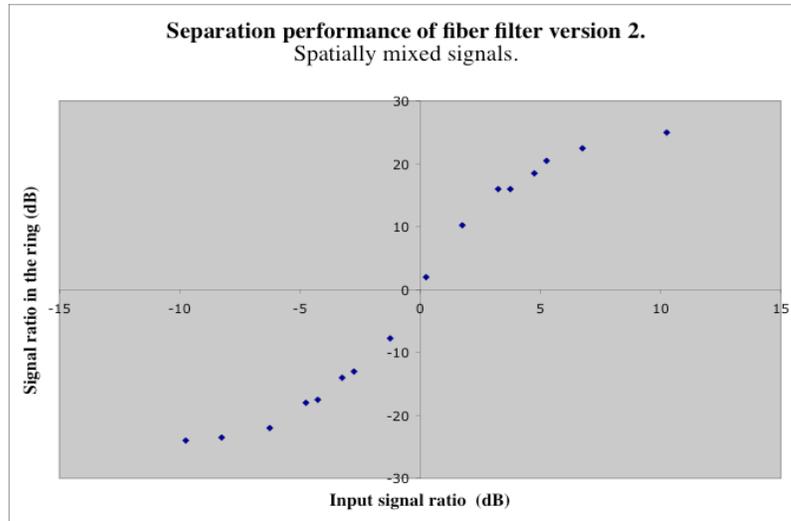
Figure 2.13: Separation curve taken with the filter shown on the top right-hand side of Figure 2.6 and with the test bed of Figure 2.12

2. 3. 3. 3   Free space optics version

The separation performance of the autotuning filter was greatly improved with the free space optics implementation. The slope at the origin in Figure 2.14 is 26 dB/dB, a small signal ratio enhancement of 400. This is nearly a two-order magnitude improvement over the fiberized versions. This performance comes at the price of a more careful alignment of the input beams. The value of the slope is sensitive to the geometry of the pump beams. Good performance requires a shallow angle between the pumps as well as the pumps crossing where they intersect the ring beam. A small change in any of these requirements can negatively affect the slope (down to 10 dB/dB). The fiber versions were not nearly so sensitive to alignment since there was no control over how the speckled pattern folded on itself when it was focused down.
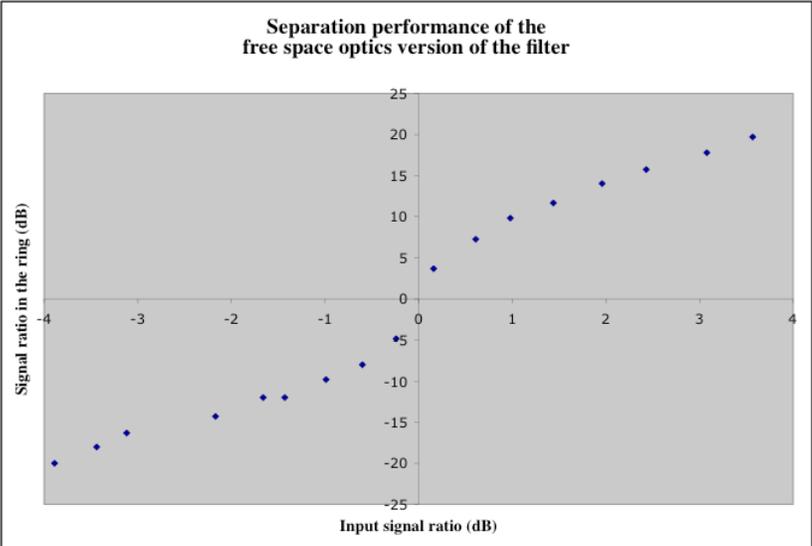
Figure 2.14: Separation curve taken with the filter shown in Figure 2.7

2. 4   Theoretical analysis of the filter

In this section we seek to gain insight about the dynamics of the autotuning filter. The first part explores the parameter space of the filter searching to optimize signal separation performance. This search varies the values of the parameters of the reflexive-coupled photorefractive ring oscillator. We analyze the steady state solutions to the differential equations embodying the dynamics of the filter. This stability analysis consists of a full numerical integration of the differential equations with initial conditions set as perturbed steady state solutions. This search does not conclude with an ideal set of parameters, but with a qualitative description of the influence of each parameter on the filter's separation performance.

The last part of this theoretical section demonstrates (in a somewhat non-elegant fashion, but for the first time) that the autotuning filter separates signals by implementing the mathematical function of principal component separation. Our use of the words "principal component," is a little off from the textbook definition. This last part starts with a clarification of what we mean by them.

2. 4. 1 Varying the filter's parameters for best separation performance

Ideally, the desired filter perfectly suppresses anything but the stronger signal in the ring regardless of the intensity difference between the input signals. When dealing with two signals, a simple ring without a reflexive coupling unit theoretically achieves this. If the available small signal gain in the oscillator strictly equals twice the threshold gain for oscillation, only the stronger component undergoes enough gain for oscillation. Photorefractive gain is shared out proportionally to the relative intensities of each signal.

This "strictly equal" is difficult to realize experimentally, hence the need for extra degrees of freedom supplied by the parameters of a photorefractive reflexive ring.

2. 4. 1. 1   The filter's adjustable parameters

The four adjustable parameters of the filter are:

- Gg, the dimensionless intensity gain supplied by the two-beam coupling gain element;

- L, the multiplicative round trip losses due to absorption, mirror reflectivity (they do not include the splitting from the BS) and possible inserted loss elements;

- m, the pump to weak beam intensity ratio at the reflexive coupling element;

- Gr, the dimensionless intensity gain of the reflexive coupling element.
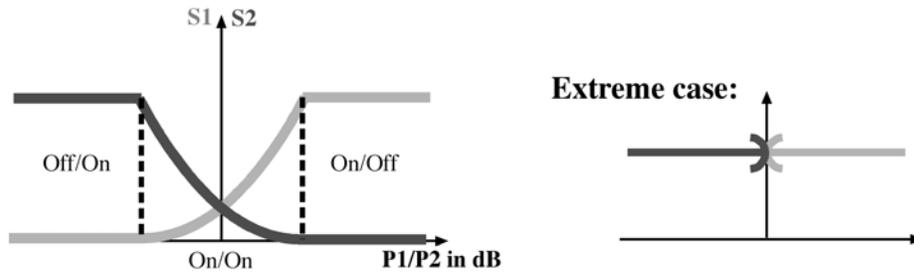
Figure 2.15: Regime of interest in our discussion: when the signal ratio is close to unity both signals may oscillate. Above a critical value $P_1/P_2{}^c$ only the stronger signal oscillates.

We observe the filter's ability to suppress the weaker signal on the same plot used to evaluate the experimental versions of the filter: the plot of the oscillating signals' intensity in the ring S_1 and S_2 versus the input signal intensity ratio P_1/P_2.   Different points in the parameter space produce different types of plots. Figure 2.15 shows the plot type of interest in this discussion. Around a unity-input ratio (0 dB), both signals may oscillate in the ring (the on/on regime).   Above some absolute critical boundary value $P_1/P_2{}^c$, only the stronger input signal oscillates in the ring (the on/off regime). Experimentally, this corresponds to the

stronger signal being the only one writing a grating in the crystals. As discussed earlier, the weaker signal never fully disappears from the ring. A smaller boundary value $P_1/P_2{}^c$ means that the filter achieves a "perfect" stronger signal extraction for input signal ratios closer to unity.

The study presented below explores how the filter's parameters affect this boundary value $P_1/P_2{}^c$. In summary it shows that: a smaller gain Gg is better (too much gain washes out the competition); a larger transmission T is better (non selective losses hinder the competition); a larger splitting ratio m is better (it enhances the importance of the reflexive coupling) and given m, Gg, and T there is an optimum gain Gr.

2. 4. 1. 2   The theoretical "input signal ratio vs. output signal ratio" curve

The boundary value $P_1/P_2{}^c$ is indirectly obtained by observing the Log-Log plot of the signal ratio in the ring S_1/S_2 versus the input signal or pump ratio P_1/P_2. When the input signal ratio approaches $P_1/P_2{}^c$ where the weaker signal disappears from the ring, the output signal ratio will tend to infinity. Since it is symmetric around the origin, we only observe the plot for P_1 greater than P_2. There are two main steps in the acquisition of the data for these plots. First, we find the steady state solutions of the differential equations describing the evolution of the filter. Second, we determine which one makes physical sense by analyzing the solutions' robustness to small perturbations.

The differential equations provided by the plane-wave model of two-beam coupling for temporally and spatially orthogonal signals yields fairly simple formulas for the steady-state values of the signals' intensities. Figure 2.16 defines the notations used in the following formulas.
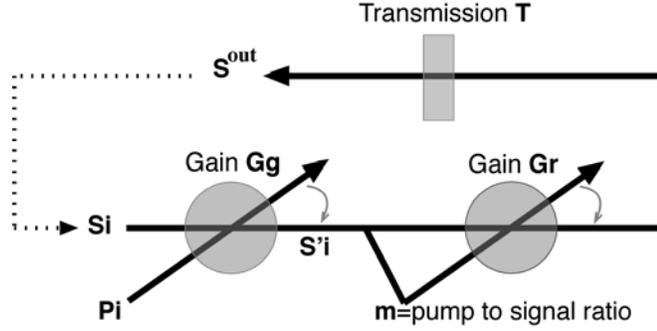
Figure 2.16: Illustration of the notations used in the equations of this section.

The intensity of S_1 just after the gain element is

$$S_1' = \frac{I_1 S_1}{P_1 Exp\left(-Gg\dfrac{I_1}{I_{tot}}\right) + S_1}$$

Equation 2.1

where $I_1 = S_1 + P_1$ and $I_{tot} = I_1 + I_2$. The intensity of S_1 after the reflexive coupling and the ring's losses $L = 1-T$ is

$$S_1^{out} = T\frac{S_1'}{1 + mExp\left(-Gr\dfrac{S_1'}{S_1' + S_2'}\right)}$$

Equation 2.2

The loop gain for S_1 is given by inserting Equation 2.1 into Equation 2.2

$$G_1(S_1,S_2) = \frac{T(S_1 + P_1)}{\left(P_1 Exp\left\{-Gg\dfrac{I_1}{I_{tot}}\right\} + S_1\right)\left(1 + mExp\left\{-Gr*1\bigg/\left[1 + \dfrac{(P_2 + S_2)S_2(P_1 e^{-Gg*I_1/I_{tot}} + S_1)}{(P_1 + S_1)S_1(P_2 e^{-Gg*I_2/I_{tot}} + S_2)}\right]\right\}\right)}.$$

Equation 2.3

The corresponding formula for S_2 is obtained by exchanging the subscripts 1 and 2.

There are four possible steady state classes to consider: no signals oscillating in the ring, both signals oscillating, the stronger signal oscillating by itself, and the weaker signal oscillating by itself. The off/off solution is stable when the round-trip gain is less than unity. This case is of no interest to us and in the rest of the paper it will be assumed that the small signal gain is always greater than the losses.

The on/off solution in which the oscillating signal corresponds to the weaker pump's signal is possible under special conditions of the filter's parameters and for an input pump ratio close to unity. One of these conditions requires that the signal corresponding to the weaker pump start out as the stronger one in the ring. This regime is never observed in our experiments since the filter starts with fanning pump light that carries the signals in the same relative proportions as the pump beams.

The on/off regime with only the stronger signal oscillating is our desired mode of operation for the filter. This solution is given by finding the pairs (S_1, $S_2=0$) that make the gain of Equation 2.3 unity (assuming $P_1>P_2$). However, for input pump ratios sufficiently close to unity, the solution is unstable: if a tiny amount of the weaker signal is introduced into the equations, it grows until the system reaches a stable on/on regime. How close to unity the pump ratio has to be for the on/on regime to be stable depends on the other parameters of the filter as will be described later.

Finally, searching for signals' intensities in the on/on regime is not as straightforward as could be expected. For an input pump ratio close to unity, solving the equation $G_1(S_1, S_2) = G_2(S_1, S_2) = 1$ yields up to three physically allowed solutions. Figure 2.17 graphically represents three such solutions as the three intersections of the two curves $G_1(S_1, S_2) = 1$ and $G_2(S_1, S_2) = 1$. A numerical integration (detailed in Appendix 7. 3) of the full photorefractive dynamical equations for the filter, using these solutions as the initial

conditions, shows that the two extreme solutions (left and right ones on the figure) are unstable and evolve in time to on/off regimes. The middle solution is stable: if we choose initial conditions close to it in signal space, the ring's intensities evolve towards this solution which means it is robust to small perturbations. This stable solution moves to the bottom right of the (S_1, S_2) space as the ratio P_1/P_2 is increased and eventually disappears when the on/off regime is no longer stable.
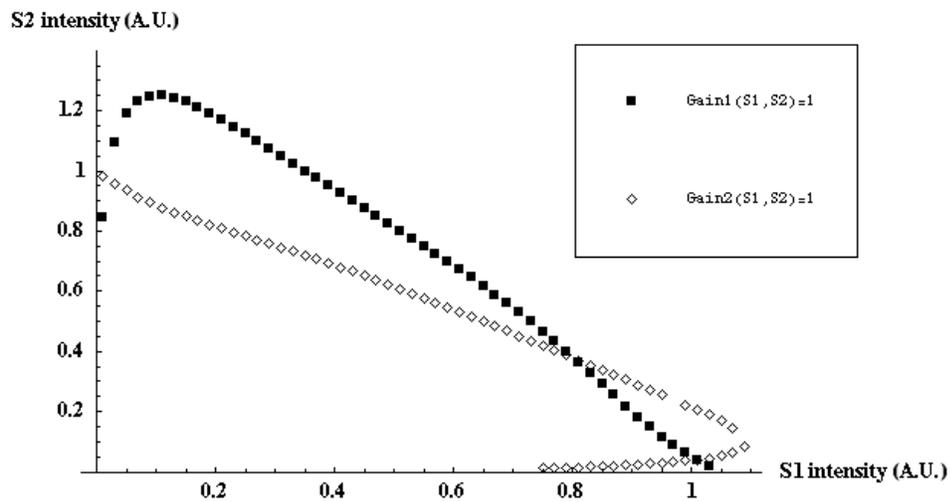
Figure 2.17. The intersection of two curves represent the pairs of (S1,S2) that yield G1=G2=1.

Figure 2.18 illustrates a typical theoretical plot of S_1/S_2 vs. P_1/P_2. In the region where both signals oscillate at the same time the curve is mostly linear. At some critical value of P_1/P_2, S_2 disappears from the ring so the curve jumps to infinity. In general, the smaller this critical value is, the steeper the slope of the linear region. The slope directly reflects the competition between the signals in the auto-tuning filter.
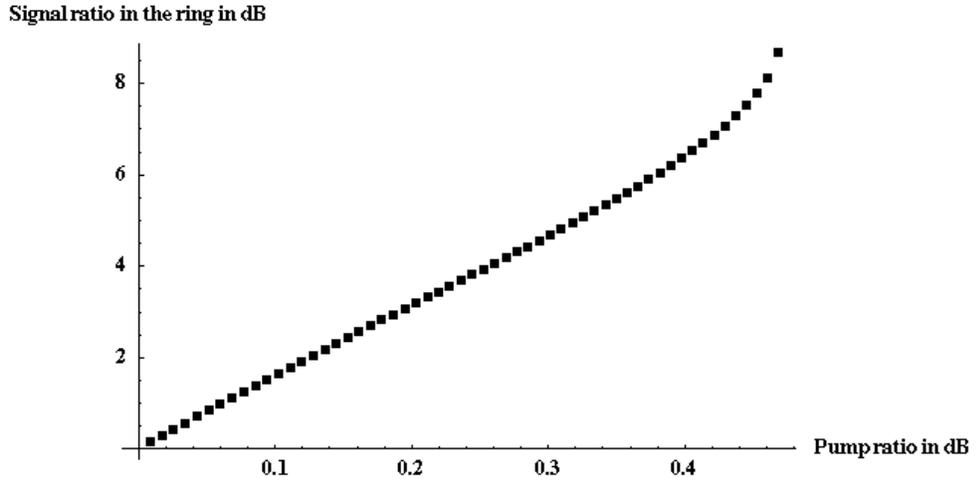
Figure 2.18. The Log-Log plot of the S_1/S_2 vs. P_1/P_2 curve shows a linear region when both signals are oscillating in the ring and a rapid increase toward infinity as the input signal ratio approaches the boundary value where the weaker signal disappears. The parameter values are **$Gr=Gg$**=10, m=50, and T=0.5.

2. 4. 1. 3   Influence of the ring's parameters on the signal competition

This section qualitatively describes the effect of the filter's parameters on the critical value $P_1/P_2{}^c$ of the input signal ratio above which the filter performs a theoretically perfect, stronger signal extraction.

The gain Gg provided by the crystal coupling the input beam to the ring essentially serves to compensate for the losses encountered by the signals in the ring. Keeping all other parameters constant (T=0.5, Gr=10, m=50), Figure x plots the S_1/S_2 vs. P_1/P_2 curve for Gg=9, 10, and 11. Figure 2.19 shows that lowering the gain Gg reduces the on/on region and increases the competition within it. In this particular case, Gg=9 is barely enough gain for the oscillator to self-start.
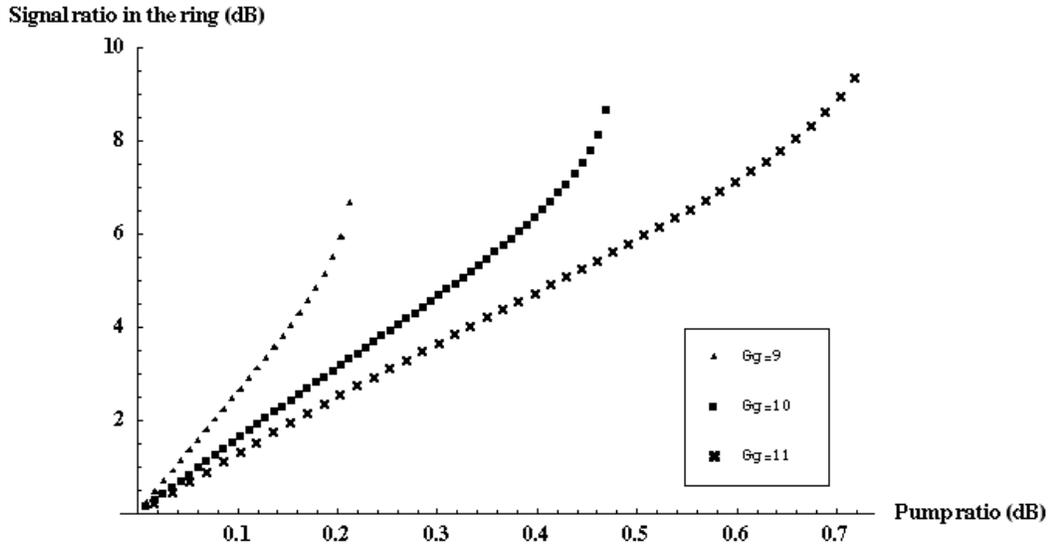
Figure 2.19. S_1/S_2 vs. P_1/P_2 curve for Gg=9, 10, and 11, left to right (T=0.5, Gr=10, m=50).

As mentioned before, photorefractive gain is shared among the signals in proportion to their relative intensities. On one hand, to ensure that there is always a signal oscillating in the ring the minimum available gain must be above twice the threshold gain for oscillation; when the two signals are exactly equal, they are both allowed to oscillate. On the other hand, a very high available gain means both signals' gains are above threshold for a wide range of input signal ratio values— both principal components may oscillate. A smaller available gain Gg is therefore preferable as long as it stays greater than twice the threshold gain.

The passive losses of the filter are embodied by the intensity transmission coefficient T. Keeping all other parameters constant (Gg=Gr=10, m=25), Figure 2.20 plots the S_1/S_2 vs. P_1/P_2 curve for T=0.4, 0.5, and 0.55, illustrating that higher losses soften the filter's competition and increase the critical value of P_1/P_2. This transmission coefficient, being the same for all signals trying to oscillate, does not help the competition between the signals. Lowering T is not equivalent to decreasing the gain Gg from a signal competition point of

view; it actually hinders the competition. The critical input signal ratio decreases as the transmission T increases.
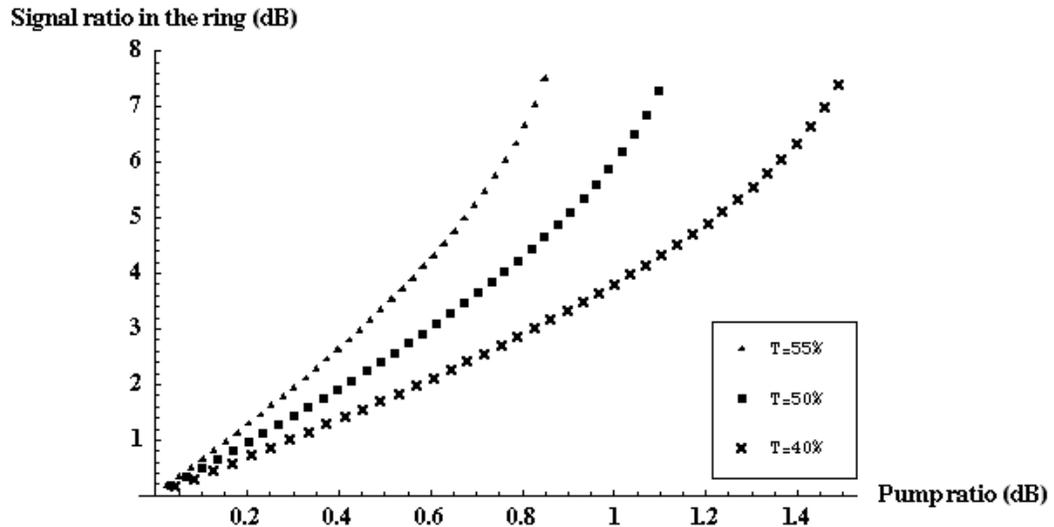
Figure 2.20. S_1/S_2 vs. P_1/P_2 curve for T=0.55, 0.50, and 0.40 left to right ($Gg=Gr$=10, m=25).

The two remaining parameters are closely linked to one another. In order to study their influence on the competition simultaneously, we observe slightly different plots. All the curves have a linear region close to the origin so the gradient of the slope can be estimated by looking at the signal separation performance for only one input signal ratio. In the following figures we chose an input pump ratio P_1/P_2=0.2dB=1.047. Keeping the losses and the gain unit's gain constant (T=0.5, Gg=10), the left hand-side of Figure 2.21 plots S_1/S_2 vs. Gr for different values of m. For any given value of Gr, a larger value of m provides a better signal ratio enhancement. For a given m there is an optimum value of Gr that is higher for larger values of m.

45
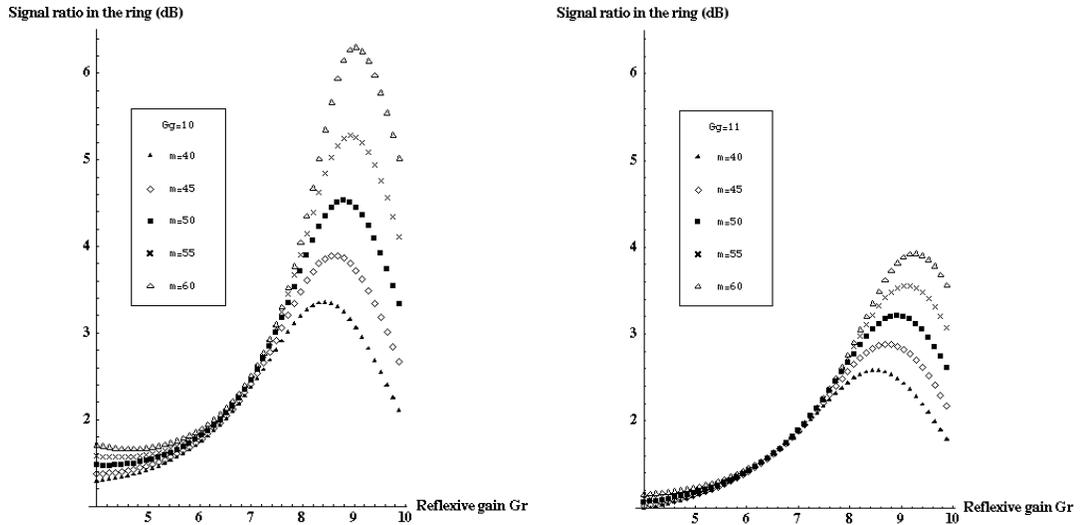
Figure 2.21. Left side: S_1/S_2 vs. *Gr* for *m*=60, 55, 50, 45, and 40 from top to bottom with *T*=0.5, *Gg*=10, and

P_1/P_2=0.2 dB. Right side: same values except *Gg*=11.

The splitting ratio *m* determines the amount of power that is removed from the ring and coupled back to it through photorefractive two-beam coupling. This reflexive coupling process is effectively a selective loss element: the weaker signal undergoes higher losses than the stronger one. Increasing the parameter *m* gives more importance to the signal competition and therefore lowers the critical input signal ratio. Physically, *Gr*'s optimum value may be explained by two facts. One, coupling back to the ring with too little gain increases the overall losses of the filter and lets the two beam coupling at the input gain unit govern the dynamics of the filter. Two, coupling back to the ring with too much gain dampens the selectivity of the reflexive coupling.

Overall the best signal ratio enhancement is obtained with the larger *m* and the corresponding optimum *Gr*. Increasing *m* however, imposes more difficult self-starting conditions on the filter requiring a higher gain *Gg*. The right hand-side of Figure 2.21 shows similar curves to the ones on the left hand-side with a *Gg* of 11 instead of 10. The signal separation deteriorates rapidly indicating a sharp tradeoff between increasing *m* and

46

decreasing *Gg*. The figure also shows that the optimal values of *Gr* are only slightly higher than in the previous case. This implies that *Gr* depends strongly on *m* and weakly on the other parameters of the filter.

2. 4. 2   The filter's principal component extraction abilities

This section compares the experimental results presented earlier with theoretical data obtained with a pure principal component extractor model. A brief review of principal component analysis provides a context in which to describe the function of our autotuning filter.

2. 4. 2. 1   Principal components

Consider a collection of N random time-dependent signals, $\tilde{s}_1(t), \tilde{s}_2(t), \ldots, \tilde{s}_N(t)$, each of which has a zero mean value, i.e., has no D.C. component. In general, these signals may be correlated, meaning here that $\left\langle \tilde{s}_i(t)\tilde{s}^*_{j\neq i}(t) \right\rangle_T \neq 0$, where $\left\langle \ldots \right\rangle_T$ indicates an average over a time *T* much longer than the characteristic inverse bandwidth of the signals. The original collection of signals can be linearly transformed to a new set of signals that are uncorrelated, provided certain mild constraints on the signals are satisfied. One specific de-correlating transformation can be obtained through the correlation matrix

$$\tilde{\mathbf{C}} = \frac{1}{P}\begin{pmatrix} \left\langle |\tilde{s}_1|^2 \right\rangle & \left\langle \tilde{s}_1\tilde{s}^*_2 \right\rangle & \cdots & \left\langle \tilde{s}_1\tilde{s}^*_N \right\rangle \\ \left\langle \tilde{s}_2\tilde{s}^*_1 \right\rangle & \left\langle |\tilde{s}_2|^2 \right\rangle & \mathrm{L} & \left\langle \tilde{s}_2\tilde{s}^*_N \right\rangle \\ \mathrm{M} & \mathrm{M} & \mathrm{O} & \mathrm{M} \\ \left\langle \tilde{s}_N\tilde{s}^*_1 \right\rangle & \left\langle \tilde{s}_N\tilde{s}^*_2 \right\rangle & \mathrm{L} & \left\langle |\tilde{s}_N|^2 \right\rangle \end{pmatrix},$$

Equation 2.4

or

$$\tilde{C}_{ij} = \frac{1}{P}\left\langle \tilde{s}_i \tilde{s}_j \right\rangle_T$$

where the explicit time dependence has been dropped for compactness. The correlation matrix is normalized by the total average power in the collection of signals,

$$P = \sum_{i=1}^{N}\left\langle \left|\tilde{s}_i^2(t)\right|\right\rangle_T .$$

Signal de-correlation is achieved by first diagonalizing the correlation matrix, which can be done in the usual manner by performing a similarity transformation with a matrix *V* formed from the eigenvectors and eigenvalues of the matrix. The eigenvectors of the correlation matrix are commonly referred to as the *principal components* of the signal space while its eigenvalues are referred to as the *principal values*. For the present we assume that the correlation matrix is non-singular, and furthermore that its eigenvalues $\{\lambda_1, \lambda_2, \ldots, \lambda_N\}$ are non-degenerate so that they can be ordered, $\lambda_1 > \lambda_2 > \ldots > \lambda_N$. The eigenvector corresponding to the largest eigenvalue is loosely referred to as the "largest principal component" and similarly for the eigenvector corresponding to the second largest eigenvalue, and so forth.

Corresponding to the matrix *V* is a unique unitary matrix *U* that can be used to transform the original, correlated signals, to a new set of signals $\{\hat{s}_1(t), \hat{s}_2(t), \ldots, \hat{s}_N(t)\}$ that are uncorrelated and furthermore have the property that $\left\langle \left|\hat{s}_i\right|^2 \right\rangle = \lambda_i.$ In the remainder of this chapter we twist the conventional jargon a bit by referring to the transformed signals

themselves as the principal components, e.g., to $\hat{s}_1(t)$ as the largest principal component, $\hat{s}_2(t)$ as the second largest, and so forth.

2. 4. 2. 2   Comparison of experimental results with pure PC extraction
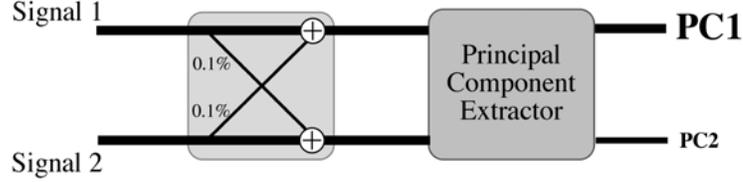
Figure 2.22. Simple model of our filter as a principal component extractor. The mixing on the left hand-side accounts for the spatially finite size of the photorefractive gratings that allows one pump beam to weakly diffract off of the other pump's grating.

Figure 2.22 illustrates how we obtained the theoretical data we are comparing to our experimental data set. The mixing box on the left hand-side of the Figure 2.22 allows for some cross talk between the two input beams to account for the finite size of the gratings written in the photorefractive crystals. It is represented mathematically by a mixing matrix m_{ij}. If we call $\boldsymbol{E}_{source}$ the vector whose components are the temporally uncorrelated signals' field values E_1 and E_2, the input signal vector $\boldsymbol{E}_{in}$ to the principal component extractor is

$$\boldsymbol{E}_{in} = \boldsymbol{M} \bullet \boldsymbol{E}_{source} = \begin{pmatrix} m_{11}E_1 + m_{12}E_2 \\ m_{21}E_1 + m_{22}E_2 \end{pmatrix}. \qquad \text{Equation 2.5}$$

We assume the mixing matrix M is symmetric with $m_{11}=m_{22}=0.9995$ and $m_{12}=m_{21}=0.0316$ (these numbers preserve the intensity of each source signal and make the

intensity cross talk 0.1%). The right hand-side box of Figure 2.22 extracts the largest principal component of E_{in}.

The smooth curve in Figure 2.23 represents the calculated signal intensity ratio in the largest principal component versus the input pump intensity ratio E_1^2/E_2^2. The experimental data points are the crosses in Figure 2.23. The size of the "x" marks covers the measurements' uncertainty of ± 0.5dB.
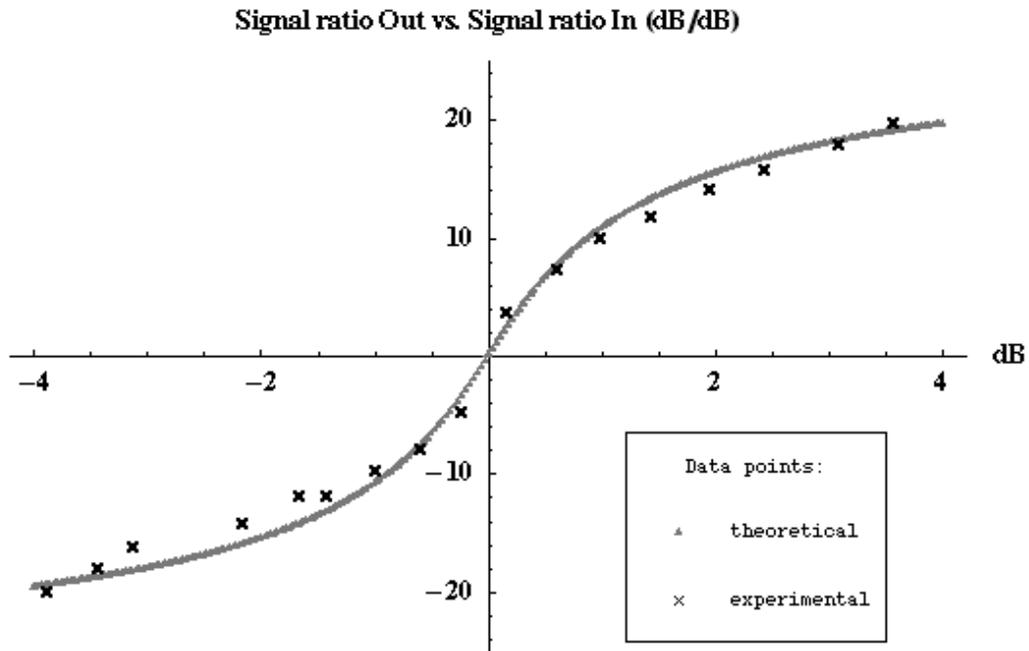
Figure 2.23. Separation performance of the filter. The smooth gray curve shows calculated data points using the first principal component extraction model. The slope at the origin is 15 dB/dB. This is in contrast to the experimental data points (in black) which show a slope at the origin of 26dB/dB.

The model provides a remarkably good fit considering that no photorefractive related equations are utilized. We are comparing the performance of the filter to the purely algebraic technique of principal component extraction. Only the known cross talk between the channels is physically accounted for. The slope at the origin of the theoretical curve is

15 dB/dB corresponding to a small signal ratio enhancement of 32. For the experimental data of Figure 2.23, this ratio is 26 dB/dB. The strict principal component extraction model "underestimates" the role of the competition for gain when input ratios are close to unity.

2. 4. 3 Theoretical arguments to prove the filter's PC extraction capabilities

2. 4. 3. 1 Model and equations

The auto-tuning filter's complex dynamics led us to find a simpler model for its theoretical analysis. We model our filter by a single-mode dispersionless cavity comprising only the photorefractive gain crystal. The single-mode resonator has the same effect as our reflexive coupling on the real cavity— both allow only one spatial mode to oscillate. The dispersionless quality replaces the highly multimode cavity.
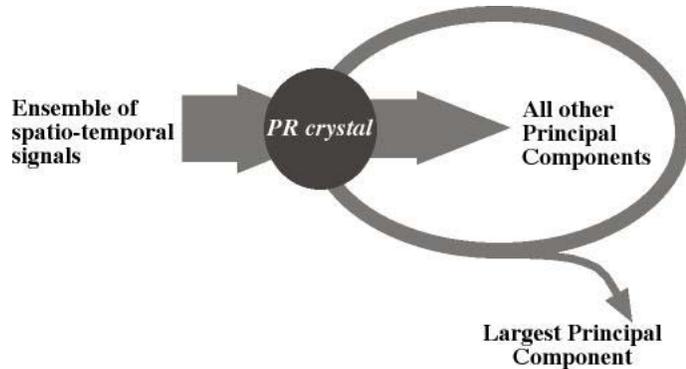
Figure 2.24. Single mode cavity model of our autotuning filter.

The modeled filter depicted in Figure 2.24 has a two-dimensional spatial input as well as a two-dimensional temporal input. The optical pump beams are spatially orthogonal channels that carry mixtures of two temporal signals. The ring brings one other spatial channel to the

system, orthogonal to the input channels. This section answers the question: What is the temporal content of the ring mode given the temporal contents of the input channels?

The answer is that only the energy corresponding to the largest principal component of the input space pumps the ring while the rest of the energy passes through it. We demonstrate this with an input beam containing two spatial channels carrying two temporal signals.

The photorefractive equations

As simple as our filter's model looks, there are still 8-coupled variables to account for. They all depend on both space and time. The numbers 1 and 2 refer to input spatial channel information and the Greek letters α and β refer to temporal information. The variables are:

- 2 gratings G_1 and G_2 in the photorefractive crystal: the two spatial pumps each write a grating with the ring's spatial mode (we assume they do not write a grating with one another)

- 4 variables to describe the pump beams' temporal content: two variables $P_{i\alpha}$ and $P_{i\beta}$ (i=1,2) for each spatial pump

- 2 variables R_α and R_β to describe how much of each temporal signal is in the ring.

First we study the simplest of all input scenarios: temporally uncorrelated signals α and β (they cannot write a grating together) each carried by a different pump. The classical coupled equations describing the photorefractive dynamics relative to our 6 field and 2 grating variables are:

$$\left(\tau\frac{\partial}{\partial t}+1\right)G_1(z,t)=$$

$$\frac{\Gamma}{2I_T}\left(R_\alpha(z,t)P_{1\alpha}^{\ *}(z,t)+R_\beta(z,t)P_{1\beta}^{\ *}(z,t)\right)$$

$$\left(\tau\frac{\partial}{\partial t}+1\right)G_2(z,t)=$$

$$\frac{\Gamma}{2I_T}\left(R_\alpha(z,t)P_{2\alpha}^{\ *}(z,t)+R_\beta(z,t)P_{2\beta}^{\ *}(z,t)\right)$$

$$\frac{\partial}{\partial z}P_{1\alpha}(z,t)=-G_1^{\ *}(z,t)R_\alpha(z,t)$$

$$\frac{\partial}{\partial z}P_{1\beta}(z,t)=-G_1^{\ *}(z,t)R_\beta(z,t)$$

$$\frac{\partial}{\partial z}P_{2\alpha}(z,t)=-G_2^{\ *}(z,t)R_\alpha(z,t)$$

Equation 2.6

$$\frac{\partial}{\partial z}P_{2\beta}(z,t)=-G_2^{\ *}(z,t)R_\beta(z,t)$$

$$\frac{\partial}{\partial z}R_\alpha(z,t)=G_1(z,t)P_{1\alpha}(z,t)+G_2(z,t)P_{2\alpha}(z,t)$$

$$\frac{\partial}{\partial z}R_\beta(z,t)=G_1(z,t)P_{1\beta}(z,t)+G_2(z,t)P_{2\beta}(z,t)$$

where τ is the photorefractive time constant, Γ is the coupling constant of the crystal and I_T is the total intensity present in the medium.

After a short study of this case we will show how any input to the filter can be related to this one. It is then straightforward to find the temporal content of the ring given any temporal content of the input channels.

2. 4. 3. 2   The simple case

The above equations are not, as far as we know, analytically solvable. To find the solutions we consider, as in section 2. 4. 1, all possible steady states in the ring and analyze them one by one. The options are an off/off state where no signal oscillates in the ring; two on/off states where only one of the temporal features is present in the ring and finally an

on/on state where both temporal features oscillate in the ring. The latter may have more than one solution if the ring can support different combinations of the signals.

The only parameters that are not input dependent are the available gain Γl (l is the length of the gratings) of the photorefractive crystal and the round trip losses. Clearly, the off/off state occurs when the small signal photorefractive gain $Exp[\Gamma l]$ is smaller than the round trip losses. This case is not of interest to us. The on/off states of the model filter were thoroughly studied in the past with temporally and spatially orthogonal signals [62]. That paper demonstrates that the only stable on/off state is the oscillation of the temporal signal corresponding to the overall strongest pump.

We now claim that no on/on steady state is possible with our simple input scenario. The on/on state exists if (but not only if) both signals can reach a unity round trip gain in the loop. The gain of each signal in the ring, αGain and βGain, depends on the following parameters and input variables: $P_{1\alpha}^{(z=0)}$ and $P_{2\beta}^{(z=0)}$ ($P_{2\alpha}^{(z=0)}=P_{1\beta}^{(z=0)}=0$ here), the intensity of the ring signals R_α and R_β, the value of Γl and the absorption losses.

For different pairs of $P_{1\alpha}^{(z=0)}$ and $P_{2\beta}^{(z=0)}$, we numerically calculated the pairs of (R_α, R_β) yielding αGain=1 and those yielding βGain=1. Smooth gain curves like those of Figure 2.25 are obtained. However, no combination of values of $P_{1\alpha}^{(z=0)}$ and $P_{2\beta}^{(z=0)}$ (the best case scenario being when they have very similar values), Γl and loss make the curves intersect. This means that no non-zero linear combination of (R_α, R_β) results in unity gain for both temporal signals in the ring at once. The on/on state is not a steady state.
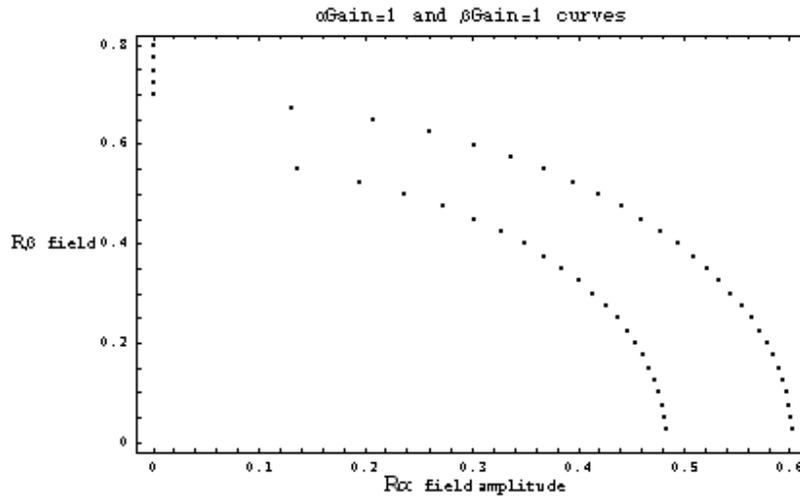
Figure 2.25. Gain curves for two spatially and temporally orthogonal signals.

Summarizing this paragraph, when the filter's input consists of temporally uncorrelated signals carried by different pumps, the circuit always allows only the signal corresponding to the more intense pump to oscillate. The following paragraphs generalize this statement to all spatially orthogonal mixtures of the uncorrelated signals on the pump beams.

2. 4. 3. 3   Spatially orthogonal mixtures

The photorefractive gain crystal in our model sees three spatial beams: one bears the ring signal and the other two carry the input pump signals. These may be represented as three spatial ports and their contents written as the components of a vector. Different vectors are used for different temporal signals. With the notation from the photorefractive-coupled equations, we have two vectors $\mathbf{V}_\alpha$ and $\mathbf{V}_\beta$:

$$\mathbf{V}_\alpha = \begin{pmatrix} R_\alpha \\ P_{1\alpha} \\ P_{2\alpha} \end{pmatrix} \quad \text{and} \quad \mathbf{V}_\beta = \begin{pmatrix} R_\beta \\ P_{1\beta} \\ P_{2\beta} \end{pmatrix}. \qquad \text{Equation 2.7}$$

So far, we have studied input vectors of the shape:

$$\mathbf{V}_\alpha = \begin{pmatrix} R_\alpha \\ P_{1\alpha} \\ 0 \end{pmatrix} \quad \text{and} \quad \mathbf{V}_\beta = \begin{pmatrix} R_\beta \\ 0 \\ P_{2\beta} \end{pmatrix}, \qquad \text{Equation 2.8}$$

and concluded that when we require a unity gain on the first port, either R_α or R_β goes to zero whether $P_{1\alpha}$ or $P_{2\beta}$ is weaker respectively.

Now let us rotate the axes of the pump subspace around the ring mode axis (the first axis here). In the new basis, the sub-vectors' expressions ($P_{1\alpha}$,0) and (0,$P_{2\beta}$) of $\mathbf{V}_\alpha$ and $\mathbf{V}_\beta$, will change to:

$$\mathbf{V}_\alpha = \begin{pmatrix} R_\alpha \\ \cos\theta \cdot P_{1\alpha} \\ -\sin\theta \cdot P_{1\alpha} \end{pmatrix} \quad \text{and} \quad \mathbf{V}_\beta = \begin{pmatrix} R_\beta \\ \sin\theta \cdot P_{2\beta} \\ \cos\theta \cdot P_{2\beta} \end{pmatrix}, \qquad \text{Equation 2.9}$$

where θ is the angle of rotation of the subspace around the first axis. By construction, this rotation leaves any vector that lies in the plane perpendicular to the rotation axis, in that same plane. Any vector that did not previously have a component along the rotation axis will still not have a component along it, in our new basis. In other words, it still holds true in this

56

basis that our steady-state vector will show only one temporal feature along the ring mode axis.

It is straightforward to reverse the reasoning that if we start with a spatially orthogonal mixture of the uncorrelated temporal signals on the pump beams. We can just rotate the spatial pump subspace so that the two temporal signals at the input lie along separate axes (this is the eigen subspace of the pumps). In this space our "simple case" study holds and we can once again conclude that the ring mode's temporal features will correspond to only those of the stronger signal.

2. 4. 3. 4   Non spatially and temporally orthogonal mixtures

What are the temporal features of the ring beam if the two channels carry a linear mixture of some signals S_a and S_b that are somewhat correlated?

The previous paragraphs determined that the filter extracts what it sees as the stronger of two spatially and temporally orthogonal signals. This paragraph establishes that those signals are none other than the principal components of the input space.

First we establish that they are indeed spatially and temporally orthogonal. Let us represent our input space with the vector $\boldsymbol{P}$. The rows describe the temporal contents of input channels 1 and 2 and the symbols S_{ia} and S_{ib} represent how much of each temporal signal is on each channel:

$$P = \begin{pmatrix} Ch_1 \\ Ch_2 \end{pmatrix} = \begin{pmatrix} S_{1a} + S_{1b} \\ S_{2a} + S_{2b} \end{pmatrix}.$$

Equation 2.10

By definition, the principal components are the eigenvectors of the following correlation matrix ρ:

$$\rho = \begin{pmatrix} Ch_1 \\ Ch_2 \end{pmatrix} \otimes \begin{pmatrix} Ch_1^* & Ch_2^* \end{pmatrix}$$

$$= \begin{pmatrix} \left\langle Ch_1^2 \right\rangle_t & \left\langle Ch_1 Ch_2^* \right\rangle_t \\ \left\langle Ch_2 Ch_1^* \right\rangle_t & \left\langle Ch_2^2 \right\rangle_t \end{pmatrix}.$$

Equation 2.11

The eigenvectors are orthogonal by construction. In our case this ensures that they are spatially orthogonal. The particular shape of the correlation matrix also ensures that they are temporally orthogonal. In general, the correlation matrix for complex variables may be written as:

$$\rho = \begin{pmatrix} |m|^2 & mn^* \\ nm^* & |n|^2 \end{pmatrix},$$

Equation 2.12

where m and n in our case are the temporal signals on the two input channels. The eigenvalues of ρ are always 0 and 1 (provided the matrix has been normalized by $|m|^2 + |n|^2$) and the eigenvectors written in the channel basis are:

$$\begin{pmatrix} -\dfrac{n}{m} \\ 1 \end{pmatrix} \quad \text{and} \quad \begin{pmatrix} \dfrac{m}{n} \\ 1 \end{pmatrix}.$$

Equation 2.13

58

The temporal correlation of the PCs is then:

$$
\begin{aligned}
\langle PC_1 \cdot PC_2 \rangle_t &= \left\langle \left(-\frac{n}{m} m + n \right) \left(\frac{m}{n} m + n \right) \right\rangle_t \\
&= -\left\langle \frac{n}{m} m \frac{m}{n} m \right\rangle_t - \left\langle \frac{n}{m} mn \right\rangle_t + \left\langle n \frac{m}{n} m \right\rangle_t + \langle nn \rangle_t \\
&= 0
\end{aligned}
$$

Equation 2.14

Are the PCs the only possible spatially and temporally orthogonal signals obtained from a linear combination of the original input signals? Let us suppose there is another spatio-temporal orthogonal pair (L_1, L_2) that is also a linear combination of the input signals. The spatial orthogonality constraint means that this new set can be written as the rotation of the PCs plus a possibly different scaling factor, G and H, on each vector:

$$
\begin{aligned}
L_1 &= G(\cos\theta \cdot PC_1 + \sin\theta \cdot PC_2) \\
L_2 &= H(-\sin\theta \cdot PC_1 + \cos\theta \cdot PC_2).
\end{aligned}
$$

Equation 2.15

Are these combinations still temporally orthogonal? Using Equation 2.14 we calculate the correlation product:

$$
\begin{aligned}
\langle L_1, L_2 \rangle_t &= \left\langle G(\cos\theta \cdot PC_1 + \sin\theta \cdot PC_2), \right. \\
&\qquad \left. H(-\sin\theta \cdot PC_1 + \cos\theta \cdot PC_2) \right\rangle_t \\
&= GH \cos\theta \sin\theta \left(\langle PC_1^2 \rangle_t - \langle PC_2^2 \rangle_t \right)
\end{aligned}
$$

Equation 2.16

This product is zero only if θ is zero (no rotation) or if the PCs have the same energy. The latter is a degenerate case we have also observed in our experiments. When the two input signals have equal intensity the auto-tuning filter is unable to choose one over the other.

2. 4. 3. 5   Conclusion

To summarize the last few sections, the temporal signal that oscillates in the filter's ring in steady state has the same features as the temporal content of the largest principal component of the input signal space. If the eigenvalues happen to be degenerate the temporal content of the ring may be any linear combination of the principal components. In the non-degenerate case, the largest principal component may be expressed as a linear combination of the original signals S_a and S_b by finding the coordinates of the principal components in the channel basis. The channels' temporal contents are then themselves a linear combination of the signals.

CHAPTER 3

AN OPTICALLY SMART ANTENNA ARRAY

3. 1   Objective

3. 1. 1   Blind Source Separation

When you are in a room full of people your brain has no problem hearing many conversations at once but tuning in to only one. Without much effort, your brain solves what is known as the "cocktail party problem." The common perception of television or cell phone channels is that more of them require more bandwidth: they each need their own separate bin of frequencies. What if all the channels shared the same frequency bin and we possessed a black box that could hear them all at once while listening to any one of them on command? This black box performs what is called blind source separation (BSS). It is capable of distinguishing among a multitude of completely unknown incoming signals that may overlap in frequencies; just as our brain does with audio signals at a cocktail party.

There are various algorithms that solve the problem of blind source separation to some degree. In the last decade a method called independent component analysis (ICA) has emerged as a powerful method for blindly separating signals [65]. It is a computer-intensive method that relies on the statistics of the signals. Its real-time application has mostly been limited to the blind separation of speech type signals; simultaneous processing of multiple

high-bandwidth signals is exceedingly challenging for digital signal processing approaches [66]. Our group is currently working on an opto-electronic implementation of one particular ICA technique. We see no obstacles to operate our system with megahertz bandwidth signals in real time. The first part of the ICA algorithm involves separating the principal components of a signal mixture. Chapter 2 described in length and demonstrated that we have an optical device capable of doing principal component extraction. The primary objective that motivates the work presented in this chapter is the assessment of the design issues and tradeoffs associated with the incorporation of holographic optical signal processing in a microwave receiver. If the incorporation of the autotuning filter in such a system can be demonstrated as practical, then it seems reasonable to expect that the technology will also enable the practical realization of the optical circuitry required for the higher-order signal processing associated with ICA.

3. 1. 2   A portable prototype system

In the following pages, we demonstrate the technology to make a miniature (but not integrated) optical system robust and portable. This chapter describes the making of, and evaluates the performance of a smart antenna array with optical adaptive processing. The array operates at a 10 GHz RF carrier and a 140 MHz IF signal. The input wave is an unknown superposition of a number of uncorrelated signals. These signals are incident from different directions and possibly have changing spatial and temporal characteristics. The output electrical signals are adaptively separated and ordered according to their respective signal strengths. This function is accomplished with the autotuning filter, which is completely internal to the system. The processor and associated electronics are packaged in a standard-size aluminum briefcase with a single external power plug, and consumes less than 50 W of CW power.

Overview of the system

The first stage of our prototype system, schematically shown in Figure 3.1, receives two 10 GHz signals from two distinct sources placed in its far field. Audio signals frequency-modulate the microwaves. The receiving front end consists of a 30-element antenna array that acts as a quasi-optical discrete lens with the detecting antennas placed on its focal arc. The two electrical signals from the detectors are then down converted to 140 MHz and amplified before feeding the second stage of the system.
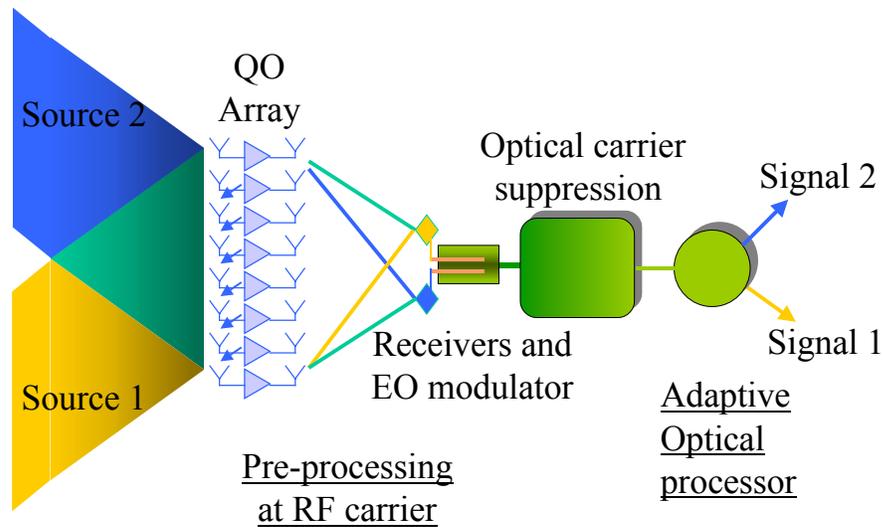
Figure 3.1: Diagram of the prototype optically smart antenna array.

The IF signals are applied to a one crystal, two-channel resonant electro-optic phase modulator. An optical line beam comes out of the electro-optic modulator with its top half modulated with one of the IF signals and the bottom half modulated with the other. Since this is phase modulation the original optical frequency is still present in the beam, necessitating a carrier suppression element in order for the third stage of the system to work properly. The suppression of the optical carrier is achieved by two-beam coupling the signal-bearing beam with a non-signal bearing beam in a photorefractive crystal where the former

beam is the pump (loss port). Although the signals suffer a 3dB loss, the carrier frequency is suppressed by over 50 dB.

The final processing stage consists of the autotuning filter, a 5 cm^2 photorefractive ring oscillator. Two barium titanate crystals in the oscillator combine to extract the principal component of the input signal space, in this case the stronger signal, while passing on the other components. The oscillating beam is sampled and photodetected. Demodulating electronics retrieve the audio signal (originally imposed in the 10 GHz microwave transmitter) from the AC port of the photodetector, which is then sent to a speaker.

3. 2   The microwave front end

3. 2. 1   The transmitters

Although we process 140 MHz RF, we transmit 10 GHz microwaves across space for the practical reasons that it makes the far field of the source much closer in space, and greatly reduces the dimensions of the receiving antenna arrays well as the space needed to demonstrate the system! Figure 3.2 is a photograph of the battery-operated transmitters. The horn antennas as well as the transmitters' circuitry were designed and built in the Active Antenna Lab (Prof. Z. Popovic's lab).
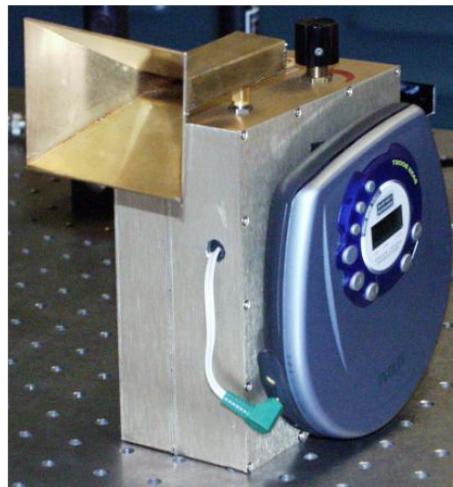
Figure 3.2. Photograph of the battery operated transmitters. The CD player provides the audio signal that
modulates the transmitted microwaves.

Modulation scheme

Portable CD players generate our audio signals (we use only the right or left ear channel). The relatively slow changing voltage of each audio signal is amplified and drives a ~100 MHz Voltage Controlled Oscillator. A mixer imposes this frequency modulated signal as sidebands on a ~10 GHz high frequency signal from a Dielectric Resonator Oscillator.

The output of the mixer is amplified up to 200 mW before being emitted by the horn antennas. Figure 3.3 illustrates the transmitter's circuit diagram and the spectrum that they emit.
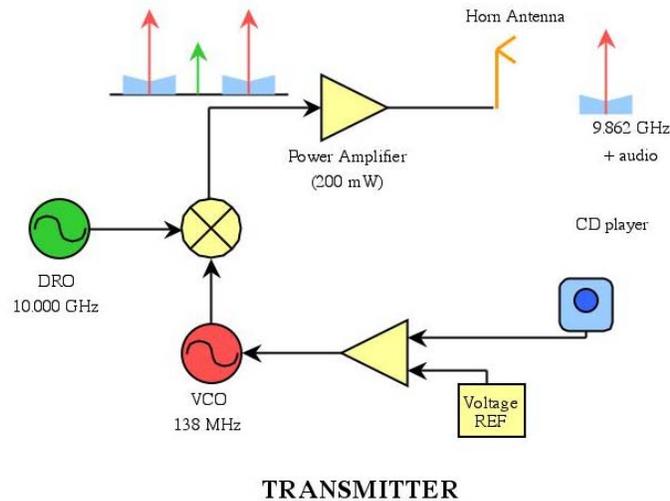
Figure 3.3. Diagram of the circuit that drives the horn antennas.

3. 2. 2 The quasi optical antenna array

3. 2. 2. 1   Principle of operation

The lens antenna array shown schematically in Figure 3.4 is a quasi-optical array analogous to a Rotman lens [67, 68]. It is a passive discrete lens with 30 patch antenna elements, in which the lensing is accomplished with varying delay lines across the array between input and output antenna elements. The left photograph shows the patch antenna elements fed at the non-radiating edges and the microstrip delay lines, which are connected with via holes to the orthogonally polarized patches on the other side of the two-layer lens array.
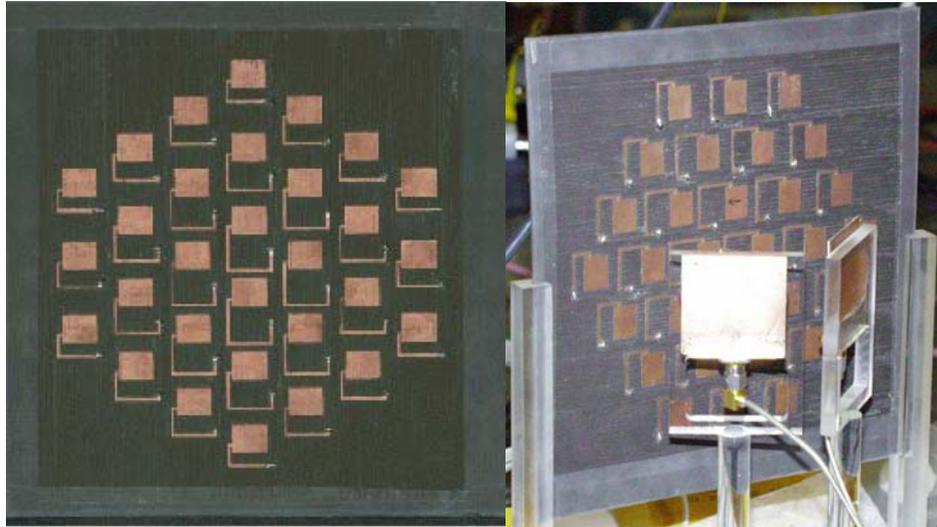
Figure 3.4. Photographs of both sides of a 30-element X-band two-layer quasi-optical lens antenna array with patch antenna elements. The one on the right also shows the ground planes of the receiving antennas placed on the focal arc of the lens array.
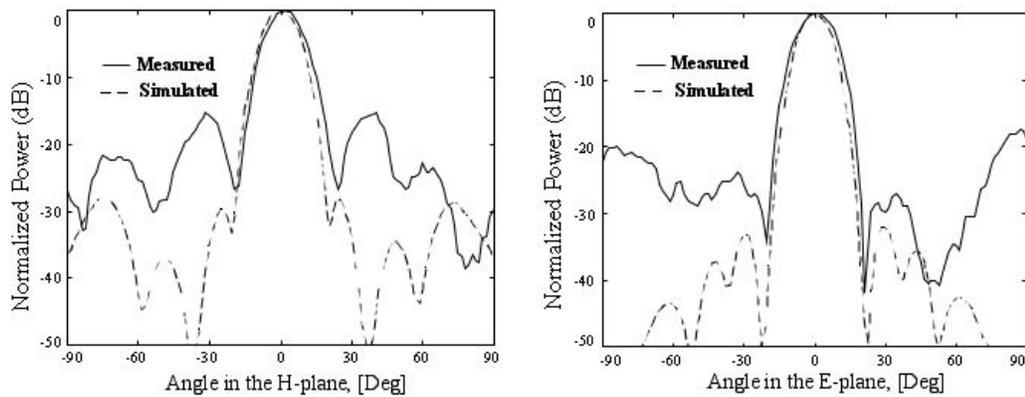
Figure 3.5 Measured (solid line) H-plane (on the left) and E-plane (on the right) radiation patterns at 9.9 GHz have higher sidelobes than the simulated patterns for a uniformly illuminated array (dashed line). This is due to the non-uniform amplitude and phase associated with the near-field spatial feed. The simulated patterns are calculated using the measured radiation pattern of the patch element

3. 2. 2. 2   Antenna data

The antenna is designed for 10 GHz, with a few percent bandwidth (hundreds of MHz). The F-number of the lens is 0.6, corresponding to a focal length of 7.5cm. The array lattice is triangular, with a period of $0.65\lambda_0$, chosen to minimize grating lobes when the beam is scanned. The measured radiation patterns of the lens fed at the focal point with an open X-band waveguide feed are shown in Figure 3.5.

The lens has a number of imperfect focal points, and in our project we use two of these points along the H-plane focal arc to place receivers, each preferentially receiving one spatial beam. The photograph on the right of Figure 3.4 shows the back of two receiving patch antennas placed at those focal points. The two transmitters are placed in the far field of the lens array symmetrically on either side of the array's normal. Each receiver preferentially receives from one of the sources, but some signal from the other source is also present, and referred to as the "cross-talk" signal. The relative amount of the cross talk depends on the spatial separation between sources as well as the radiation pattern of the lens.

3. 2. 3   The active down conversion stage

There are two reasons we need a down conversion stage in our prototype system. One the autotuning filter it is built around processes up to 3 GHz signals, not 10 GHz. Second, the microwave signals are transferred to optical beams by phase modulation. We found no commercial electro-optic modulator (EOM) for green light small enough to fit our size criteria. Since phase modulation was not the focus of our project we built one in the lab but for lower frequencies to simplify the RF circuitry.
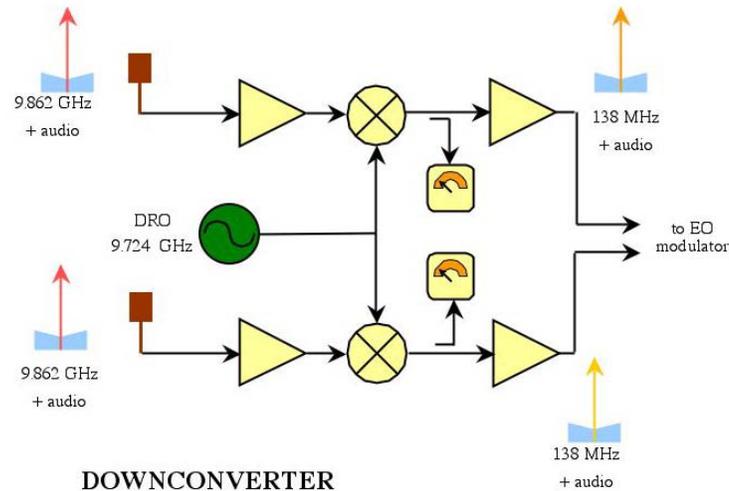
Figure 3.6. Down converting circuit schematics. The amplifiers imediately following the receiving patch antennas are LNAs.

Figure 3.6 presents the down conversion box's schematics. The receiving patch antenna feeds are directly connected by coaxial cable to low noise amplifiers (LNA) at the input of the down conversion box. The LNAs are designed for optimal noise figure (CHA2063 United Monolithic Semiconductors, with a 7-13 GHz bandwidth, 16 dB gain and 2 dB noise figure). The output power for the LNAs at 1 dB-compression point is 10 dBm, with low DC power consumption (40 mA at 5 V). A mixer down converter follows the LNA. The IF amplifiers are CLC522 National Semiconductors wideband variable gain amplifiers and they provide more than 40 dB gain control through a single high impedance voltage input. The ability to control the levels of the signals at the input of the optical processor is important for proper optical processing, as discussed at the end of this chapter. The outputs of the IF amplifiers drive power amplifiers, the 0 to 30 dBm outputs of which drive the electro-optic modulator.

3. 2. 4 Demodulation of the audio signals

The down converted IF signals phase modulate an optical beam so that they may be optically processed. The proper functioning of the autotuning filter requires that the optical carrier be suppressed from the beams. This brings one advantage and one drawback to the process of retrieving the original signals.   With no optical carrier the two microwave sidebands combine to produce an amplitude-modulated beam at twice the IF frequency. This modulation is easily detectable with a fast photodetector. There is no need for a heterodyne detection.   For demonstration purposes, the original microwave signals were frequency modulated with audio signals. The frequency-doubled audio at the output of the filter cannot be sent to speakers without hurting the audience's ears. Figure 3.7 shows the diagram of the circuit that was used to retrieve the original audio signal by performing a square root operation on the detected signal. The doubled IF frequency is first divided by four with a prescaler to give a signal that is half the IF frequency. It is then compared with the halved output frequency of a voltage-controlled oscillator that locks onto the original IF carrier frequency via a phase lock loop. The filtered output of the comparator, which drives the VCO in the PLL, restores the original audio signals.
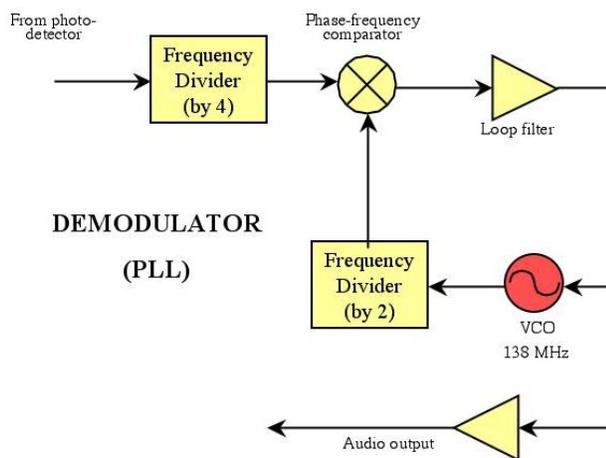
Figure 3.7 The demodulator uses a PLL to lock to the doubled IF frequency. The loop has a frequency divider
that restores the original audio signals that may then be sent to speakers.

70

With only one transmitted signal, the circuit performed well with a high pass filter (>
200MHz) and an automatic amplitude gain control module inserted after the photodetector.
Unfortunately the PLL did not do well at extracting both transmitted audio signals when the
power-contrast between the two IF carriers at the output of the detector was less than 30 dB.
This was the case when the antenna array received the transmitted signals with similar
powers and the system was most convincingly useful.

The audio modulation in the system was added to the demonstration to enhance the
audience's understanding of the system's separation performance. Unclear audio signals at
the crucial moment of the demonstration defeated the purpose. Instead, we chose to show the
audience the spectrum of the IF signals at the output of the photodetector. To allow the real-
time demonstration of the system we filmed the screen of a hand held spectrum analyzer
(Bantham model) with a camcorder and projected its output through a laptop.

3. 3   The EOM and carrier suppression

3. 3. 1   A two channel EO

The 100 MHz IF signals are encoded as phase-modulation sidebands on an optical carrier using a *single* electro-optic crystal modulator as shown in Figure 3.8. The optical line shaped beam passes through a magnesium doped lithium niobate crystal with a pair of horizontal microstrip electrodes. The other side of the crystal has a corresponding pair of grounded microstrips. The top and bottom halves of the beam are spatially modulated with the temporal signals of the two electronic channels.
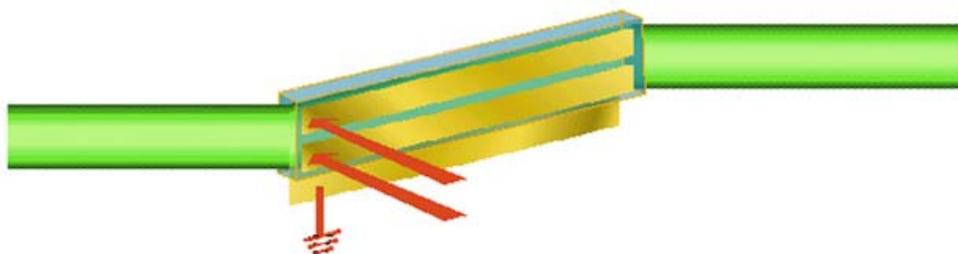
Figure 3.8. Electro-optic modulation: a channelized electro-optic modulator made from magnesium doped
lithium niobate crystal (Mg:LiNbO$_3$) imposes spatial and temporal modulation on the optical carrier.

The electro-optic crystal is a thin slab (0.3 by 7 by 35 mm) where the optical facets have been AR coated in order to minimize back-reflections. The two signal electrodes are two strips, approximately 3 mm wide and separated by about 1 mm. Our first idea to apply these electrodes was to coat these electrodes directly onto the crystal. We evaporated 50 nm of chromium and then gold by electroplating for increased thickness. Something in the process rendered our crystal 90 % opaque. After a couple of trials we abandoned the idea of coating. The electrodes were finally etched out as a pattern on copper covered plastic sheets and

simply mechanically pressed against the crystal. This mount that also houses the electronic matching circuit is detailed in Appendix 7. 4.

3. 3. 2   Resonant matching design

At the operating IF frequency of 140 MHz, the modulator is a lumped-element circuit; the microstrip transmission lines are only a few electrical degrees long. The electro-optic crystal and electrodes are modeled as two capacitively coupled capacitors. The measured capacitance of the 3 mm-wide electrodes is 53 nF. The resonating circuit that matches the electrodes to 50 ohms and cancels the coupling capacitance is drawn in Figure 3.9.
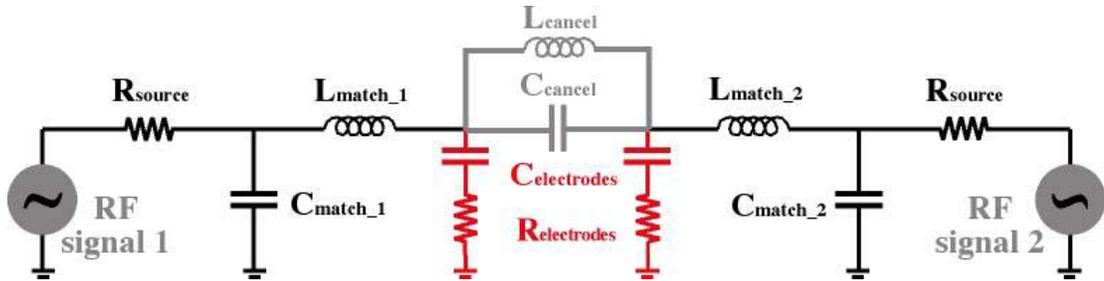
Figure 3.9. The two electrodes of the EO are modeled by a resistor and a capacitor. They are matched to 50 ohms by RC circuits. An LC element cancels the coupling capacitance between the electrodes.

Independently of the suitcase project, a four-channel EO was built using a crystal with the same dimensions. The complexity of such a device lies in the design of a matching circuit capable of canceling coupling capacitances between adjacent and non-adjacent channels. The built device had –10 dB cross talk between the electrodes.

3. 3. 3   EO data

3. 3. 3. 1   Half-wave voltage Vπ

The modulation efficiency has been measured to be about 0.2 rad/V for both electrodes, fed separately with a narrowband matching circuit. This gives a Vπ of 15.7 Volts. The value is close to the theoretical Vπ calculated from the material constants of $LiNbO_3$ and the geometry of the cut. The formula is

$$V\pi = \frac{d}{L}\frac{\lambda_o}{r\,n^3}$$

where the thickness d equals 0.3 mm, the length L equals 30 mm, the wavelength λ_o equals 532 nm, the index n equals 2.2 and the electro-optic coefficient r equals $30.8 \cdot 10^{-12}$ m/V. These values yield a theoretical Vπ of 16.2 Volts.

3. 3. 3. 2   Cross talk

The cross talk between the two electrodes, due to RF leakage, measured with a HP8510 Network Analyzer, is –24 dB. A more pertinent way to measure this cross talk is to measure each channel's spatial distribution of modulation.   We scan the beam after the carrier suppression unit with a photodetector.   Direct detection is possible because the phase modulation without the carrier becomes an amplitude modulation. The scanning results are shown in Figure 3.10.   The two curves on the top plot show the spatial distribution of modulation for each electrode turned on one after the other.   The bottom plot shows the intensity of the beat frequency along the beam when both channels are turned on. The level

of this beat frequency stays low compared to the levels of modulation of the desired signals. This indicates that the cross talk between the channels has been efficiently canceled.
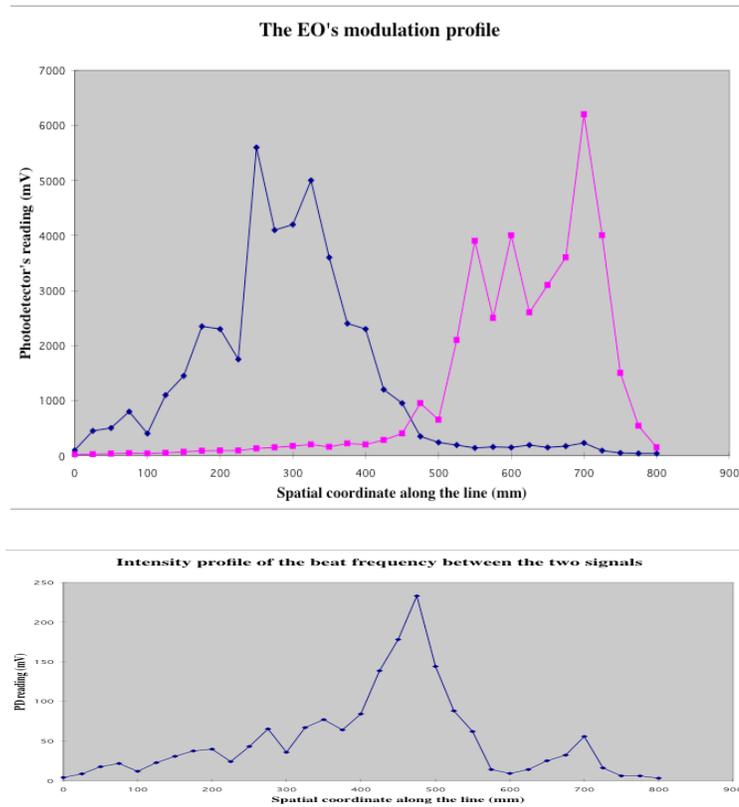
Figure 3.10. Modulation profile at the output of the two-channel electro-optic modulator along the optical beam. The top graph shows the relative modulation strength of each channel along the 7 mm of the line shaped beam that starts at graduation 100=1 mm and ends at 800=8 mm. The channels are driven one at a time. The bottom graph measures the power of the signal that has the beat frequency between the two modulation signals in the same way (so that the graphs' values are comparable) but with both channels turned on at the same time,.

3. 3. 4   The carrier suppression unit

The autotuning filter distinguishes various signals by correlation. The optical carrier that remains after phase modulation is common to all the signal channels and therefore introduces an unwanted false correlation. We implement an optical carrier suppression

system for this reason. Carrier suppression is accomplished through two-beam coupling within a barium titanate photorefractive crystal and uses the principles of an optical novelty filter [2]. The beam coupling interaction takes place between two beams coming from the same laser, one of which has been modulated with the IF signals by the EOM as schematically illustrated in Figure 3.11. As a result of this interaction the modulated beam is transmitted from the crystal with the optical carrier largely suppressed, while the other beam has increased carrier power and also a portion of the IF signal power.
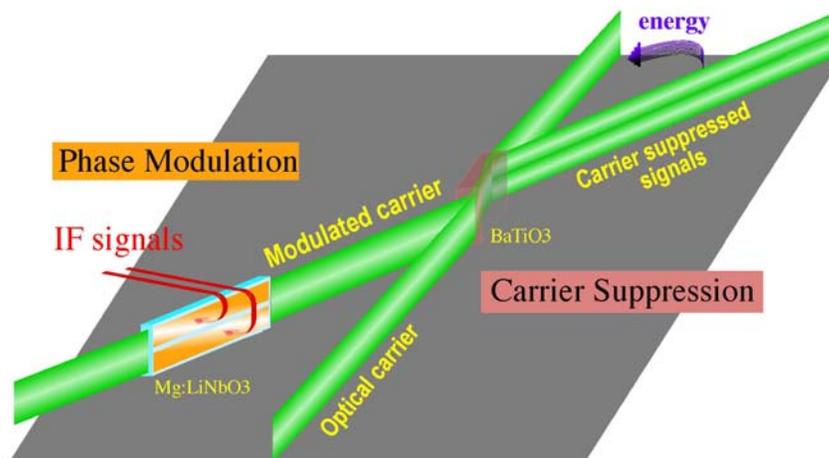
Figure 3.11. Two-beam coupling in a photorefractive barium titanate crystal (BaTiO$_3$) suppresses the optical carrier.

Two-beam coupling coherent beams that have the same frequency, transfers the energy of one beam to the other through a holographic grating that these same beams induce in the crystal. We refer to the beam gaining energy as the "plus" port and to the beam losing energy as the "minus" port. The amount of energy transferred depends on two parameters: the gain of the crystal, G, and the power ratio between the two input beams. Each of these two parameters, in turn, depends on certain geometrical parameters, such as the angle between the beams at which they are incident upon the crystal.

When one beam consists of multiple frequencies, as in the carrier suppression case, the process becomes more complex. However, it is this process of energy transfer that allows us to suppress the carrier from the modulated beam. A complete treatment of the carrier suppression problem has been published in [69]. Here we present a short and intuitive version of the theory relevant to our system. We simplify it further by assuming we have a sinusoidal modulation.

Principle of photorefractive carrier suppression

The dynamics of two beam coupling with a purely real coupling constant occurring between two single mode beams may be pictured in an abstract two dimensional field space as illustrated in Figure 3.12. The horizontal axis represents the fields in the minus port, and the vertical axis represents those in the plus port. Each vector in this space holds all the information about all the fields at the same frequency. In the case of the carrier suppression scenario we have two vectors: the one that describes the optical carrier frequency $\mathbf{E}\omega_c$, has components along the minus as well as the plus ports. The vector related to the modulation frequency $\mathbf{E}\omega_m$ has a non-zero coordinate only along the minus axis. Ignoring bulk absorption, the energy transfer from the minus port to the plus port is a simple rotation. The remarkable fact is that the value of the rotation angle is the same for all the vectors (under the condition that the frequencies are within the photorefractive grating's bandwidth). The angle depends only on the input vectors in a highly nonlinear way. If λ_1 and λ_2 are the eigenvalues of the density matrix of the input vectors defined by

$$\rho = \frac{I_{\omega_c}}{I_{total}}\left(\mathbf{E}\omega_c \otimes \mathbf{E}\omega_c{}^+\right) + \frac{I_{\omega_m}}{I_{total}}\left(\mathbf{E}\omega_m \otimes \mathbf{E}\omega_m{}^+\right).$$

The rotation angle may be expressed as

$$\theta = Arc\tan\left[e^{(\lambda_1-\lambda_2)\Gamma l}\tan\theta_o\right],$$

where θ_o is the input angle of ρ's eigenvector associated with the largest eigenvalue λ_1, Γ is the coupling constant and l is the length of the grating. This formula describes how photorefractive two-beam coupling transfers energy such that the eigenvector associated with the largest eigenvalue tends toward the plus axis. Only infinite gain perfectly aligns the two.
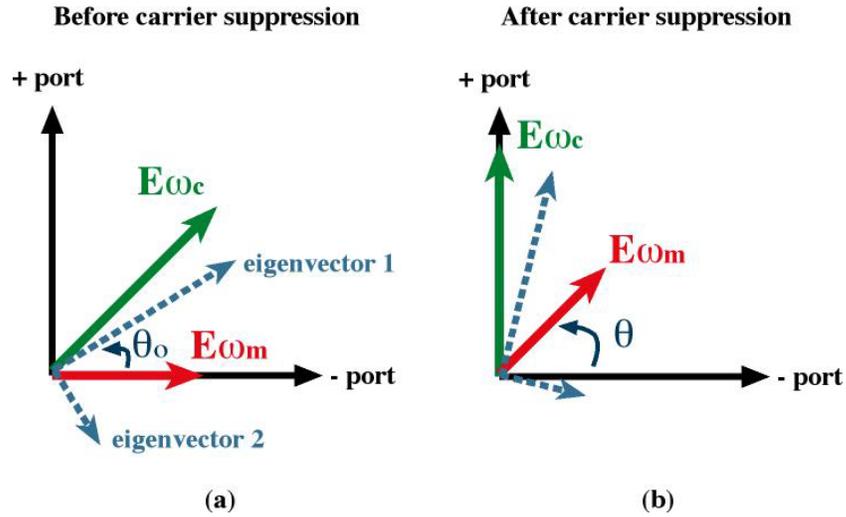
Figure 3.12. 2D representation of single mode two-beam coupling. (a) In the case of carrier suppression the input to the minus ("-") port is a modulated laser beam while the input to the plus ("+") port is a non-modulated beam from the same laser. (b) Nonlinear coupling between the beams causes the energy in the carrier at the minus port to be transferred to the plus port at the output.

In our carrier suppression picture our largest eigenvector lies somewhere between $\mathbf{E}\omega_c$ and $\mathbf{E}\omega_m$. With enough gain (i.e., a long enough grating) the rotation representing the energy transfer will align $\mathbf{E}\omega_c$ along the plus axis as illustrated in Figure 3.12.b. At that point, $\mathbf{E}\omega_c$ has no component along the minus axis; it is "perfectly" suppressed from the initially

78

modulated beam. The picture also shows that this suppression comes at the cost of losing some of $\mathbf{E}\omega_m$'s energy from that beam. The quantitative version of what we just described shows that the gain to achieve this carrier suppression is minimum when the intensity at the plus port initially equals the intensity at the minus port no matter what the modulation depth of the modulated beam is. The value of this minimum gain decreases as the modulation depth increases. This fact makes the experimental implementation of this photorefractive carrier suppression very convenient: the intensity ratio between the non-modulated and the modulated beam only needs to be adjusted once. The other convenient fact about this way of suppressing the carrier is that photorefractive crystals adapt to slow drifts of the laser beam's frequency. This is a major advantage over Mach-Zender configurations.

Very careful experiments resulted in 70 dB of carrier suppression. This means that the carrier on the modulated beam was decreased by seven orders of magnitude resulting in the best carrier suppression reported in the literature to date. Not so careful alignment of the photorefractive carrier suppression still yields 50 dB suppression. This was enough, in our case, to dwarf the carrier compared to the modulated signals at the input of the autotuning filter. Figure 3.12.b shows that rotating all the vectors by the 45 degrees, required for best carrier suppression, adds 3 dB of loss on the modulated signals. This is physically explained by the fact that even though the signals cannot write a stable grating with the carrier, they can read a grating written by the two carriers (a 0.5 cm finite length grating has hundreds of GHz bandwidth.) Some of the signals' energies are therefore lost to the plus port.

3. 4   Design of the optical stage

Building a miniature optical system involved resolving two main types of problems. One was designing the optical layout with space constraints. This is what I called optical mode matching: obtaining a specific beam size and divergence in a specific place. The second type of problem was purely mechanical. Miniature systems are not common enough that optics companies carry a wide assortment of miniature mounts and subsystems. Many of the mechanical parts, that are usually pulled out of a drawer or ordered from a catalog, had to be replaced with "homemade" versions. Most of these mechanical designs are described in the appendices.

3. 4. 1   The optics

3. 4. 1. 1   A line shaped beam

A natural choice for the system's optical set up would be to mirror the electronics layout by splitting the laser beam in two and propagating these two channels all the way to the autotuning filter. We chose a single vertical line-shaped beam instead. This facilitates coupling in and out of the electro-optic crystal and simplifies suppressing the carrier from two beams at once. The geometry is shown in Figure 3.11 above. This arrangement also avoids having to use two sets of lenses any time the beam needs shaping. A 30-degree line generator (Edmund Scientific), shown in Figure 3.13, creates our beam.

Figure 3.13: These line generators create a 30-degree fanning beam that is 0.8 mm wide.

The line generator is followed by a horizontal cylindrical lens that collimates the beam's height through out the system to 6 mm in order to fit in the $LiNiO_3$ EO crystal. The photorefractive crystal configured for carrier suppression (45-degree cut based on the group's past experience with novelty filters) is cut to accommodate this dimension. It also has Brewster windows that are oriented to reduce reflections for the modulated beam.

3. 4. 1. 2   Mode matching with 3-lens subsystems

Certain elements in our system require very specific beam sizes. For example, the line generator needs a 0.8 mm focused beam, and the EO crystal requires a beam less than 0.3 mm wide over a distance of several centimeters. A gaussian laser beam is fully characterized, at any point in space, by its waist W and radius of curvature R. These two parameters are classically embodied by the complex parameter **q** defined by

$$\mathbf{q}(z) = \frac{1}{\mathrm{R}(z)} + \frac{1}{i\mathrm{W}(z)}.$$

This is particularly convenient because propagating **q** through a simple lens system may easily be done with the ABCD matrix formulation. The formula relating the input and output **q** parameters is

$$\mathbf{q}^{out} = \frac{\mathrm{A}\mathbf{q}^{in} + \mathrm{B}}{\mathrm{C}\,\mathbf{q}^{in} + \mathrm{D}}$$

Equation 3.1

Transforming the input **q** into the desired output **q** using three lenses gives theoretically 7 adjustable parameters. Three parameters determine the focal lengths. Four other parameters define the positions of the lenses and the location at which the beam has the desired input and output **q**. Our constraints are the total length between the locations of the input and output **q**, and two equations provided by the real and imaginary parts of Equation 3.1. It may seem at first that we do not need 7 adjustable parameters when we have only 3 constraints. However the three focal lengths are only partially adjustable since we wished to use common lenses available through catalogs. The choice of three lenses was simply a good compromise between the number of elements and the time spent optimizing their positions. Figure 3.14 shows a picture of a three-lens subsystem. The lenses are placed in cylindrical mounts that have the exact same outer diameter. This enables a single v-groove to keep them all centered, while allowing one degree of translation for position adjustment.

Figure 3.14: 3 lens subsystem. The lenses are placed in cylindrical mounts that have the exact same outer diameter to keep the lenses centered relative to each other. The v-groove allows only one translation.

3. 4. 2 The mechanics

The base plate and the clamping mechanism

For our prototype system to be robust and portable enough to travel, we had to ensure the good alignment of the optics was solidly fixed and that the system functioned properly when not on an optical cushioned table. The first problem was solved with an original clamping system from underneath. The mechanism resembles an upside down table clamp. The left of Figure 3.15 shows a photograph of the clamps. Each subsystem has a 1/4-20 screw attached to it that goes through the base plate. The clamps pull on a ring that threads onto this screw as illustrated on the right of the figure. Designing a simplified miniature optical table solved the second problem. It decouples the optical stage from any relevant and reasonably expectable vibrations the suitcase could be submitted to. Vibration modes of the plate itself, which is a one big piece of steel, are avoided by carving out a girder structure out of the bottom and all the holes for the screws mentioned above help too. Outside vibrations are cut off by isolating the plate from the rest of the suitcase with foam feet. The plate is held in place with c-shaped metal ribbons (see appendix 7. 5 for details).
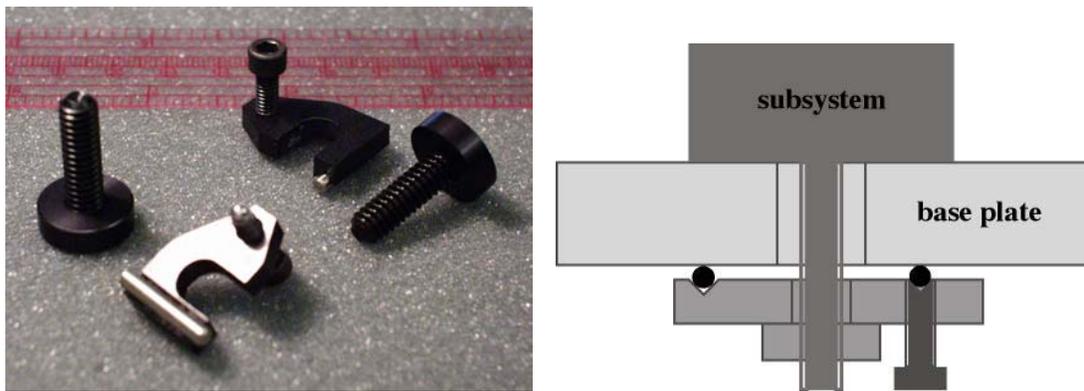
Figure 3.15: Photograph and picture of the inverted table clamps. A 1/4-20 screw with a threaded ring attach to every subsytem on the base plate. A u-shaped piece with an integrated screw pulls down on the ring thus immobilizing the sub sytem on the base plate.

Layout of the optics

Figure 3.16 shows the 8x11 inch optical stage. The laser is a frequency doubled solid-state laser emitting 150 mW of continuous power at 532 nm (Compass 315M-150 from Coherent).
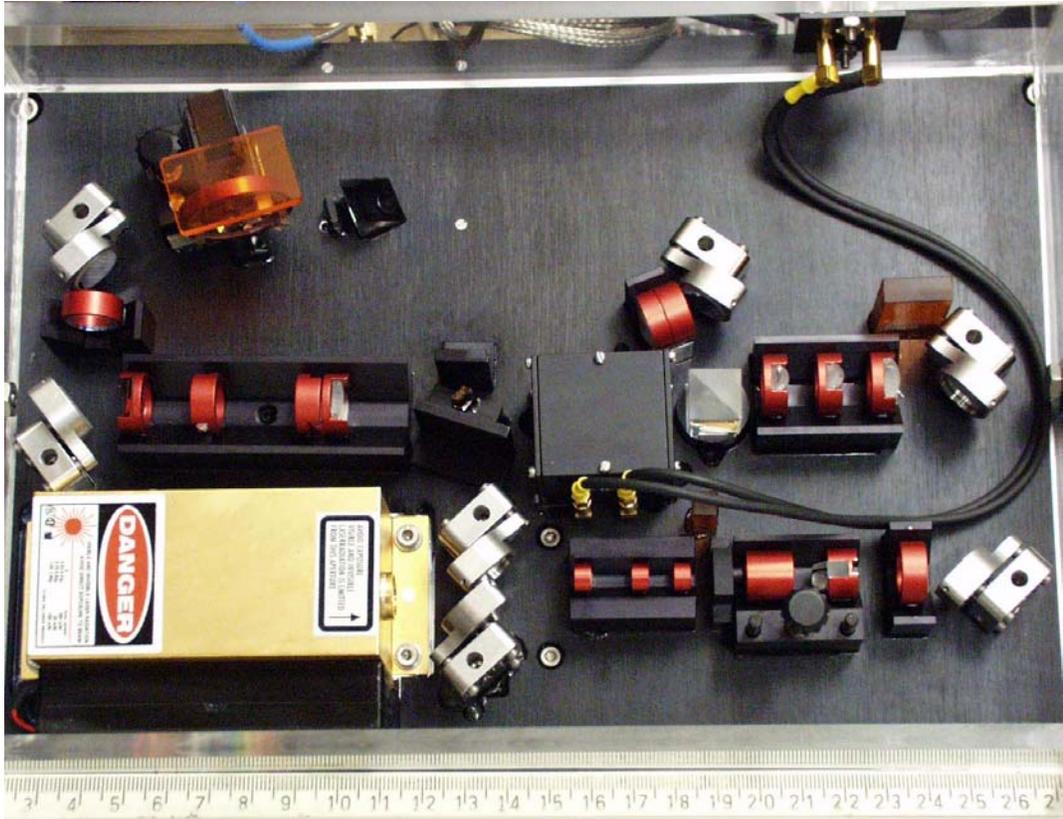
Figure 3.16: Photograph of the 8x11 inch optical stage.

The first three spherical lenses after the laser mode-match the laser beam for the line generator. Three more cylindrical lenses shape the beam for the EO crystal housed in the box connected to the two coaxial cables bringing in the IF signals. A beam splitter divides the laser beam in equal parts before one half enters the EOM. The two beams are then coupled in a photorefractive crystal so that the carrier is suppressed from the modulated beam. The last set of lenses and the half wave plate prepare the beam for the autotuning filter's input. The

filter sits sideways under the orange roof that absorbs reflected or scattered green light. Finally, a 90-degree prism sends the output of the filter to a fast 300 MHz photodetector placed under the base plate. The laser's control electronics and power supply also hide beneath the plate.

3. 5   System performance

3. 5. 1   The suitcase

Figure 3.17 is a photograph of the adaptive antenna processing system. The system is packaged in a 13x18x6 inch aluminum briefcase with a single power plug.   The system (mostly the laser) consumes a maximum of 90 W of power at start up.   The power consumption drops to 50 W after 4 minutes.
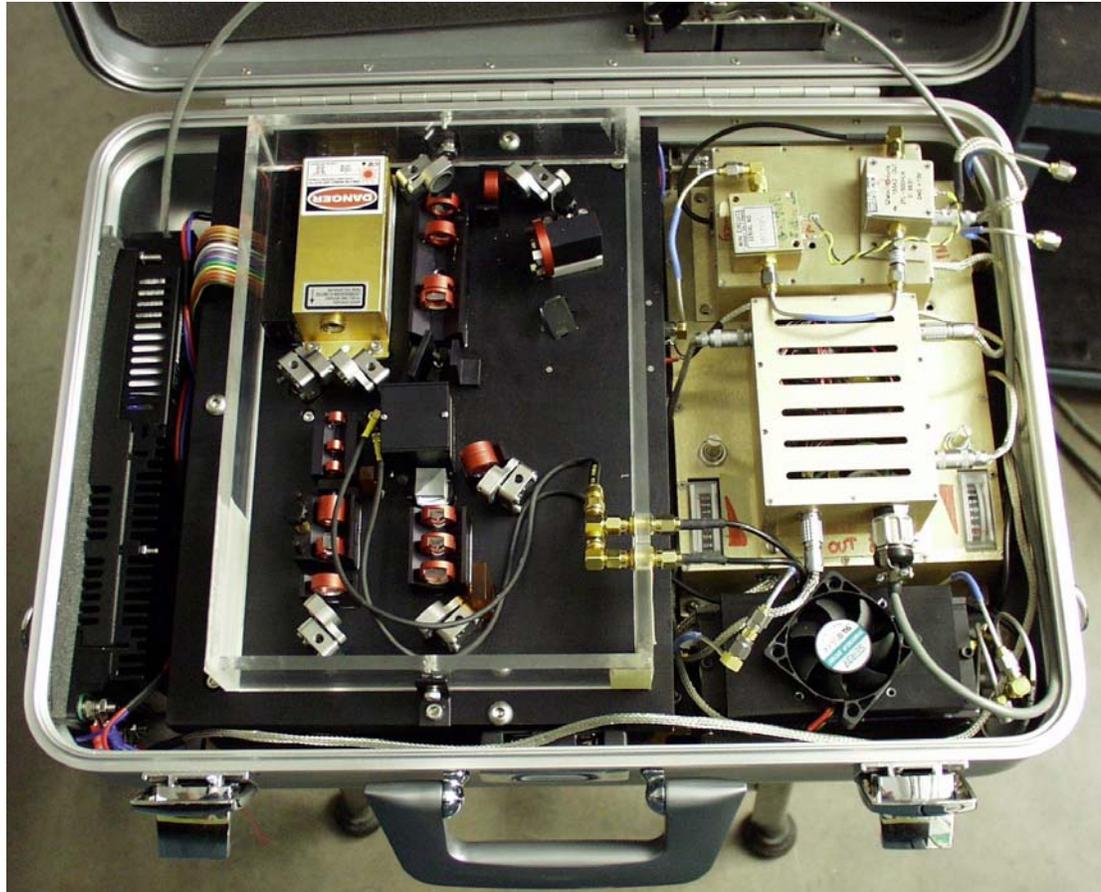
Figure 3.17: Photograph of the "suitcase project." The two coaxial cables visible in the top right corner receive electrical signals directly form the patch antennas placed on the focal arc of the antenna array. The bigger gold-colored box contains the LNAs and the down converting electronics. The output is amplified by power amplifers sitting under the visible cooling fan (there is another one under the

optics). The two electronic channels then drive the EOM in the optical stage to the left of the picture. The suitcase measures 13x18x6 inches when it is closed and plugs into a regular wall outlet, consuming less than 50 W of power.

The electronic portions of the system sit on the right side of the case, while the optical portion sits to the left of center. The laser power supply is visible at the far left, while the power for the electronics is distributed from the gold box with stripe-shaped vents in its cover. A fan under the optics combined with a fan on top of the power amplifiers create enough of an air flow to keep the suitcase's elements cool.

Figure 3.18 shows the system as it was tested end-to-end. The processor sits towards the left of the photograph, with the antenna lens array sitting just to its right. On the right are the two transmitters with their horn antennas. The two transmitters are placed symmetrically about the antenna array boresite.

Figure 3.18: Configuration of the system as it was tested in the laboratory.

3. 5. 2   End-to-end characterization of the prototype

The outputs of our two-channel system do not, in general, recover the original source signals in the face of multi-path and other interference effects. We built this prototype around the autotuning filter and not around the full circuit performing independent component extraction for reasons mentioned in the introduction of this chapter. The output of our adaptive processor always provides the principal components of the signal space. The principal components are proportional to the two transmitted signals if and only if three conditions are satisfied: 1) the sources are independent, 2) they produce different received powers and (3) the signals incident on the optical processor correspond to *spatially orthogonal* signals. Condition 1 is always satisfied in practice unless some spurious effect causes an apparent correlation (such as the presence of the optical carrier, in our case). The limits imposed on our system by condition 2 are already revealed by the signal extraction curve of the auto-tuning filter, which shows a finite slope through the origin, discussed in the previous chapter. This requirement reflects a fundamental limitation of principal component analysis. Condition 2 can be relaxed with a more sophisticated optical circuit capable of higher-order (than correlation) signal processing. The fact, though, is that this requirement is usually satisfied in practice. Condition 3 is another matter. It reflects a particular limitation of our holographic circuit that needs a more complicated optical circuit geometry to be overcome. As it stands, condition 2 is the most confining one and is the focus of the end-to-end characterization of the system.

We assessed the performance of the system by taking signal extraction curves reminiscent of the enhancement of the auto-tuning filter (see previous chapter) for three different angles between the two transmitters. Figure 3.19 provides a context in which to describe the measurements. In general, each of the two detector outputs will be composed of

a linear superposition of the transmitter signals. Since the transmitted signals are uncorrelated, one can write:

$$R_1 = R_{11} + R_{12}$$
$$R_2 = R_{21} + R_{22}$$

where R_{jk} is the received signal power from transmitter T_k after down conversion to the IF.
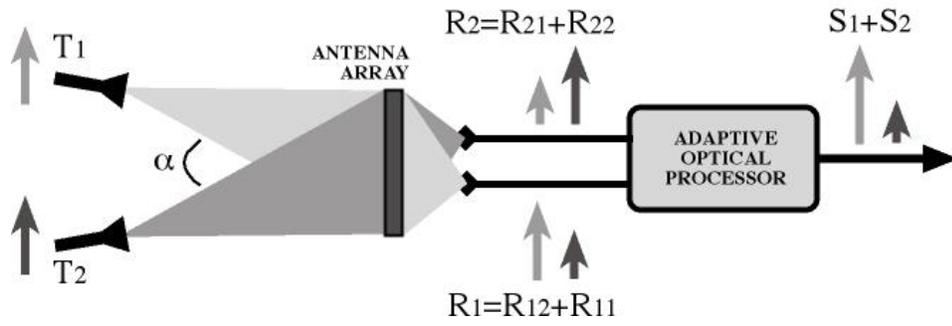
Figure 3.19. Diagram defining the context of the end-to-end system measurements.

With a large angle between the transmitters, the received power R_1 at the IF on one channel of the receiver is primarily from transmitter T_1 while the received power R_2 at the other channel is primarily from transmitter T_2. In other words, for equal transmitted powers R_{12} and R_{21} are small compared to R_{11} and R_{22}. We measure a cross talk between receiving channels by setting the transmitter so that the received powers R_{11} and R_{22} are equal and then determine $C_j = R_{jk} / R_{jj}$ ($i \neq k$). From the symmetry of our experimental arrangement, we expect the two values of cross talk to be the same, $C_1 \approx C_2 \equiv C$. Table 1 shows this cross talk C for three different angles. At the largest angle of 48° between the transmitters the cross talk is −15dB. At the smallest angle of 20° it is 0 dB.

In this experiment, as in the previous chapter, we optically sample and detect only the power in the filter's ring, which provides the higher power of the two principal components. We define the input signal power ratio as R_{11}/R_{22}. We define the output power ratio S_1/S_2, the ratio of detected power corresponding to the temporal signals of the two transmitters T_1 and T_2. Ideally this output ratio would be zero or infinity, depending one which signal was larger, that received from T_1 or that received from T_2 but otherwise independent of the input ratio.

Qualitatively, we can expect that the principal components will become more and more a superposition of the two source signals as the transmitters are moved closer together in angular space. When they are at the same angular position, there is nothing available to the optical processor to distinguish one source from two sources. Figure 3.20 plots the measured output signal ratio versus the input ratio for three different angles between the transmitters. The two curves for the larger angles have a characteristic "S" shape. When the received signals have identical powers they are indistinguishable by the auto-tuning filter (this is because the two eigenvalues of the signal correlation matrix are degenerate). However, even a small power difference can provide the needed distinction. Of particular interest therefore is the slope near the origin of the curve. For the largest angle of incidence it is 76 dB/dB. This means that if the signals differ by 0.04 dB at the input to the auto-tuning filter, their ratio is enhanced to about 3 dB at the output. Once the output ratio is above 10 dB or so, the enhancement begins to level off. With the smaller angle between the transmitters of 35° the slope at the origin of the "S" curve becomes much shallower. The value of this slope is 6.1 dB/dB. For an angle of 20° the "enhancement" is smaller with a value of about 1.3 dB/dB. At this latter angle we note that the cross talk is 0 dB, meaning that all four IF powers R_{jk} are about the same size for equal transmitted powers. It would seem for this smallest angle that the two transmitters are unresolved by the antenna and therefore their two signals should be
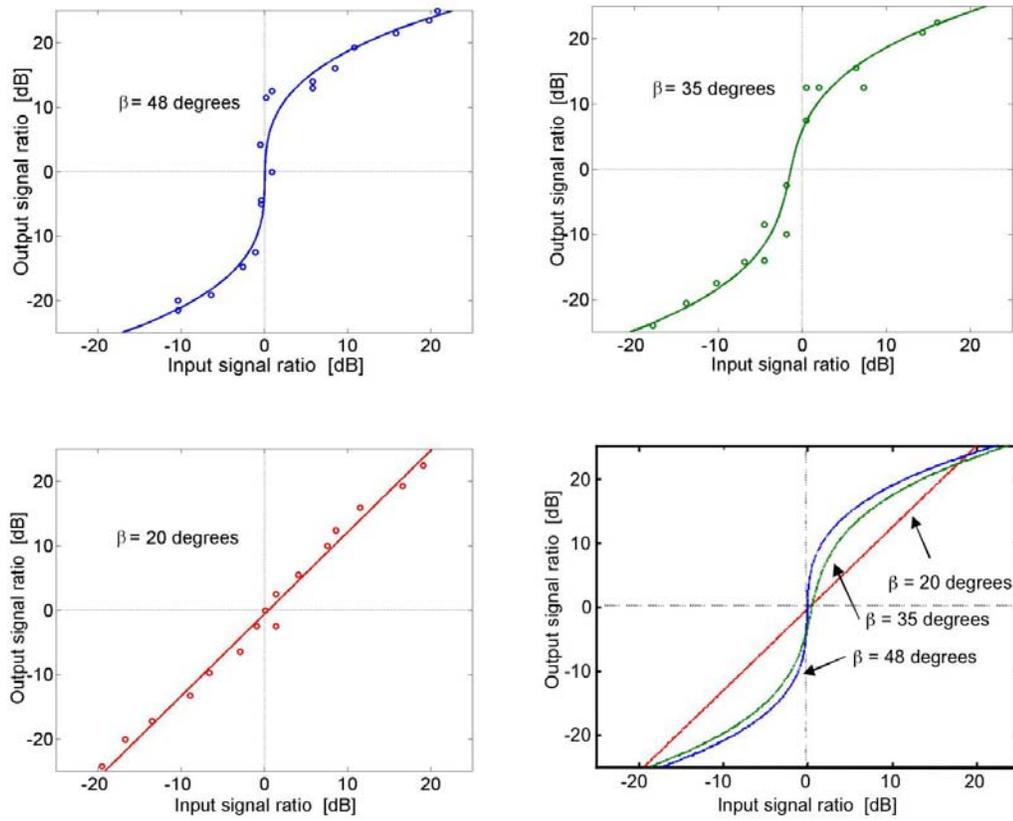
Figure 3.20. Signal extraction properties of the adaptive system parameterized by the mutual angle between the

transmitters.

Angle between transmitters (α) [degrees]	Receiver cross talk [dB]	Maximum slope enhancement (dB)
48	-15	76
35	-10	6.1
20	0	1.3

Table 1. Cross talk and enhancement slope of the antenna system for three different angles between the

transmitters in the far field.

indistinguishable from one. However, the analysis in terms of power omits the important role of the signal phase and this is the reason there is still some observed signal contrast enhancement, however small. Overall the performance of the system at separating out the two source signals degrades gracefully as our mixture of signals becomes less orthogonal.

3. 6   Remarks

The role of the antenna lens array in our system design is subtler than might first be apparent. It is true that the array performs something akin to a spatial Fourier transform on the signal space; roughly speaking, it converts an angle of arrival to a spatial region in the focal surface. In this sense it does some preprocessing of the incoming signals. If the incoming signals are known to have well-defined and distinguishable directions, the adaptive processor is less relevant. The focal-surface detectors already contain fairly well separated signals. That does not help in cases of multipath and other forms of interference. In principle it makes no difference to the auto-tuning filter whether or not this "Fourier" transformation of the signals takes place. The actual practical benefit of the antenna lens array enters through dynamic range considerations: in a typical communications scenario one can expect the power incident on the antenna lens array to be more or less uniform over the array, while the power at the focal surface varies by a larger amount. Consider two angularly well-separated sources for example, one giving rise to a received power of 1 W, and the second giving rise to a received power of 0.1 W. At the array, each antenna element receives the same power of 1.1/N watts, where N is the number of array elements. At the focal surface, one detector receives 1.0 W while the second receives 0.1 W. One can clearly amplify the signal from the second detector so that the output powers from the front-end channels are more similar for both signals. This could not be done were the signals taken directly at the antenna array. Such dynamic range considerations remain valid when the signals are subject to a multipath environment.

Our prototype demonstration is designed for processing two signals. Among the major benefits of the optical processing are its scaling characteristics. A larger input signal space, say of size N, can be accommodated merely by increasing the number of electrodes on the electrooptic modulator to N —the autotuning filter remains largely unchanged. Increasing

the number of output channels from 2 to M, requires a total of (M-1) autotuning filters. Thus in general the adaptive processor scales linearly with the size of the desired signal space, rather than quadratically, as is often the case with adaptive electronic processors.

Our system will optimally process multipath communication signals provided arrival time differences are negligible compared to the inverse bandwidth of the signal. Different paths are received by different focal surface receivers. The autotuning filter combines the received signals coherently while the noise from different receivers adds incoherently. When the multipath delay times are much greater than the inverse signal bandwidth, the autotuning filter treats each as a separate source and extracts the strongest one.

The prototype demonstrated here processes signals with bandwidths in the 100 MHz range. None of the components are however limited to this bandwidth. Broadband antennas, such as second resonant slots with up to 20% bandwidth can be used instead of the patches at a higher carrier frequency, allowing for several gigahertz IF frequencies. A possible issue in this case may be the angle-of-arrival detection quality due to higher grating lobes at the lower band edge, which is a design parameter. The electro-optic modulator presented here is effectively a lumped-element circuit, but its architecture accommodates a set of N coupled traveling wave transmission lines, and such an EO modulator can cover several gigahertz of bandwidth with good modulation efficiency.

CHAPTER 4

A PHOTOREFRACTIVE REGENERATIVE

AMPLIFIER

4. 1   Introduction

The autotuning filter of Chapter 2 extracts one principal component at a time. Extracting all the components requires cascading as many filters as there are signals at the input, minus one. The filter runs on a minimum of 3 mW of optical power supplied by the input signal-carrying beams. After the filter, the through beam is weaker since the ring extracts some of its energy and the gain crystal also absorbs nearly half of it. Current small laser sources—that easily fit in a briefcase for example—output up to a couple hundred milliwatts. This limits how many autotuning filters, or any other photorefractive circuit, may be daisy-chained before there is simply not enough optical power left to add a new one. Adding more laser sources is a complicated solution as our circuits rely on coherent beams: the added sources would have to be injection-locked. Amplification appears as a simpler solution in the long run.

This short chapter presents the first steps toward making photorefractive regenerative amplifiers. For the first amplifier, in hopefully a longer series, we chose to work on an amplifier that takes a multimode beam in and outputs a single mode beam with the same

temporal characteristics as the input beam. This amplifier could, for example, be added at the outputs of cascaded autotuning filters (the outputs that locally extract the largest principal component of their input space.) The same amplifier could not be inserted in between cascaded filters, as the spatial diversity needs to be preserved for the input of the following filter.

4. 2   A photorefrative amplifier

4. 2. 1   Design issues

We chose to use a photorefractive ring oscillator to convert a multimode beam into a single mode beam.   As mentioned in section 2. 2, a ring oscillator pumped with photorefractive two-beam coupling transfers all of the temporal features of the input to the oscillating beam. This is true weather both or either of the input and ring beams are single mode or multimode. In the case of a single mode cavity, the photorefractive gratings adapt so that the diffracted input signal is always on resonance with the length of the loop [64]. Some of the photorefractive gain is sacrificed to induce the necessary phase shift if the signal is off resonance.   In any case, this simple ring transforms a multimode beam into a single mode one. It does not overall provide gain: sampling the ring produces the output beam so the finite gain limits how much light can be taken out. To provide real gain we have two choices. One consists of adding a semiconductor laser amplifier in series with the single mode output beam. The second choice involves incorporating the semiconductor amplifier in the ring. It is a more elegant but also more complex solution. The challenge of inserting an amplifier in an adaptive resonator is that it will naturally tend to make the cavity lase at the frequency that yields the highest energy in the ring. This is due to the fact that the spontaneous emission of a semiconductor amplifier is equivalent to an optical broadband noise source. The design of a regenerative amplifier with a semiconductor laser diode in a photorefractive ring must therefore prevent the lasing and ensure that all the available gains serve to amplify a given signal.

We started our photorefractive amplifier experimental investigations with work necessary for both of the amplifier solutions mentioned above. We first learned how to pump a photorefractive ring resonator that was forced to be single mode.   This constraint was

achieved by obliging the oscillating beam to couple in and out of a single mode fiber inserted in the loop. Second, we learned how to make a semiconductor laser diode amplifier since they are not commercially available. The following section provides the technical details about how to make the device.

4. 2. 2 Manufacturing a semi-conductor laser amplifier in a research laboratory

4. 2. 2. 1   The method

Conceptually, a traveling wave optical amplifier is simple. It is a laser diode gain medium through which an optical beam passes once. The first step to making a semiconductor amplifier is the acquisition of a semiconductor laser diode chip. In this world of cheap red laser pointers, it is surprisingly difficult to get small quantities of bare laser diode chips. Eventually the company Semiconductor Laser International sold us some uncoated, double heterostructured InGaAlP diodes, initially designed to emit at 655nm. The second manufacturing step consists of attaching the chips to a mount that allows us to deliver 200 mA of current to the chip and that acts as a heatsink. The third step is anti-reflection coating both facets of the chips.

4. 2. 2. 2   The technique

Mounting the chips

We used one of the industry's standard diode laser submounts called c-mounts with some slight modification. Figure 4.1 shows the modified c-mount. The top part of the mount is thinned down to be roughly the same thickness as the diode chip's length (about 500 microns.) This is so the full 30-degree cone of acceptance of the chips stays unobstructed on both sides. Our chips are designed to be single spatial mode laser sources

which leads to a smaller, 1x3 µm-aperture than commercial multi-spatial modes power amplifiers which have 1x100 or 200 µm-apertures.

We glued the chips down on the mounts with very highly electrically and thermally conductive glue from Epoxy Technology (2 part epoxy, model # EPO-TEX H20E). We manipulate the chips with a Vaccum Parts Handling System from Techni-Tool. It is a pen-shaped tube, connected to a small vacuum pump on one end and fitted with a metal syringe tip on the other (plastic syringe tips turned out to pick up static electricity too well.). Miniature wood tweezers (carved out of a wood Q-tip stick) proved to be another useful tool to manipulate the chips. Once glued in place, the top metal sides of the chips are wedge-bonded to the ribbon-like electrode illustrated in Figure 4.1.
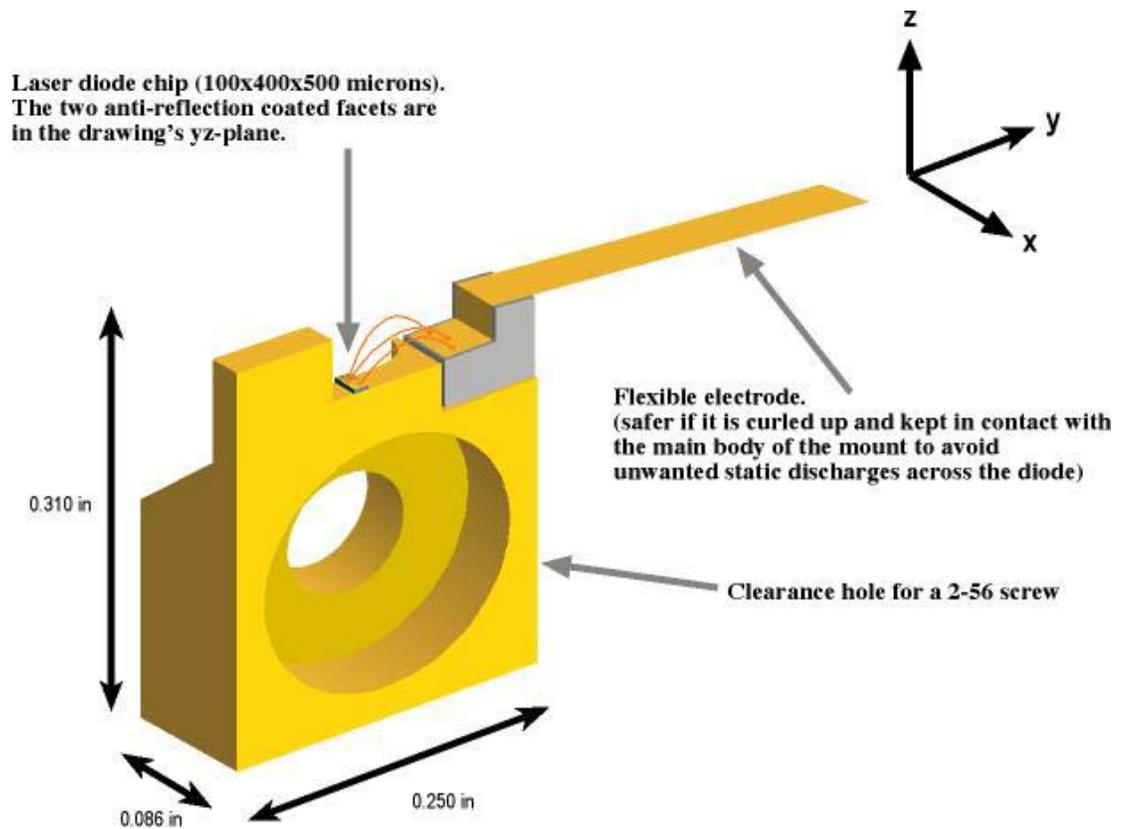
Figure 4.1 Schematic of the c-mount used to heatsink the semiconductor chip and also provide the electrodes
necessary to supply the chip with current.

Coating the chips

InGaAlP has an index of refraction of 3.5 so that the facets of the chip produce natural 30% reflecting mirrors. These offer a resonating cavity to the spontaneously emitted light, imposing a lasing current threshold on the semiconductor amplifier. In addition, the presence of a cavity induces ripples on the wavelength dependent gain-curve that distort the amplification of a broad bandwidth signal. The better the anti-reflection coating and the smaller those ripples. Optical amplifiers became commercially viable when the reflections of their input and output facets were reduced to less than 0.01%.

The diodes' coatings were optimized by monitoring the laser output power versus the injection current during the coating process. We chose to deposit a single quarter-wavelength layer of HfO_2 by electron-beam evaporation. The diode's output-power-versus-current (PI) curve was continuously observed during the process: the diode was subject to a periodic ramp of current that was displayed on an oscilloscope along with the optical beam's power. When the lasing current threshold was crossed, the slope of the PI curve exhibited a sudden change. As the coating approached the optimal thickness, the lasing disappeared altogether. We then closely observed the peak power of the spontaneous emission decrease. The deposition process was stopped when the decrease-rate slowed down, which was sign that the light emission was at a minimum and about to increase again. Figure 4.2 shows the PI curves of a diode measured before coating and then after each facet has been coated. Reflection curves taken with an optical spectrum analyzer and microscope revealed the center wavelength and bandwidth of the coatings. We achieved less than 0.01% reflection over tens of nanometers.
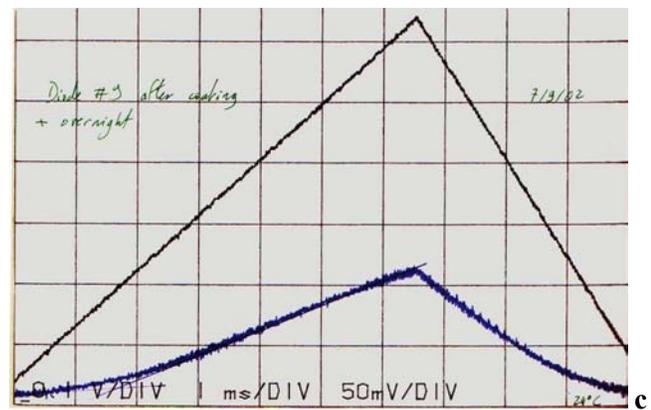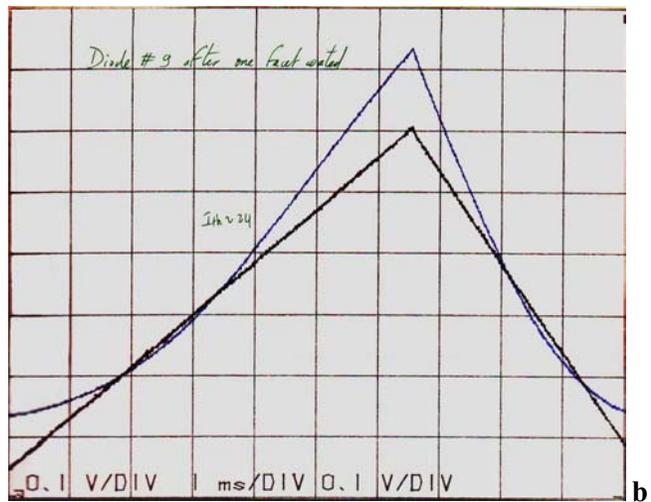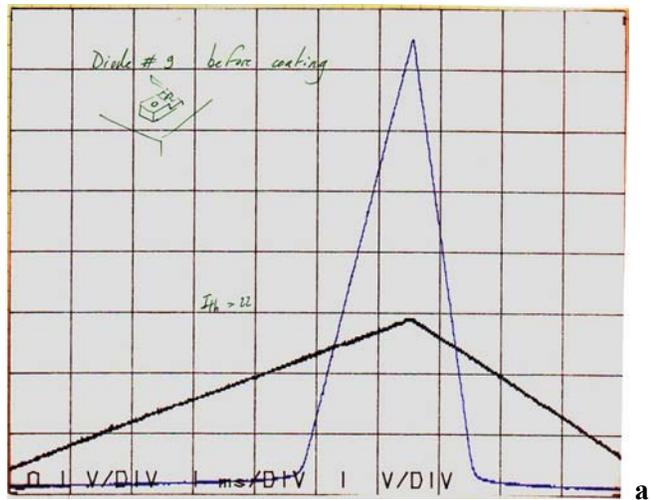
Figure 4.2. PI curves of a laser diode. The triangular black curves represent the current passing through the diode. Their vertical scale is 100 mV for 10 mA. The nonlinear blue curves represent the laser ouptut power monitored by a photodetector placed in the vacuum chamber, taken a) before coating,(Ith = 22 mA), b) after coating one facet (Ith=33 mA), and c) after coating both facets (lasing Ith not apparent below 65 mA).

The thickness of $Hf0_2$ deposited was monitored through the resonant frequency of a piezo-electric crystal being coated alongside the chips. Unfortunately our calibration of the thickness deposited was not repeatable enough. The center frequency of the anti-reflection coating changed (over 100 nm) with nearly every run. The yield of usable diodes was low so we sacrificed performance for speed: we sent our diodes to be coated in bulk to a coating company (Spectrum Thin Films, NY.) The diodes were packaged so that the c-mounts were attached to a single metal "window frame" (both sides of the diodes had to be open for coating) and each had its electrodes shorted. The diodes survived the trip and came back with a good uniform coating for 655 nm.

4. 2. 2. 3   Results

The uncoated diode chips purchased from SLI were originally intended to become 35 mW laser diodes with 80 mA of current. The anti-reflection coated diode chips, pumped with 100 mA of current, amplified a 0.2 mW, 655 nm beam up to 20 mW. This is an unsaturated gain of 20 dB.

4. 2. 3 Immediate future work

The immediate next step will consist of integrating the c-mounted diode in a pre-aligned lens-diode-lens unit. Figure 4.3 shows the proposed design for the mechanical alignment of the unit with 5 degrees of freedom (the unnecessary 6th is the rotation around the diode's waveguide axis). The pre-aligned unit could then be inserted into any circuit where a diode amplifier needs to be tried out.
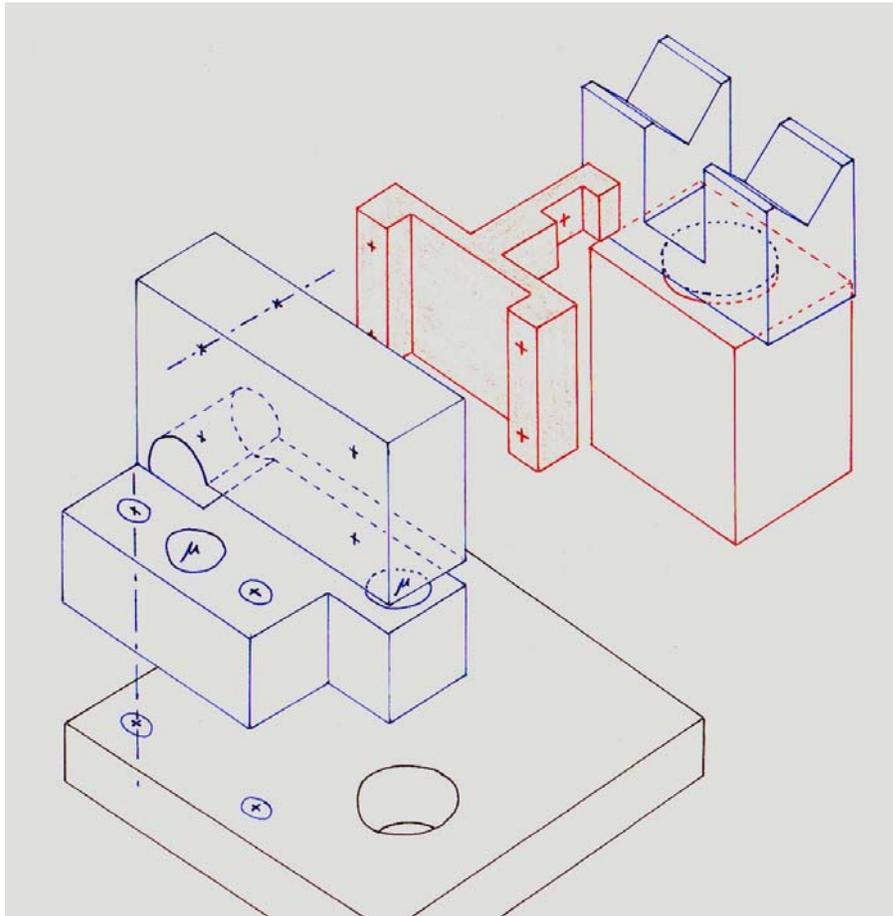
Figure 4.3. Proposed mechanical mount to align a lens, the diode amplifier and another lens.

CHAPTER 5

CONCLUSIONS

This thesis summarized the development of three projects. The first project concerned the building and the analysis of a photorefractive oscillator. We named it an autotuning filter for its ability to automatically tune in to the strongest principal component of its spatio-temporal input space. This filter was the object of Chapter 2. The following chapter described the insertion of that optical circuit in a sophisticated RF-photonics system, which implemented principal component extraction on mixtures of two microwave signals received by a 10 GHz quasi-optical lens antenna array. Finally, Chapter 4 presented the first development stages of an optical amplifier adapted to photorefractive information processing. All three projects achieved progress toward engineering photorefractive circuits for commercial applications.

The autotuning filter's ancestors are circuits such as the feature extractor and the frequency demultiplexer. Their experimental implementations occupied about half a standard optical table (about 2 m^2) and required hundreds of milliwatts to operate. The signals processed by those circuits were within audio frequency range. The free space optics version of the autotuning filter, described in Chapter 2, processes signals with up to 3 GHz of bandwidth. The circuit fits on a quartz plate that is 3 cm in diameter and requires only 3 mW of optical power to operate. The earlier, fiber versions of the autotuning filter required about 10 mW of optical power and could process signals with bandwidths of hundreds of MHz.

Their signal separation performance was not as good as the performance of the free space optics version of the filter but the results were very repeatable. This is not the case with the free space optics version whose performance varies greatly with the alignment of the input pump beams to the oscillator. A non-optimized alignment yields a slope at the origin of 8 dB/dB, which is as good as the fiberized versions of the filter. An optimized alignment yields a quasi bistable device for input signals with powers within 10% of each other. Future work on this device should include a way to make the alignment of the input beams repeatable so that the device's performance may also be uniform from one use to the next. One solution would be to fiberize the input with single mode fibers whose alignment can be optimized once and then fixed in place.

Chapter 3 demonstrated that the use of dynamic holographic optics in microwave systems could be implemented with reasonable robustness, power consumption and size, to be convenient in practical environments. The prototype system we presented performed principal component extraction on an ensemble of signals incident on a microwave antenna array. At the end of Chapter 3 we discussed widening the processing bandwidth of our system as well as increasing the number of signals it could handle. Another direction for future work lies in implementing a more powerful method for blind source separation (BSS.) Principal component analysis (PCA) separates signals by forming a set of uncorrelated spatio-temporal signals. The characterization section of Chapter 3 showed how the PCA method fails to recognize the original source signals when the received mixtures are not spatially orthogonal. There is a BSS method called independent component analysis (ICA) that does not require spatially orthogonal mixtures. ICA yields the original source signals if the temporal behaviors of the source signals are not correlated to any degree and that the received mixtures are linear combination of these signals. ICA may be implemented with optics and electronics in two stages. The first stage performs PCA on the received mixtures. The second stage consists of a winner-takes-all opto-electronic loop that extracts one of the

independent components from the principal components at its input. A prototype of such a system is currently being developed in our laboratories.

Finally, Chapter 4 presented the making of an optical semiconductor amplifier for red wavelengths. To render this device practical, the mounted chip must be incorporated in a unit that facilitates the handling and the coupling of light into and out of the amplifier. This convenient single mode amplifier unit could be inserted in a single mode ring pumped by a multi-mode beam. It was explained in Chapter 4 how that oscillator would transform a multi-mode beam carrying a temporal signal to a single mode beam carrying essentially the same information. Last and most difficult would be the realization of a fully spatially multi-mode amplifier.

In conclusion, this thesis described the miniaturization of a photorefractive oscillator capable of extracting the strongest principal component of its input signal space. The analysis and simulation of the circuit provided insight into the circuit's dynamics. This autotuning filter physically performs a task that is otherwise computationally intensive for such high bandwidth signals. Chapter 3 showed that the insertion of this photorefractive circuit in a microwave processor was reasonably practical and robust to transportation. The work on optical amplifiers adapted to our way of handling information opened the gate for designing more complex and smarter photorefractive circuits.

CHAPTER 6

REFERENCES

BIBLIOGRAPHY

1. Neff, J.A. *The role of optics in future computational systems*. in *Topical Meeting on Optical Computing*. 1985. Incline Village, NV.

2. Anderson, D.Z. and J. Feinberg, *Optical Novelty Filters.* Ieee Journal of Quantum Electronics, 1989. **25**(3): p. 635-647.

3. Anderson, D.Z. and M.C. Erie, *Resonator Memories and Optical Novelty Filters.* Optical Engineering, 1987. **26**(5): p. 434-444.

4. Gan, Z., L. Bintz, and D.Z. Anderson, *Fiberoptic Acoustic Fourier Transducer for Audio Sound Processing.* Applied Optics, 1992. **31**(11): p. 1740-1744.

5. Zhou, G., et al., *A Life-Sized Physical Model of the Human Cochlea with Optical Holographic Readout.* Journal of the Acoustical Society of America, 1993. **93**(3): p. 1516-1523.

6. Anderson, D.Z., et al., *Photorefractive Flip-Flop.* Optics Letters, 1991. **16**(4): p. 250-252.

7. Crouch, D.D. and D.Z. Anderson, *Dynamics of an Optical Ring Circuit Having Photorefractive Gain and Loss and History-Dependent Feedback.* Journal of the Optical Society of America B-Optical Physics, 1991. **8**(6): p. 1315-1325.

8. Montemezzani, G., G. Zhou, and D.Z. Anderson, *Self-Organized Learning of Purely Temporal Information in a Photorefractive Optical-Resonator.* Optics Letters, 1994. **19**(23): p. 2012-2014.

9. Saffman, M., et al., *Topology-Preserving Mappings in a Self-Imaging Photorefractively Pumped Ring-Resonator.* Chaos Solitons & Fractals, 1994. **4**(11): p. 2077-2092.

10. Saffman, M., C. Benkert, and D.Z. Anderson, *Self-Organizing Photorefractive Frequency Demultiplexer.* Optics Letters, 1991. **16**(24): p. 1993-1995.

11. Anderson, D.Z., et al., *Optical implementation of a self-organizing feature extractor.* Advances in Neural Information Processing Systems IV, 1992.

12. Anderson, D.Z., M. Saffman, and A. Hermanns, *Manipulating the Information Carried by an Optical Beam with Reflexive Photorefractive Beam Coupling.* Journal of the Optical Society of America B-Optical Physics, 1995. **12**(1): p. 117-123.

13. White, J.O. and A. Yariv, *Photorefractive Crystals as Optical-Devices, Elements, and Processors.* Proceedings of the Society of Photo-Optical Instrumentation Engineers, 1984. **464**: p. 7-20.

14. Kwong, S.K., et al., *Conversion of Optical-Path Length to Frequency by an Interferometer Using Photorefractive Oscillation.* Applied Physics Letters, 1985. **47**(5): p. 460-462.

15. Huignard, J.P. and P. Gunter, *Photorefractive Materials and Their Applications .2. Survey of Applications - Introduction.* Topics in Applied Physics, 1989. **62**: p. 1-3.

16. Dunning, G.J., Y. Owechko, and B.H. Soffer, *Hybrid Optoelectronic Neural Networks Using a Mutually Pumped Phase-Conjugate Mirror.* Optics Letters, 1991. **16**(12): p. 928-930.

17. Ja, Y.H., *A Double-Coupler Optical Fiber Ring-Loop Resonator with Degenerate 2-Wave Mixing.* Optics Communications, 1991. **81**(1-2): p. 113-122.

18. Frauel, Y., et al., *Topological map from a photorefractive self-organizing neural network.* Optics Communications, 1997. **135**(1-3): p. 179-188.

19. Petrovic, M.S., et al., *Optical photorefractive flip-flop oscillator.* Optics Communications, 1997. **138**(4-6): p. 349-353.

20. Schwab, M., et al., *Fourier control of pattern formation in an interferometric feedback configuration.* Optics Communications, 1999. **170**(1-3): p. 129-136.

21. Hung, K.M., *Optical pattern recognition using a unidirectional photorefractive oscillator coupled with an angular multiplexing volume hologram.* Journal of Modern Optics, 2000. **47**(4): p. 655-661.

22. Desfarges-Berthelemot, A., et al., *Intracavity beam shaping and referenceless holography.* Optical Materials, 2001. **18**(1): p. 27-35.

23. Sedlatschek, M., et al., *Demonstrator Concepts and Performance of a Photorefractive Optical Novelty Filter.* Optical Materials, 1995. **4**(2-3): p. 376-380.

24. Jolliffe, I.T., *Principal component analysis*. 2nd ed. Springer series in statistics. 2002: New York: Springer-Verlag. 487.

25. Saffman, M., *Self-organized formation of image representations in photorefractive oscillators*, in *Physics (JILA)*. 1994, University of Colorado: Boulder.

26. Damiao, V., *Developments in photorefractive two-beam coupling systems*, in *Electrical Engineering (JILA)*. 2000, University of Colorado: Boulder, CO.

27. Khukhtarev, N.V., *Holographic storage in electro-optic crystals. II. Beam coupling - Light amplification.* Ferroelectrics, 1979. **22**: p. 961-4.

28. Yeh, P., *Introduction to Photorefractive Nonlinear Optics*, ed. Wiley-Interscience. 1993, New York: John Wiley & Sons, Inc.

29. Solymar, L., D.J. Webb, and A. Grunnet-Jepsen, *The physics and applications of photorefractive materials*. Oxford series in optical and imaging sciences. 1996: New York : Oxford University Press.

30. Klein, M.B. and G.C. Valley, *Characteristics of BaTiO3 for electro-optic devices.* Proc. SPIE - Int. Soc. Opt. Eng., 1986. **1986b**(567): p. 116-20.

31. White, J.O., et al., *Coherent Oscillation by Self-Induced Gratings in the Photorefractive Crystal Batio3.* Applied Physics Letters, 1982. **40**(6): p. 450-452.

32. Jain, R.K. and G.J. Dunning, *Spatial and Temporal Properties of a Continuous-Wave Phase- Conjugate Resonator Based on the Photorefractive Crystal Batio3.* Optics Letters, 1982. **7**(9): p. 420-422.

33. Croningolomb, M. and A. Yariv, *Plane-Wave Theory of Nondegenerate Oscillation in the Linear Photorefractive Passive Phase-Conjugate Mirror.* Optics Letters, 1986. **11**(4): p. 242-244.

34. Kwong, S.K., M. Croningolomb, and A. Yariv, *Oscillation with Photorefractive Gain.* Ieee Journal of Quantum Electronics, 1986. **22**(8): p. 1508-1523.

35. Dai, L.K., et al., *Photorefractive Mode-Coupling between 2 Unidirectional Ring Oscillators.* Applied Physics B-Photophysics and Laser Chemistry, 1991. **53**(3): p. 153-159.

36. Dalessandro, G., *Spatiotemporal Dynamics of a Unidirectional Ring Oscillator with Photorefractive Gain.* Physical Review A, 1992. **46**(5): p. 2791-2802.

37. Dambly, L. and H. Zeghlache, *Theory of a Multimode Photorefractive Oscillator - Quantitative Results on the Frequency-Shift.* Physical Review A, 1994. **49**(5): p. 4043-4054.

38. Kaczmarek, M. and R.W. Eason, *Conditions for efficient build-up of power in photorefractive ring cavities.* Optics Communications, 1998. **154**(5-6): p. 334-338.

39. Sandfuchs, O., et al., *Spatio-temporal dynamics in photorefractive two-wave mixing configurations: the counterpropagating geometry and the unidirectional ring oscillator.* Chaos Solitons & Fractals, 1999. **10**(4-5): p. 709-724.

40. Montemezzani, G., et al., *Origin of the Lobe Structure in Photorefractive Beam Fanning.* Physical Review A, 1995. **52**(2): p. 1791-1794.

41. Rothe, H., O. Ginter, and C. Woldenga, *Assessment and Robust Reconstruction of Laser-Radar Signals.* Optics and Laser Technology, 1993. **25**(5): p. 289-297.

42. Kim, K.T., D.K. Seo, and H.T. Kim, *Efficient radar target recognition using the MUSIC algorithm and invariant features.* Ieee Transactions on Antennas and Propagation, 2002. **50**(3): p. 325-337.

43. Zhang, Y.W. and Y.L. Ma, *CGHA for principal component extraction in the complex domain.* Ieee Transactions on Neural Networks, 1997. **8**(5): p. 1031-1036.

44. Du, K.L., et al., *Neural methods for antenna array signal processing: A review.* Signal Processing, 2002. **82**(4): p. 547-561.

45. Kung, S.Y., K.I. Diamantaras, and J.S. Taur, *Adaptive Principal Component Extraction (Apex) and Applications.* Ieee Transactions on Signal Processing, 1994. **42**(5): p. 1202-1217.

46. Becker, S. and M. Plumbley, *Unsupervised neural network learning procedures for feature extraction and classification.* Applied Intelligence, 1996. **6**(3): p. 185-203.

47. Jang, J.S. and D.H. Shin, *Parallel optical-feature extraction by use of rotationally multiplexed holograms.* Optics Letters, 1996. **21**(19): p. 1612-1614.

48. Zhang, H., et al., *Image feature extraction with various wavelet functions in a photorefractive joint transform correlator.* Optics Communications, 2000. **185**(4-6): p. 277-284.

49. Sheng, Y.L. and C. Lejeune, *Invariant Pattern-Recognition Using Fourier-Mellin Transforms and Neural Networks.* Journal of Optics-Nouvelle Revue D Optique, 1991. **22**(5): p. 223-228.

50. Gindi, G.R. and A.F. Gmitro, *Optical-Feature Extraction Via the Radon-Transform.* Optical Engineering, 1984. **23**(5): p. 499-506.

51. Qu, J.A., H.P. Chang, and S.M. Xiong, *Optical processing of light-induced autofluorescence for characterization of tissue pathology.* Optics Letters, 2001. **26**(16): p. 1268-1270.

52. Bacci, M., et al., *Non-invasive fibre optic Fourier transform-infrared reflectance spectroscopy on painted layers - Identification of materials by means of principal component analysis and Mahalanobis distance.* Analytica Chimica Acta, 2001. **446**(1-2): p. 15-21.

53. Freitag, H., T. Huth-Fehre, and K. Cammann, *Rapid identification of plastics from electronic devices with NIR-spectroscopy.* Analytical Letters, 2000. **33**(7): p. 1425-1431.

54. Bjorsvik, H.R., *Reaction monitoring in explorative organic synthesis using fiber-optical NIR spectroscopy and principal component analysis.* Applied Spectroscopy, 1996. **50**(12): p. 1541-1544.

55. Okamoto, G.T., *Smart Antenna Systems and Wireless LANS*, ed. Kluwer. 1999: Norwell.

56. Meridith, S. and A. Crowley, *Smart system antennas.* Mobile Radio Technology, 1997.

57. Widrow, B. and S. Stearns, *Adaptive signal processing*, ed. P. Hall. 1985.

58. Haykin, S., *Unsupervised Adaptive Filtering, Volume 1: Blind Source Separation*, ed. Wiley-Interscience. Vol. 1. 2000. 460.

59. Cardoso, J.F. *On the performance of orthogonal source separation algorithms*. in *EUSIPCO*. 1994. Edimburgh, Scotland.

60. McGrath, D.T., *Planar 3-Dimensional Constrained Lenses.* Ieee Transactions on Antennas and Propagation, 1986. **34**(1): p. 46-50.

61. Ishio, H. and S. Shimada, *Optical amplifiers and their applications*. 1994, New York: New York : Wiley.

62. Zozulya, A.A., M. Saffman, and D.Z. Anderson, *Stability Analysis of 2 Photorefractive Ring-Resonator Circuits - the Flip-Flop and the Feature Extractor.* Journal of the Optical Society of America B-Optical Physics, 1995. **12**(6): p. 1036-1047.

63. Comon, P., *Independent Component Analysis, a New Concept.* Signal Processing, 1994. **36**(3): p. 287-314.

64. Yeh, P., *Theory of Unidirectional Photorefractive Resonators.* J. Opt. Soc. Am. B, 1985. **2**: p. 1924-8.

65. Hyvärinen, A. and J. Karhunen, *Independent component analysis*. 2001: Wiley-Interscience. 504.

66. Roland, C. and J. Palicot. *A blind recognition of the transmitted signal for a self-adaptive re-configurable terminal*. in *Proc. IST Mobile Communication Summit*. 2001. Barcelona, Spain.

67. Hollung, S., A.E. Cox, and Z.B. Popovic, *A bi-directional quasi-optical lens amplifier.* Ieee Transactions on Microwave Theory and Techniques, 1997. **45**(12): p. 2352-2357.

68. Popovic, Z. and A. Mortazawi, *Quasi-optical transmit/receive front ends.* Ieee Transactions on Microwave Theory and Techniques, 1998. **46**(11): p. 1964-1975.

69. Anderson, D.Z., et al., *-70 dB optical carrier suppression by two-beam coupling in photorefractive media.* Journal of Applied Physics, 2000 (?). **invited**: p. 743-748.

CHAPTER 7

APPENDICES

These appendices regroup technical information relative to the work presented in the previous chapters. The first appendix reveals the manufacturing process of photorefractive spherical crystals with tools commonly available in an experimental laboratory. The second appendix details the mechanical mounts that were designed for the autotuning filter versions using slabs of spherical crystals. The third appendix is transcript of the code to the Mathematica program written to study the influence of the filter's parameters on its signal separation performance. The fourth appendix details the mount that was designed to house the fragile electro-optic crystal and the electronic circuit that impedance matches the electrodes to 50 ohms. The fifth appendix presents a mechanical method to avoid vibration modes in a large piece of metal, the suitcase's optics base plate in our case. The sixth appendix describes the procedure for demonstrating the suitcase's signal separation abilities in front of an audience.

7. 1   Making spherical crystals
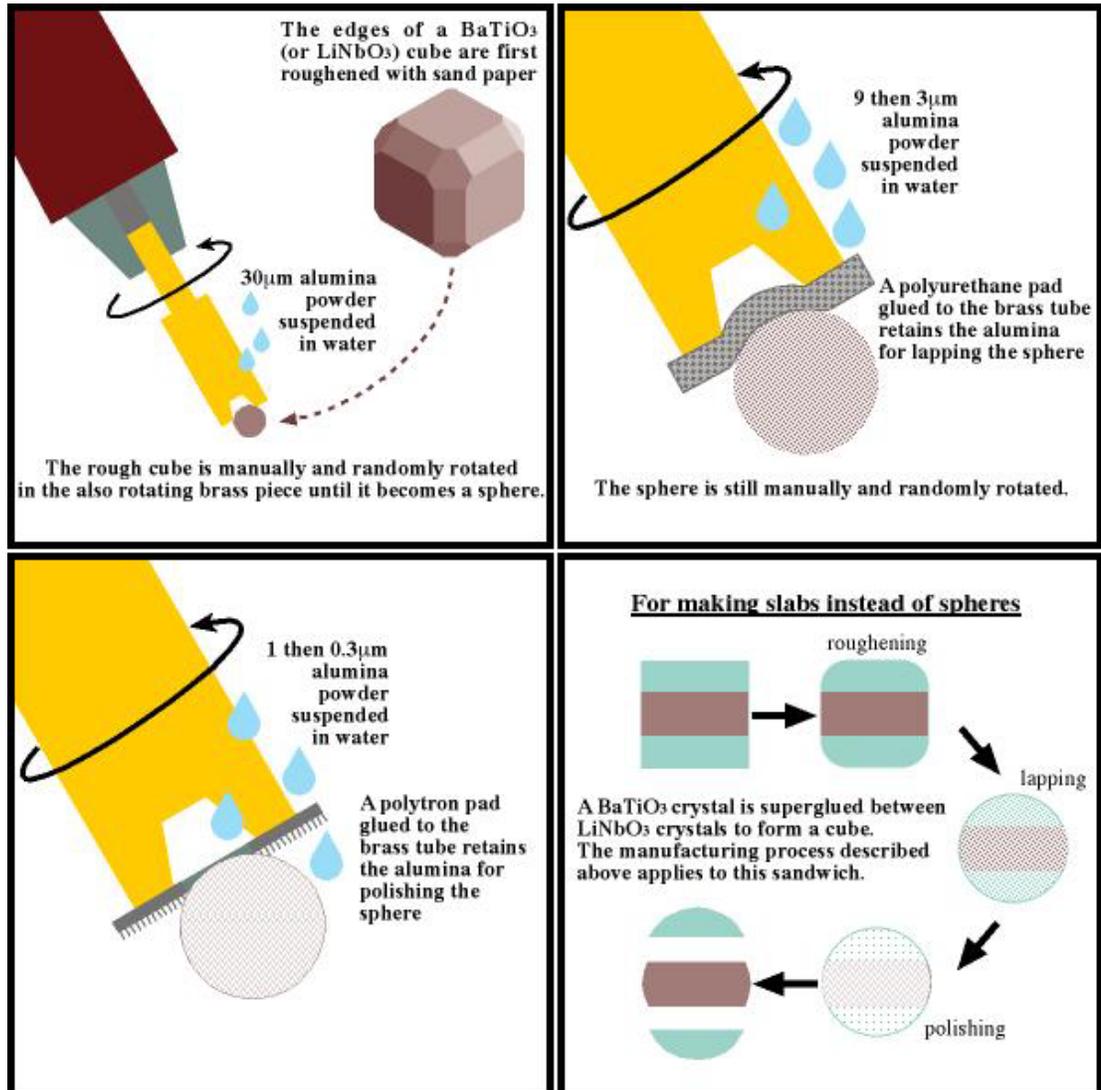
Figure 7.1 Description of the method to hand-make spherical photorefractive crystals.

7. 2   Mechanical mounts for the fiber filter

7. 2. 1   Ballbearings and glue

V-grooves constrain the fibers
in all directions but one

45 mm

BaTiO₃

The ballbearings provide a mechanical support
for the glue that holds the post in place.
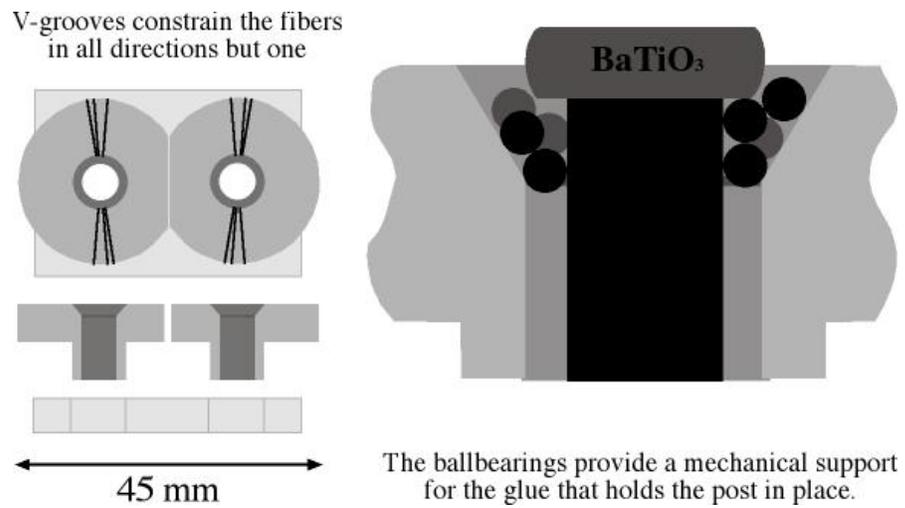
Figure 7.2 Mechanical mount for the first version of the autotuning filter with spherical photorefractive crystals

(see Figure 2.6.a.)

7. 2. 2   Pure mechanics

Figure 7.3 Mechanical mount for the second version of the autotuning filter with spherical photorefractive

crystals (see Figure 2.6.b.)

7. 3   Algorithm for studying the parameters' influence

Following is the Mathematica code that numerically simulates the autotuning filter.

Comments were added throughout the program to enable the reader to follow its structure.

```
Begin["study`"]
Off[General::spell1]
<< Graphics`

study`

ClearAll["study`*"]
```

Solutions to the space coupled differential equations

EqDiffr is the solution for the signal beam (field).
EqDiffp is the solution for the pump beam (field).
xr and xp are the positions of the initial conditions, and a and b are their values respectively.
g is the traditional gain ΓL.
x is the spatial coordinate at which the solution is wanted.

```
EqDiffr[xr_, a_, xp_, b_, g_, x_] := Sec[g (xp - xr)] * Sin[g x] * (b Cos[g xr] + a Sin[g xp]) +
  Cos[g x] * Sec[g (xp - xr)] * (a Cos[g xp] - b Sin[g xr]);
EqDiffp[xr_, a_, xp_, b_, g_, x_] := Cos[g x] * Sec[g (xp - xr)] * (b Cos[g xr] + a Sin[g xp]) -
  Sec[g (xp - xr)] * Sin[g x] * (a Cos[g xp] - b Sin[g xr]);

Equalize[a_, B_] := For[k = 1, k < n + 2, k++, {a[k] = B[[k]]}];
```

" Update grating" and " Propagate beams" modules

The "UpDate grating" module takes a linear array of pump (Plin), signal (Slin), and grating (Glin) values in.
c is the effective coupling constant: ΓL times the relative intensity ratio.
The "UpDate grating" module returns a linear array G with the new values of the grating at different positions.
The "Propagate beams" module returns two linear arrays S and P for the signal and pump values throughout the crystal.

```
UpDate[Plin_, Slin_, Glin_, c_] := Module[{Gnew, Gold, NewGrat, s, p, sp, pp, k},
  K1[Gold_, s_, p_, k_] := (-Gold + k / 2 * (s*p)) * Δt;
  K2[Gold_, s_, p_, sp_, pp_, k_] := (-Gold - K1[Gold, s, p, k] + k / 2 * (sp*pp)) * Δt;
  Gnew[Gold_, s_, p_, sp_, pp_, k_] :=
   Gold + 0.5 * (K1[Gold, s, p, k] + K2[Gold, s, p, sp, pp, k]);
  Clear[G];
  NewGrat := Array[ng, n];
  k := c;
  For[j = 1, j < n + 1, j++, {
    Gold = Glin[[j]];
    s = Slin[[j]];
    p = Plin[[j]];
    sp = EqDiffr[(j - 1) / n, s, (j - 1) / n, p, Gold + K1[Gold, s, p, k], j / n];
    pp = EqDiffp[(j - 1) / n, s, (j - 1) / n, p, Gold + K1[Gold, s, p, k], j / n];
    ng[j] = Gnew[Gold, s, p, sp, pp, k];}];
  G = NewGrat;
  ]
```

```
Propagate[Plin_, Slin_, Glin_] :=
Module[{NewS, NewP, ro, po},
  Clear[S, P];
  NewS := Array[ns, n + 1];
  NewP := Array[np, n + 1];
  ns[1] = Slin[[1]];
  np[1] = Plin[[1]];
  For[j = 2, j < n + 2, j++, {
    g = Glin[[j - 1]];
    ro = ns[j - 1];
    po = np[j - 1];
    ns[j] = EqDiffr[(j - 2)/n, ro, (j - 2)/n, po, g, (j - 1)/n];
    np[j] = EqDiffp[(j - 2)/n, ro, (j - 2)/n, po, g, (j - 1)/n];
    }];
  S = NewS;
  P = NewP;]
```

Constants

```
n = 10;        (* #of space steps, or crystal slices *)
Δt = 0.05;     (* time step for the Runga-Kutta integration *)
T = 300;       (* #of time steps *)
θ = Sqrt[.5];
m = 50;
Γl = 10;
```

Initializing functions

The indices g and r relate to the gain and reflexive crystals of the autotuning filter.
The indices 1 and 2 relate to the input signals.

```
po1 = Sqrt[1.1]; (* pump 1 field amplitude value *)
po2 = Sqrt[1];   (* pump 2 field amplitude value *)

Clear[Gg1, Gg2, Gr1, Gr2, Sg1, Sg2, Sr1, Sr2, Pr1, Pr2]

Gg1 := Array[gg1, n]; Sg1 := Array[sg1, n + 1]; Pg1 := Array[pg1, n + 1];
Gg2 := Array[gg2, n]; Sg2 := Array[sg2, n + 1]; Pg2 := Array[pg2, n + 1];
Gr1 := Array[gr1, n]; Sr1 := Array[sr1, n + 1]; Pr1 := Array[pr1, n + 1];
Gr2 := Array[gr2, n]; Sr2 := Array[sr2, n + 1]; Pr2 := Array[pr2, n + 1];
G := Array[g, n];
S := Array[s, n + 1]; P := Array[p, n + 1];

InitG[go_] := For[j = 1, j < n + 1, j++, {
    gg1[j] = go;
    gg2[j] = go;
    gr1[j] = go;
    gr2[j] = go;
    }];

InitSP[so1_, so2_] := For[j = 1, j < n + 2, j++, {
    sg1[j] = so1; pg1[j] = po1;
    sg2[j] = so2; pg2[j] = po2;
    sr1[j] = so1 * Sqrt[1/(1 + m)]; pr1[j] = so1 * Sqrt[m/(1 + m)];
    sr2[j] = so2 * Sqrt[1/(1 + m)]; pr2[j] = so2 * Sqrt[m/(1 + m)];
    }];
```

119

Algorithm for the time loop:
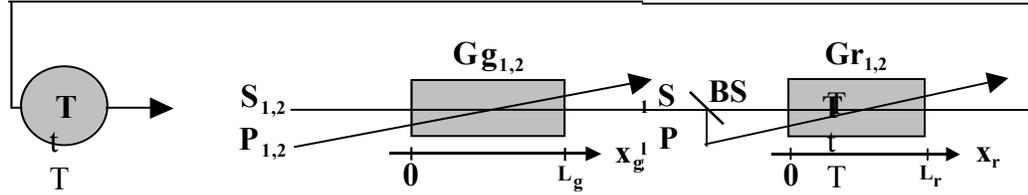
❑ Update the 2 gratings **Gg_i** in the gain crystal with the previous loop's intensities.

❑ Initialize the intensities of the beams just before the gain crystal:

Signal beams @ x_g = 0 = **T** x beams @ x_r= **L_r**

❑ Propagate the beams through the gain crystal.

❑ Update the 2 gratings **Gg_r** in the reflexive crystal with the previous loop's intensities.

❑ Initialize the intensities of the beams just before the gain crystal.

Signal beams @ x_r = 0 = **BS ratio** x beams @ x_g= **L_g**

❑ Propagate the beams through the reflexive crystal.

Time loop for a 2 feature reflexive ring (i.e., the autotuning filter)

This function uses the 2nd order Runga-Kutta method to integrate the time dependent photorefractive gain equation. It returns the description of the field amplitudes and the values of the gratings throughout the two PR crystals, after T temporal iterations.

Remarks:

1. The filter's model constrains the temporal signals to oscillate on separate spatial modes in the loop. This simplifies the grating equations: each grating then only depends on one temporal signal instead of both (there is only a weak dependence via the diminished coupling constant).

2. This integration does not let the light in the loop adjust in between rounds of updating the gratings. We believe it would not result in appreciable changes.

```
TimeLoop := For[i = 1, i < T, i ++, {
    cg1 = Tl /(po1^2+ sg1[1]^2+ po2^2+ sg2[1]^2);
    Update[Pg1, Sg1, Gg1, cg1]; Gg1 = G;
    cg2 := Tl /(po1^2 + sg1[1]^2+ po2^2+ sg2[1]^2);
    Update[Pg2, Sg2, Gg2, cg2]; Gg2 = G;
    sg1[1] = θ* sr1[n + 1]; sg2[1] = θ* sr2[n + 1];
    Propagate[Pg1, Sg1, Gg1]; Equalize[pg1, P]; Equalize[sg1, S];
    Propagate[Pg2, Sg2, Gg2]; Equalize[pg2, P]; Equalize[sg2, S];

    cr1 := Tl /(pr1[1]^2+ sr1[1]^2+ pr2[1]^2+ sr2[1]^2);
    Update[Pr1, Sr1, Gr1, cr1]; Gr1 = G;
    cr2 := Tl /(pr1[1]^2+ sr1[1]^2+ pr2[1]^2+ sr2[1]^2);
    Update[Pr2, Sr2, Gr2, cr2]; Gr2 = G;
    sr1[1] = Sqrt[1/(1+m)]* sg1[n+1]; sr2[1] = Sqrt[1/(1+m)]* sg2[n+ 1];
    pr1[1] = Sqrt[m/(1+m)]* sg1[n+1]; pr2[1] = Sqrt[m/(1+m)]* sg2[n+1];
    Propagate[Pr1, Sr1, Gr1]; Equalize[pr1, P]; Equalize[sr1, S];
    Propagate[Pr2, Sr2, Gr2]; Equalize[pr2, P]; Equalize[sr2, S];
    }]


InitG[0]
InitSP[Sqrt[.3], Sqrt[.4]]
TimeLoop
```

RESULTS---

```
sg1[1]^2
sg2[1]^2

0.947513

0.227704

MultipleListPlot[Pg1^2, Sg1^2, Pg2^2, Sg2^2, PlotRange → Automatic,
 AxesLabel →{"space steps", Intensity}, PlotJoined →True]
```
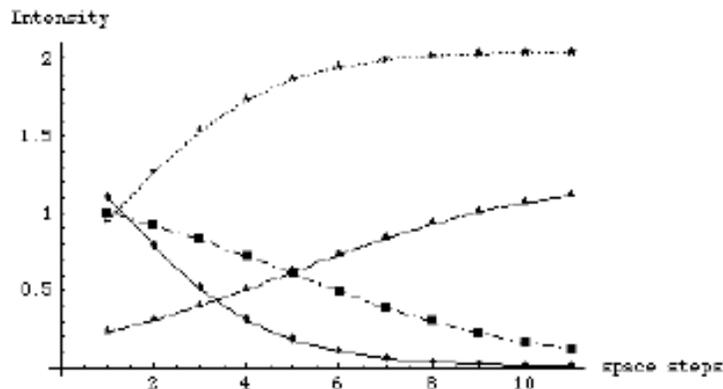


```
- Graphics -

IniG[go_] := For[j = 1, j < n + 1, j++, {
     Gg1[[j]] = go;
     Gg2[[j]] = go;
     Gr1[[j]] = go;
     Gr2[[j]] = go;
     }];
Result := Array[res, {10, 10}];
For[h = 1, h < 2, h++, {For[l = 1, l < 2, l++, {
       o1 = Sqrt[h * 0.1];
       o2 = Sqrt[l * 0.1];
       IniG[0];
       InitSP[o1, o2];
       TimeLoop;
       res[h, l] = sg1[1]^2;
      }; }];
MatrixForm[Result]
```

Results for pump ratio 1.1/1: lines correspond to equal So1, and columns equal So2, starting at 0.1 in increments of 0.1 (400 time loops for each value)

```
(10 by 10 matrix)
```

121

Feeding in a steady state solution

```
s1 = Sqrt[1.03591]; s2 = Sqrt[.07594];
Itot = s1^2 + po1^2 + s2^2 + po2^2;
Is[z_, Iso_, Ipo_] := Iso*(1 + Ipo/Iso)/(1 + Ipo/Iso*Exp[-Гl*z*(Iso + Ipo)/Itot]);
Ip[z_, Iso_, Ipo_] := Ipo*(1 + Iso/Ipo)/(1 + Iso/Ipo*Exp[+Гl*z*(Iso + Ipo)/Itot]);
Grate[z_, Iso_, Ipo_] := Гl/2*(Sqrt[Is[z, Iso, Ipo]]*Sqrt[Ip[z, Iso, Ipo]])/Itot;

For[j = 1, j < n + 1, j++, {
    gg1[j] = Grate[(j - 1)/n, s1^2, po1^2];
    gg2[j] = Grate[(j - 1)/n, s2^2, po2^2];
    gr1[j] =
      Grate[(j - 1)/n, Is[1, s1^2, po1^2]/(m + 1), Is[1, s1^2, po1^2]*m/(m + 1)];
    gr2[j] = Grate[(j - 1)/n, Is[1, s2^2, po2^2]/(m + 1), Is[1, s2^2, po2^2]*m/(m + 1)];
   }];

For[j = 1, j < n + 2, j++, {
   sg1[j] = s1; pg1[j] = po1;
   sg2[j] = s2; pg2[j] = po2;
   sr1[j] = Is[1, s1^2, po1^2]*Sqrt[1/(1 + m)];
   pr1[j] = Is[1, s1^2, po1^2]*Sqrt[m/(1 + m)];
   sr2[j] = Is[1, s2^2, po2^2]*Sqrt[1/(1 + m)];
   pr2[j] = Is[1, s2^2, po2^2]*Sqrt[m/(1 + m)];
   }]

TimeLoop
sg1[1]^2
sg2[1]^2

1.03591

0.07594
```

When fed the "middle" steady-state solution (see below) the system stays there :)
When fed the "extreme" left SS solution it evolves to s2 on, s1 off
When fed the "extreme" right SS solution it evolves to s1 on, s2 off

Steady state formulas **********************************

```
T = .5;   (* Intensity transmission of the loop *)
gg = 10;  (* ГL in the gain crystal *)
gr = 10;  (* ГL in the gain crystal *)
m = 50 ;  (* reflexive coupling's beam splitting ratio*)
```

Expressions for the steady-state gains in a reflexive ring:

```
G1[s1_, p1_, s2_, p2_] := .5*(s1 + p1)
/((p1*Exp[-gg*(s1 + p1)/(s1 + p1 + s2 + p2)] + s1)*
    (1 + m*Exp[-gr
          /(1 + ((p2 + s2) s2 (p1*Exp[-gg*(s1 + p1)/(s1 + p1 + s2 + p2)] + s1))/
              ((p1 + s1) s1 (p2*Exp[-gg*(s2 + p2)/(s1 + p1 + s2 + p2)] + s2)))])]);
G2[s1_, p1_, s2_, p2_] := 0.5*(s2 + p2)
/((p2*Exp[-gg*(s2 + p2)/(s1 + p1 + s2 + p2)] + s2)*
    (1 + m*Exp[-gr
          /(1 + ((p1 + s1) s1 (p2*Exp[-gg*(s2 + p2)/(s1 + p1 + s2 + p2)] + s2))/
              ((p2 + s2) s2 (p1*Exp[-gg*(s1 + p1)/(s1 + p1 + s2 + p2)] + s1)))])]);
```

Plot3D[G1[s1, po1^2, s2, po2^2], {s1, 0.001, 1.3}, {s2, 0.001, 1.3},
 AxesLabel→{s1, s2, gain1}, PlotPoints→30, PlotRange→{.9, 1}, BoxRatios→{2, 2, .5}]
Plot3D[G2[s1, po1^2, s2, po2^2], {s1, 0.001, 1.3}, {s2, 0.001, 1.3},
 AxesLabel→{s1, s2, gain2}, PlotPoints→30, PlotRange→{.9, 1}, BoxRatios→{2, 2, .5}]
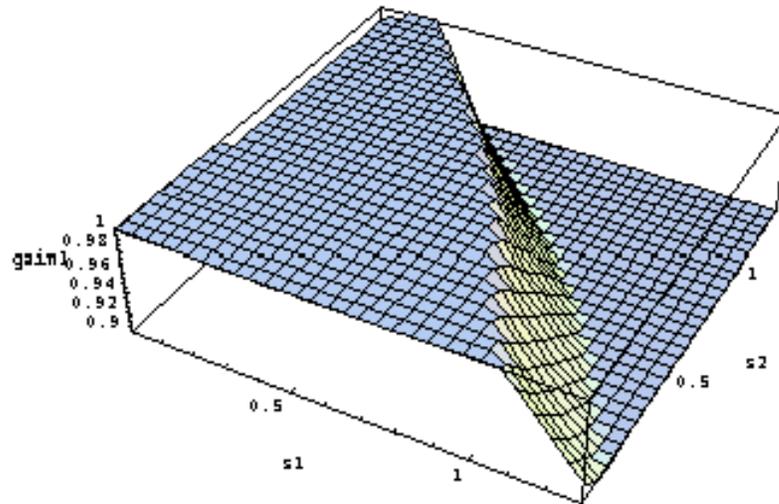
- SurfaceGraphics-
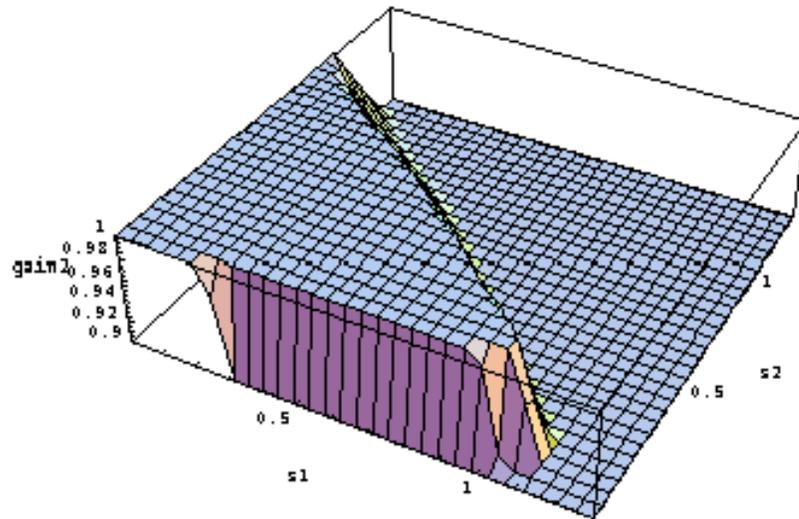
Sampling the Gain=1 curves to make a 2D plot list

```
GU1 := Array[g1, {53, 2}];
For[i = 0, i < 53, i++, {
    g1[i + 1, 1] = (0.01 + i * 0.02);
    g1[i + 1, 2] = s2 /. FindRoot[G1[g1[i + 1, 1], po1^2, s2, po2^2] == 1, {s2, 1}]}];

GU2 := Array[g2, {52, 2}];
For[i = 0, i < 52, i++, {
    g2[i + 1, 1] = (0.01 + i * 0.02);
    g2[i + 1, 2] = s2 /. FindRoot[G2[g2[i + 1, 1], po1^2, s2, po2^2] == 1, {s2, 1}]}];

GUL2 := Array[gl2, {15, 2}];
For[i = 0, i < 15, i++, {
    gl2[i + 1, 1] = (0.75 + i * 0.02);
    gl2[i + 1, 2] = s2 /. FindRoot[G2[gl2[i + 1, 1], po1^2, s2, po2^2] == 1, {s2, .01}]}];

Y := Partition[Flatten[{GU1, GUL2, GU2}], 2]
ListPlot[Y, Frame -> True, FrameLabel -> {"s1", "s2"}]
```
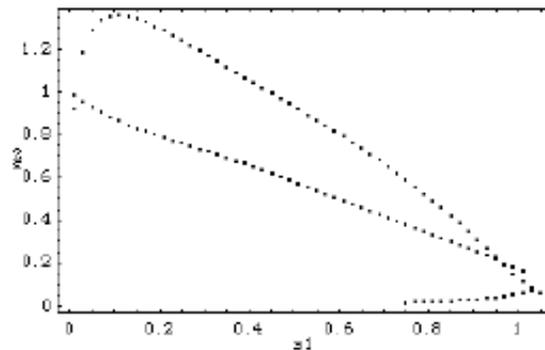


```
- Graphics -
```

Numerically finding the curves intersections

```
FindRoot[{G1[v1, po1^2, v2, po2^2] == G2[v1, po1^2, v2, po2^2],
    G1[v1, po1^2, v2, po2^2] == 1}, {v1, .001}, {v2, 1}]
FindRoot[{G1[v1, po1^2, v2, po2^2] == G2[v1, po1^2, v2, po2^2],
    G1[v1, po1^2, v2, po2^2] == 1}, {v1, .8}, {v2, .2}]
FindRoot[{G1[v1, po1^2, v2, po2^2] == G2[v1, po1^2, v2, po2^2],
    G1[v1, po1^2, v2, po2^2] == 1}, {v1, 1}, {v2, .1}]
FindRoot[{G1[v1, po1^2, 0, po2^2] == 1}, {v1, 1}]
FindRoot[{G2[0, po1^2, v2, po2^2] == 1}, {v2, 1}]
```

extreme left intersection

```
{v1 -> 0.0125476, v2 -> 0.978224}
```

middle intersection

```
{v1 -> 0.96033, v2 -> 0.206124}
```

extreme right intersection

```
{v1 -> 1.03591, v2 -> 0.0759455}
```

S1 on, S2 off

```
{v1 -> 1.09274}
```

S2 on, S1 off

```
{v2 -> 0.992304}
```

```
End[]
```

```
study`
```

124

7. 4   EO mount

The thin (0.3 mm) Mg:LiNbO$_3$ electro-optic crystal is sandwiched between a piece of grounded copper that was lapped flat and a piece of foam. A spring-loaded piece of metal pushes on the foam and holds the crystal in place. The copper electrodes (etched out from a copper covered plastic sheet) are inserted between the crystal and the piece of foam (plastic away from the crystal.)

The square-inch, resonant, matching circuit screws in sideways with its ground plane flat against the square wall visible in the center of the mount.
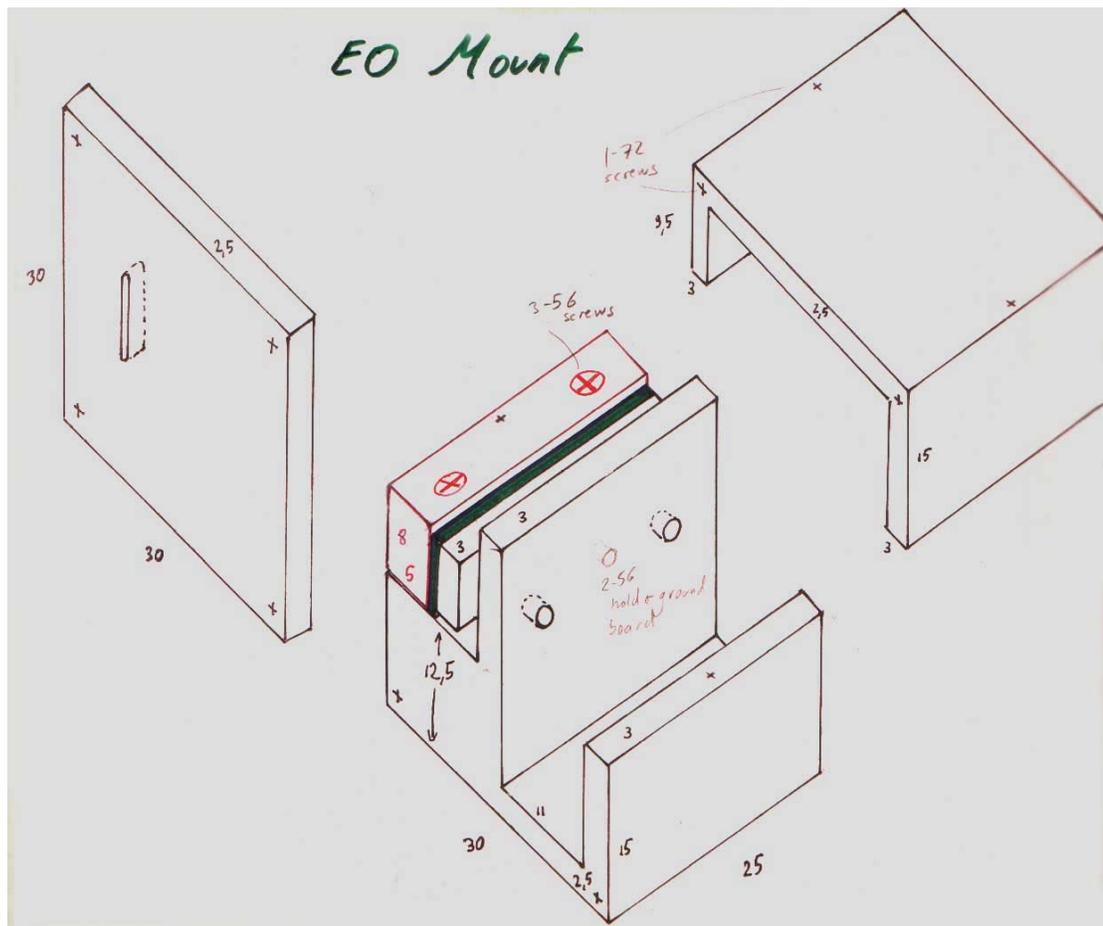
Figure 7.4. EO mount that holds the 0.3x7x30 mm crystal pressed against a piece of foam.

7. 5   Optics baseplate

The optics base plate is made out of a 3/4 inch thick piece of aluminum. To cut out vibration modes of the plate, 1/2 inch deep patterns were carved out of the bottom. These patterns are shown as striped patterns in the figure below. The light bulb shapes indicate the locations of the upside down table clamps.
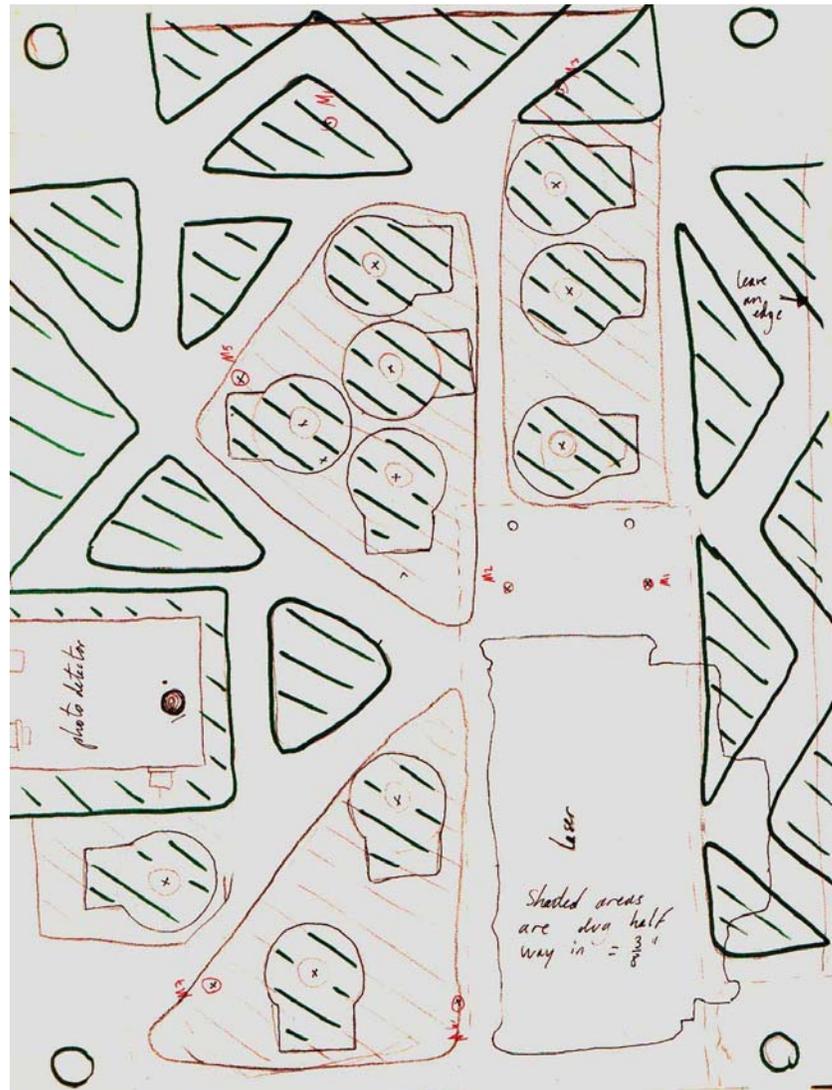

Figure 7.5. Hand drawing of the 1/2 inch deep patterns that were carved out of the bottom of the optics' baseplate.

The light bulb shapes indicate the positions of the upside down clamps that were shown in Figure 3.15.

126

7. 6   Suitcase manual

PART LIST

The suitcase
- Suitcase + power cord (white)

- 10dB directional coupler with BNC to SMA adapters

- 2 BNC cables (one labeled CH2 and the other labeled PD)

- TOOLS: Allen key (to fit fixing down srews)

- Flat-head screwdriver

- Wrench (SMA connector size)

The transmitters
- 2 transmitter boxes with their respective horn antennas

- AA and NiMH 6V batteries (or 2 PC power supplies and an extension cord)

- TOOLS: cross and flat-head screwdrivers, voltmeter

Handheld spectrum analyzer (Bantam)
To get the backlit display, press the contrast button and select backlight option ON then

the PRIOR MENU button to return to the normal screen.

To get a preset screen environment (=freq. range and ref. level) press the SAVE/RCL

button and then the SETUP MEM option. Select the desired setup by highlighting it and

then press the option RECALL.

When fully charged, the spectrum analyzer has a two-hour autonomy.

Receiving antennas

- Lens antenna

- 2 detecting patch antennas on Plexiglas poles and their cables.

- A Plexiglas antenna holder

- TOOLS: 5 min.-epoxy glue!

Well before the demonstration:

Make sure the Plexiglas antenna holders survived the trip. If not glue the parts that came

undone.

For battery operated transmitters:

- Put in the two AA batteries in first.

- Put in the four 6V batteries.

- With a voltmeter make sure that the batteries are properly in place by checking the

    voltages at the connecting pins.

INSTRUCTIONS FOR SETTING UP THE PROJECT

Suitcase

- Plug the white power cord into the suitcase and to the wall.

- Loosen the optical table (3 screws).

- Insert the 10dB directional coupler between the channel 2 output of the down

    conversion box (the big gold box) and the channel 2 input to the power amplifier

    (black box with a fan on top).

- Connect the BNC cable labeled PD to the output of the photodiode.

- Turn the power on.

Receiving antennas

Put the antenna holder in place and connect the detecting antennas' cables to the

corresponding cables coming out of the suitcase.

Transmitters

Place the transmitters roughly in the right place indicated by the strings attached to the

base of the detecting antennas' poles.

For wall supplied transmitters:

- Plug the brown power cord extension into a wall outlet.

- Set the two power supplies to 13V.

- Connect the supplies to the transmitters and plug them into the brown extension

  cord.

Just before the demonstration

- Switch on the power supply for transmitter #1 (the green LED should come on).

- Plug the directional coupler BNC cable into the little spectrum analyzer and select

  screen environment #2 (freq. range around 141MHz)

- Iteratively adjust the DRO and VCO adjustment screws so that the peaks that appear

  on the screen at first collapse together, centered on MARKER 1 (freq=142.5MHz)

- Switch on the power supply for transmitter #2.

- Adjust the new peaks to collapse together, centered on MARKER 2

  (freq=140.4MHz).

- Unplug the directional coupler BNC cable and plug the photodiode BNC cable into the S.A.

- Select the screen environment #1 (freq. range around 282MHz).

DEMONSTRATING THE PROJECT

Three peaks appear on the screen environment #1: the middle one is due to some intermodulation product of the signals. The extreme peak to the left is the signal from transmitter 2 and the extreme peak to the right is the signal from transmitter 1. The extreme peaks are roughly the same height because the transmitted powers are equal and there is very little competition between the signals at that point.

By putting a hand right in front of the horn antennas you attenuate one of the transmitted signal by a couple of dBs. You should see the corresponding peak go down and the other peak go up.